

FAKULTÄT FÜR MATHEMATIK UND NATURWISSENSCHAFTEN
TECHNISCHE UNIVERSITÄT DRESDEN

Institut für Theoretische Physik

Actomyosin mechanics at the cell level

DISSERTATION

zur Erlangung des akademischen Grades

Doctor rerum naturalium

(Dr. rer. nat.)

vorgelegt von

Anna Erzberger

geboren am 31. Mai 1986 in Berlin



Die Dissertation wurde in der Zeit vom **1. Oktober 2012** bis zum **30. September 2015**
am **Max-Planck-Institut für Physik Komplexer Systeme** angefertigt
und am **14. Januar 2016** verteidigt.

Primary advisor:

DR. GUILLAUME SALBREUX

First reviewer:

PROF. DR. FRANK JÜLICHER

Second reviewer:

PROF. DR. JOCHEN GUCK

Abstract

Almost all animal cells maintain a thin layer of actin filaments and associated proteins underneath the cell membrane. The actomyosin cortex is subject to internal stress patterns which result from the spatiotemporally regulated activity of non-muscle myosin II motors in the actin network. We study how these active stresses drive changes in cell shape and flows within the cortical layer, and how these cytoskeletal deformations and flows govern processes such as cell migration, cell division and organelle transport. Following a continuum mechanics approach, we develop theoretical descriptions for three different cellular processes, to obtain - in collaboration with experimental groups - a detailed and quantitative understanding of the underlying cytoskeletal mechanics.

We investigate the forces and cortex flows involved in adhesion-independent cell migration in confinement. Many types of cell migration rely on the extension of protrusions at the leading edge, where the cells attach to the substrate with specific focal adhesions, and pull themselves forward, exerting stresses in the kPa range. In confined environments however, cells exhibit migration modes which are independent of specific adhesions. Combining hydrodynamic theory, microfluidics and quantitative imaging of motile, non-adherent carcinosarcoma cells, we analyze the mechanical behavior of cells during adhesion-independent migration. We find that the accumulation of active myosin motors in the rear part of these cells results in a retrograde cortical flow as well as the contraction of the cell body in the rear and expansion in the front, and we describe how both processes contribute to the translocation of the cells, depending on the geometric and mechanical parameters of the system. Importantly, we find that the involved propulsive forces are several orders of magnitude lower than during adhesive motility while the achieved migration velocities are similar. Moreover, the distribution of forces on the substrate during non-adhesive migration is fundamentally different, giving rise to a positive force dipole. In contrast to adhesive migration modes, non-adhesive cells move by exerting pushing forces at the rear, acting to expand rather than contract their substrate as they move. These differences may strongly affect hydrodynamic and/or deformational interactions between collectively migrating cells.

In addition to the work outlined above, we study contractile ring formation in the actin cytoskeleton before and during cell division. While in disordered actin networks, myosin motor activity gives rise to isotropic stresses, the alignment of actin filaments in the cortex during cell division introduces a preferred direction for motor-filament interactions, resulting in anisotropies in the cortical stress. Actin filaments align in myosin-dependent shear flows, resulting in possible feedback between motor activity, cortical flows and actin organization. We investigate how

the mechanical interplay of these different cortical properties gives rise to the formation of a cleavage furrow during cell division, describing the level of actin filament alignment at different points on the cortex with a nematic order parameter, in analogy to liquid crystal physics. We show that cortical anisotropies arising from shear-flow induced alignment patterns are sufficient to drive the ingression of cellular furrows, even in the absence of localized biochemical myosin up-regulation. This mechanism explains the characteristic appearance of pseudocleavage furrows in polarizing cells.

Finally, we study the characteristic nuclear movements in pseudostratified epithelia during development. These tissues consist of highly proliferative, tightly packed and elongated cells, with nuclei actively travelling to the apical side of the epithelium before each cell division. We explore how cytoskeletal properties act together with the mechanics of the surrounding tissue to control the shape of single cells embedded in the epithelium, and investigate potential mechanisms underlying the observed nuclear movements. These findings form a theoretical basis for a more detailed characterization of processes in pseudostratified epithelia.

Taken together, we present a continuum mechanics description of the actomyosin cell cortex, and successfully apply it to several different cell biological processes. Combining our theory with experimental work from collaborating groups, we provide new insights into different aspects of cell mechanics.

Zusammenfassung

Der Zellkortex ist ein wichtiger Bestandteil des Zytoskeletts tierischer Zellen. Dieser besteht aus einer dünnen Aktin-Schicht mit assoziierten Proteinen, und befindet sich unmittelbar unterhalb der Zellmembran. In den Zellkortex sind Motorproteine eingebettet, die zellulär regulierte, kontraktile Spannungsfelder im Aktin-Netzwerk erzeugen. Wir untersuchen, wie diese aktiven Kräfte zelluläre Deformationen und Materialflüsse erzeugen, und welche Rolle diese Prozesse bei der Mechanik von Zellmigration, Zellteilung und Organellentransport spielen. Mithilfe von Ansätzen aus der Kontinuumsmechanik, entwickeln wir theoretische Beschreibungen für drei verschiedene zelluläre Prozesse, um in Zusammenarbeit mit experimentellen Gruppen ein detailliertes und quantitatives Verständnis der zugrunde liegenden mechanischen Prinzipien zu erhalten.

Wir beginnen mit der Untersuchung einer besonderen Form der zellulären Fortbewegung, die unabhängig von spezifischen adhäsiven Strukturen ist. Die meisten motilen Zellen bilden Plasmaausstülpungen an ihrem Leitsaum, welche mithilfe sogenannter Fokalkontakte am Untergrund haften, und so der Zelle erlauben, sich vorwärts zu ziehen. Dabei werden Drücke im kPa-Bereich auf das Substrat ausgeübt. Unter bestimmten Umständen sind Zellen jedoch in der Lage, sich ganz ohne solche Ankerstrukturen effektiv fortzubewegen. Wir kombinieren Theorie und Experimente, um die mechanischen Prinzipien solcher adhäsions-unabhängiger Migrationsmechanismen zu verstehen. Hierbei stützen wir uns auf experimentelle Untersuchungen von nicht-adhäsiven Karzinomzellen in mikrofluidischen Systemen. Durch die Anreicherung aktiver Motorproteine im hinteren Bereich erzeugen diese Zellen einerseits einen retrograden Aktinfluss in der kortikalen Schicht, andererseits gezielte kortikale Deformationen, die gleichzeitig zur Fortbewegung in den mikrofluidischen Kanälen beitragen. Wir stellen fest, dass die Antriebskräfte bei dieser Art der Migration um mehrere Größenordnungen geringer sind als bei der adhäsiven Fortbewegung, wobei jedoch ähnliche Geschwindigkeiten erzielt werden. Weiterhin liegt der nicht-adhäsiven Zellbewegung eine grundlegend andere Kräfteverteilung zugrunde: im Gegensatz zu adhäsiven Zellen, werden hierbei positive Kraftdipole erzeugt. Diese Unterschiede beeinflussen, wie migrierende Zellen in kollektiven Prozessen miteinander und mit ihrem Substrat interagieren.

Als nächstes betrachten wir die Bildung kontraktiler Ringe im Aktin-Zytoskelett während der Zellteilung. Hierbei kommt es zu einer geordneten Ausrichtung der Aktinfilamente im Zellkortex, wodurch anisotrope kortikale Spannungen auftreten, da die Interaktionen zwischen molekularen Motoren und Zytoskelettfilamenten eine bevorzugte Richtung erhalten. Wir untersuchen die Rückkopplungseffekte zwischen Motoraktivität, kortikalen Strömungen und der Aktinstruktur, und demonstrieren, wie diese Prozesse zur Bildung der Zellteilungsfurche führen.

Zuletzt widmen wir uns den charakteristischen Bewegungen der Zellkerne in mehrreihigen Epithelien während der Embryonalentwicklung. Diese Gewebe bestehen aus dicht gepackten, hochproliferativen, elongierten Zellen. Wir untersuchen, wie die Eigenschaften des Zytoskeletts gemeinsam mit dem mechanischen Einfluss der Gewebeumgebung die Form einzelner Zellen im Epithel bedingen. Weiterhin untersuchen wir mithilfe eines vereinfachten Modells mögliche Mechanismen, die den Bewegungen der Kerne in diesen Zellen zugrunde liegen könnten. Diese Ergebnisse bilden eine theoretische Grundlage für eine genauere Charakterisierung der Prozesse in mehrreihigen Epithelien.

Zusammengefasst präsentieren wir hier eine kontinuumsmechanische Theorie der kortikalen zellulären Aktinstrukturen, und wenden diese erfolgreich auf verschiedene zellbiologische Prozesse an. Die Kombination unserer theoretischen Beschreibungen mit experimentellen Arbeiten kollaborierender Gruppen ermöglicht neue Einblicke in verschiedene Aspekte der Zellmechanik.

Contents

1	Introduction	1
1.1	Forces in cells	1
1.1.1	Motor filament systems	2
1.1.2	The actin cytoskeleton	3
1.1.3	Non-muscle myosin II	4
1.1.4	The cell cortex	5
1.2	Hydrodynamics of active matter	5
1.2.1	The hydrodynamic limit	7
1.2.2	Linear response to generalized forcing	8
1.2.3	Constitutive relation for an active gel	8
1.3	Objectives of this work	11
2	Continuum theory of the actomyosin cortex	15
2.1	Differential geometry of an axisymmetric surface	15
2.1.1	Surface parameterization	16
2.1.2	The local basis	16
2.1.3	The metric tensor	17
2.1.4	Curvature tensor and Christoffel symbols	17
2.1.5	The covariant derivative	18
2.2	Force balance on the shell	19
2.3	Tensors on the axisymmetric shell	20
2.4	Equations of the axisymmetric active shell	21
2.4.1	Linear stability of a cylinder	23
2.5	Conclusion	25
3	Mechanics of non-adhesive cell migration	29

3.1	Adhesive and non-adhesive cell movements	30
3.1.1	Adhesive cell movements	30
3.1.2	Non-adhesive cell movements	30
3.1.3	Cell polarization during migration	32
3.2	Flows and forces during non-adhesive cell migration	34
3.2.1	Observations of non-adhesive cell migration in microfluidic channels	34
3.2.2	Theoretical description of adhesion-independent cell migration	35
3.2.3	Cell velocity and cortex flows depend critically on the substrate friction	45
3.2.4	Force density on the cell surface	53
3.3	Discussion	55
3.3.1	The fluid drag coefficient governs the threshold friction for adhesion-independent cell movement	55
3.3.2	Possibilities regarding the origin of substrate friction in non-adhesive cell migration	56
3.3.3	The role of forces and force dipoles for cell-cell interactions during collective cell migration	57
4	Furrow initiation in pseudocleavage and cytokinesis	61
4.1	Contractile rings and the initiation of cytokinesis	61
4.2	Furrow initiation in the <i>C. elegans</i> zygote	63
4.2.1	Theoretical description of furrow initiation	64
4.3	Discussion	69
4.3.1	The pseudocleavage furrow arises from the processes polarizing the cell	69
4.3.2	Robustness of the pseudocleavage and cytokinetic furrows	69
5	Nuclear movements in pseudostratified epithelia	75
5.1	Pseudostratified epithelia and interkinetic nuclear migration	75
5.2	Nuclear movements in cells of pseudostratified epithelia	76
5.2.1	Segment shapes	78
5.2.2	Nuclear dynamics	82
5.3	Discussion	85
5.3.1	Investigating force generation during nuclear movements in pseudostratified cells	85
6	Concluding remarks	89

CONTENTS

Appendices

Appendix A	Hydraulics of microfluidic channels with migrating cells	91
Appendix B	Internal friction during Walker cell migration	95
Appendix C	Image analysis and quantification	99
C.1	Estimation of cortical myosin intensities	99
C.2	Estimation of cortical flows	101
C.3	Software and tools	101

List of Figures

1.1	Filaments of the cytoskeleton	3
1.2	The actomyosin cortex and its constituents	6
2.1	Parameterization of the cell surface	19
2.2	Velocity on the surface	22
3.1	Adhesive cell migration	31
3.2	Non-adhesive cell migration	33
3.3	Blebbing Walker cells in microfluidic channels	34
3.4	Cortical laser ablations of migrating Walker cells	35
3.5	Theoretical description of Walker cells	37
3.6	Cortical flows in migrating Walker cells	42
3.7	External pressure and cell velocity	44
3.8	The threshold friction	45
3.9	Varying and measuring the friction coefficient	48
3.10	The role of channel friction for cell migration mechanics	50
3.11	Fluid flow induced by migrating Walker cells	52
3.12	Forces exerted by migrating Walker cells	54
4.1	Actomyosin contractile rings	62
4.2	Pseudocleavage and cytokinesis	63
4.3	Myosin distribution, flow velocities and cortical actin ordering during furrow initiation	65
4.4	Theoretical description of furrow initiation	70
5.1	Pseudostratified epithelia in development	77
5.2	Linear stability analysis of cortex shell segments	80

LIST OF FIGURES

5.3	Three-segment description of pseudostratified epithelial cells	82
5.4	Apical migration of nuclei	84
A.1	Single and multiple cells in microfluidic channels	92
B.1	Role of the nucleus and internal friction during Walker cell migration	97
C.1	Quantification of cortical myosin fluorescence intensity	100

List of Tables

3.1	Mechanical and geometric parameters of migrating Walker cells	49
3.2	Parameters derived from fitted estimates	51
3.3	Multipole moments of the force density in migrating Walker cells	53
4.1	Parameters in the theoretical description of furrow initiation	71
B.1	Fitted parameters of Walker cells for the description with internal friction	96

LIST OF TABLES

Chapter 1

Introduction

Living organisms are composed of self-replicating membrane bound compartments called cells, containing various molecules, including proteins and nucleic acids. Cell biology and related disciplines are concerned with the question how the molecules present in cells assemble and coordinate to carry out the diverse cellular functions underlying the behavior of living matter. The focus of this thesis is the *mechanical* machinery of cells, which controls cell shape, drives the transport of material, and enables cells to translocate and move actively through their environment. As part of this machinery, cells possess specialized structures which contain macromolecules able to transduce chemical energy from metabolic sources into movement, force and growth. We will first introduce the main constituents of the force-generating apparatus in cells, with a particular emphasis on our main structure of interest, the actomyosin cell cortex. In the second part of the introduction, we will present the theoretical approaches used here to describe these active and dynamic materials at the mesoscale - i. e. at time and length scales exceeding those characterizing the microscopic, molecular processes in the system.

1.1 Forces in cells

The term *cytoskeleton* was coined by French embryologist P. Wintrebert in 1931, at a time when the observation of subcellular structures by electron microscopy was not yet possible [43]. The existence of a cellular skeleton was postulated by theoretical considerations, following observations of the physical resilience of cells. A support structure was believed necessary to stabilize cell shape and internal compartmentalization against external deformations, which were seen to occur for example during the passage of egg cells through the confinements of their environment. Today, the term cytoskeleton refers to a number of different proteinous polymer networks contained within the cytoplasm of the cell. The molecular structure of their main constituents as well as several aspects of their interactions and functioning are well characterized. Beyond providing mechanical support, the components of the cytoskeleton transmit active, spatiotemporally regulated stresses, governing the shape of cells and driving cellular and subcellular motility. Contrary to the skeletal support structures of large organisms, the cytoskeleton is dynamic, capable of rapid rearrangements in response to external changes in the environment of the cell.

For example, a migrating cell following a chemical signal from a moving target, i. e. an immune cell hunting a bacterium, constantly has to change direction and rearrange polarized cytoskeletal structures of the migratory machinery as it follows its prey.

1.1.1 Motor filament systems

Cytoskeletal networks consist of helical polymer fibers assembled from globular or elongated subunits which interact non-covalently, allowing for rapid assembly and disassembly. The three types of cytoskeletal filaments in cells are microtubules, intermediate filaments and actin filaments (see Figure 1.1). Microtubules are the largest fiber structures with a diameter of 24 nm, and the most rigid, with a persistence length of several thousand μm [41]. They form the mitotic spindle, which separates the genetic material during cell division, provide the transport tracks for vesicle trafficking in the highly elongated axons of nerve cells and contribute the main structure in ciliary cell appendages, which fulfill mechanical as well as sensory functions in cells. Intermediate filaments are thinner and more flexible with an average diameter of 10 nm and a persistence length of only 0.5 μm . They provide mechanical stability for example in epithelial sheets, and by supporting the cell nucleus. Different intermediate filaments form a dense meshwork underneath the nuclear envelope known as the nucleoskeleton. Actin filaments organize into a thin layer on the inside of the cell membrane, a structure known as the cell cortex, which controls the shape of cells and conveys active deformations during cell movement or cell division. Although actin filaments feature the smallest diameter (8 nm), they are more rigid than intermediate filaments with a persistence length of 13.5 μm [41]. Most cellular protrusions are actin-based, such as the dynamic projections formed during cell migration, but also the stable stereocilia in the inner ear which tilt in response to sound, or the microvilli on some epithelial cells, for example in the gut, where they serve to increase the absorptive surface area. While actin filaments and microtubules have asymmetric subunits, which give rise to filament polarity, intermediate filaments are formed from symmetric monomers. Furthermore, the subunits of actin and microtubules catalyze the hydrolysis of nucleotide phosphates, adenosine triphosphate (ATP) or guanosine triphosphate (GTP), thereby converting the chemical energy present in the phosphoanhydride bond to drive the rapid remodeling of filaments. Active filament growth and shrinkage is regulated by the cell to generate spatiotemporally controlled forces underlying cell deformations and intracellular transport. A variety of proteins associate with cytoskeletal fibers. They regulate the sites and rates of assembly and disassembly, or link the filaments to each other or to other cellular structures, such as the cell membrane or the nucleus. A particular class of these accessory proteins is able to exert forces on the filaments, actively moving the filaments or translocating themselves along them. These so-called motor proteins convert chemical energy into work by undergoing cyclic conformational changes which are powered by the dephosphorylation of ATP or GTP molecules, allowing the motors to step along the filaments. Various types of motor proteins are found in cells, differing in the types of cytoskeletal filaments they associate with, the direction in which they walk along the filament, and the types of molecules, or cargo, they bind to with their remaining free domains. Many motor proteins transport membraneous vesicles in cells for example, while others associate with several filament bundles at the same

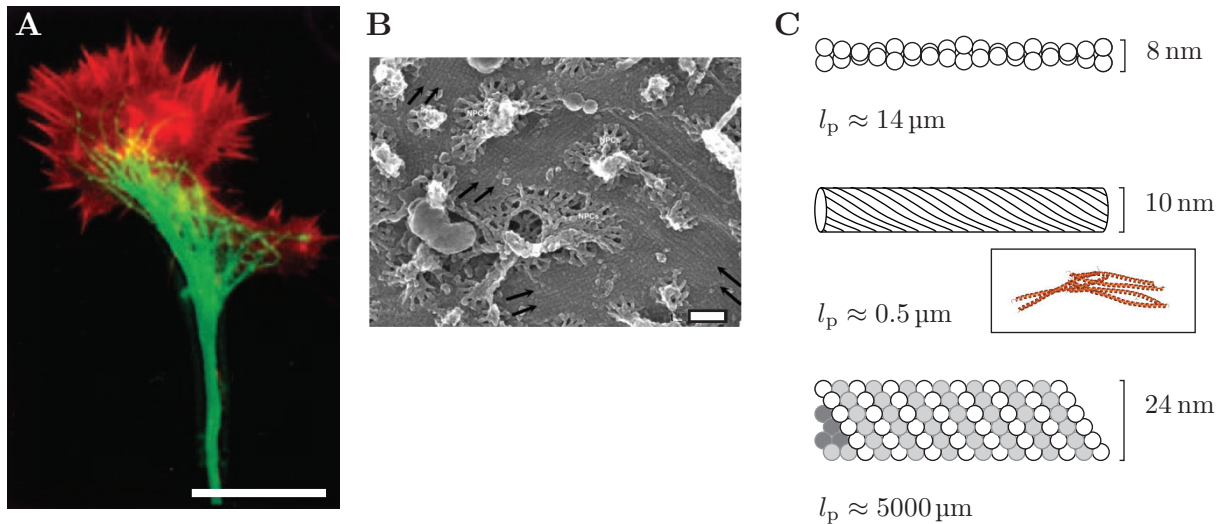


Figure 1.1: Filaments of the cytoskeleton.

A. Fluorescence microscopy image of a migrating neuron (growth cone), with microtubules stained green and actin filaments stained red. Scale bar: $20 \mu\text{m}$, Image taken from [41], Original published in [110]. **B.** Electron micrograph of the dense intermediate filamentous network on the inside of the nuclear envelope in a *Xenopus* oocyte. The nuclear lamina is the main component of the nuclear cytoskeleton, providing stiffness to the nucleus. Scale bar: 100 nm , Image taken from [47]. **C.** Schematics of the three cytoskeletal filaments, their persistence lengths l_p and diameters. Actin filaments (top) and microtubules (bottom) are assembled from globular asymmetric subunits, while intermediate filaments (middle) consist of elongated monomers. Inset: ribbon diagram of a human vimentin coil fragment, a mesenchymal intermediate filament, featuring several α -helices (from [123]).

time, generating stresses and network deformations.

1.1.2 The actin cytoskeleton

This work focuses on the actin cytoskeleton. Globular actin monomers polymerize into right-handed helical filaments with a 37 nm pitch [3] and highly variable length. While the persistence length of a single actin filament is on the order of ten μm s, bundling of several filaments is very common in cells giving rise to much more rigid structures [3]. The symmetry between the two ends of an actin filament is broken by the asymmetry of globular actin monomers. They are referred to as the pointed or plus end, and the barbed, or minus end. Conversely to this naming convention however, monomers can be added at both the minus and the plus end of the filament in principle, with the on- and off-rates depending primarily on the concentration of available free monomers in the solution, and the nucleotide state of the incorporated actin monomers. As mentioned in the previous section, actin monomers catalyze the hydrolysis of ATP, with the adenosine diphosphate and the free phosphate group remaining associated with the actin subunit. Thus, the actin subunits within a filament come in two different nucleotide states: the ATP bound T-form and the ADP bound D-form. Much of the free energy from the hydrolysis of ATP is stored in the filament, such that the dissociation of a D-form subunit in fact has a lower energetic cost than the dissociation of a T-form subunit, and the ratio of off-to-on rates

is much larger for the D-form than for the T-form. Most soluble actin monomers are found in the T-form in cells, since the physiological concentration of ATP is much larger than that of ADP. The more time an actin monomer has spent incorporated into a filament however, the more likely it is that the hydrolysis of its associated nucleotide phosphate has occurred. Thus, within a regime of free actin subunit concentration, at which nucleotide hydrolysis is slower than the rate of addition of a subunit to the filament in T-conformation, but faster than in the D-conformation, a direction of growth emerges: T-form monomers are added to the filament on one side, and D-form monomers are removed from the filament on the other side (see Figure 1.2 A). At a critical concentration of free subunits, the length of the filament remains constant. This energy consuming process is termed treadmilling. Actin turnover dynamics as well as actin filament organization are heavily regulated by different proteins in the cell. For example, the *in vitro* half life of an actin filament at physiological monomer concentrations is 30 min, but only 30 s in a non-muscle cell [3]. A large variety of proteins associates to actin, ranging from monomer- or filament-binding proteins, and actin nucleators that regulate filament turnover, to cross-linking and bundling proteins and proteins that link actin filaments to the plasma membrane and other structures. Actin architecture depends strongly on these actin associated proteins, which determine the different structures of the actin cytoskeleton, including the cell cortex, stress fibers and contractile rings. Furthermore, actin filaments can associate with several different myosin motors, of which myosin II is the most prominent one in the actomyosin cortex.

1.1.3 Non-muscle myosin II

Non-muscle myosin II consists of a 150 nm helical tail (see Figure 1.2 B), a globular head where the motor domains are located, and a neck region containing the two regulatory light chains (RLC). Phosphorylation of the RLC domains controls the conformational state of the myosin molecule, which assumes a compact assembly-incompetent form when unphosphorylated, and an unfolded conformation otherwise (Figure 1.2 B), in which case it can bind to actin and dimerize with other myosin II motors via tail-tail interactions [133]. The ATPase activity of the motor domains allows the head to move, driven by the enzymatically catalyzed hydrolysis of ATP. At the beginning of one stepping cycle, ATP binds to a myosin head, which is associated with actin. The resulting conformational change reduces the affinity of myosin to actin and induces the temporary dissociation of the head from the filament. Simultaneously, this ATP-dependent conformational change triggers the movement of an 8.5 nm lever arm located below the head, which is stabilized by the light chains. This movement displaces the myosin head by approximately 5 nm along the actin filament. ATP is hydrolyzed, and as the head weakly re-associates with actin at the new location, the free phosphate group from the hydrolysis is released, which triggers the strong binding of the head to the actin filament. This in turn results in a second conformational change, the so-called power stroke, where the myosin resumes its initial conformation 'reeling in' the main protein body and any associated structures. As ADP is released, the cycle returns to its initial state [3]. The time scales of the individual steps depend on the concentration of available ATP. These conformational changes allow the myosin motors to exert tension on the actin filaments, or to perform work moving either the filament,

or themselves along it (Figure 1.2 C). Such processes result in the contractility of stress fibers, cytokinetic rings or the circumferential rings in epithelia.

The regulatory light chains feature several different phosphorylation sites, which control the conformation of the myosin heads, modulating the ATPase activity of the motor domain in the presence of actin. In vitro experiments suggest that the phosphorylation of the RLC also regulates the assembly of Myosin II into minifilaments [133].

1.1.4 The cell cortex

Most animal cells accumulate a thin layer of actin filaments and associated myosin and other cross linking proteins on the inside of the cell membrane (Figure 1.2 D - E). This structure, termed the actomyosin cell cortex, governs the shape of cells and drives several types of cellular and subcellular motility. The thickness and composition of the cortex is subject to regulation and varies strongly among cell types and cell cycle phases. In HeLa cells, cortex thickness has been measured to range from 180 to 220 nm throughout the cell cycle [26]. The actomyosin cortex is highly dynamic, with actin and myosin turnover rates on the order of seconds to tens of seconds [112]. The local architecture of the cortex is largely determined by the presence of different cross-linking and actin-binding proteins. Some of these regulate the length and lifetime of actin filaments, while others mediate the coupling of the actin cortex to the plasma membrane, or interactions between filaments leading to the formation of bundles (see e. g. [95] for a review). Actin and myosin regulation determines how stresses are generated and responded to in the cortex. The spatiotemporally regulated stresses in the actomyosin cortex drive active shape changes of the cell during cell migration and cytokinesis. They also produce long-ranged flows within the cortical layer which, for example, establish cell polarity [86], or maintain actin-rich protrusions such as lamellipodia [95, 69]. In the following section, we discuss the theoretical framework we use to describe and understand actomyosin cortex mechanics.

1.2 Hydrodynamics of active matter

The actomyosin cortex can be understood as a many-body system, consisting of tens of thousands of interacting particles, i. e. actin filaments, molecular motors and cross-linking proteins. Several different length and time scales characterize the molecular interactions between the particles. For example, the mesh size of actin networks in the cortex ranges from tens to hundreds of nm [17, 39], with myosins moving along the filaments at velocities on the order of $0.1 - 5 \mu\text{m s}^{-1}$ [96, 58] and dwell times of a few seconds [96]. In this work, we study actomyosin based cellular processes at length scales of tens of microns, and time scales of minutes to hours. For example, many types of cell migration involve cortex flows at velocities of roughly $10 \mu\text{m min}^{-1}$. Similarly, during cell division, when a cell is cleaved into its two daughters, the cell cortex undergoes deformations of a few microns on time scales of about 1 to 10 min.

Hydrodynamic theories are concerned with the slow, long-ranged processes, which emerge from the microscopic dynamics of many-body systems. Hydrodynamic variables are conserved quantities or broken symmetry variables and are therefore subjected to continuity equations. In

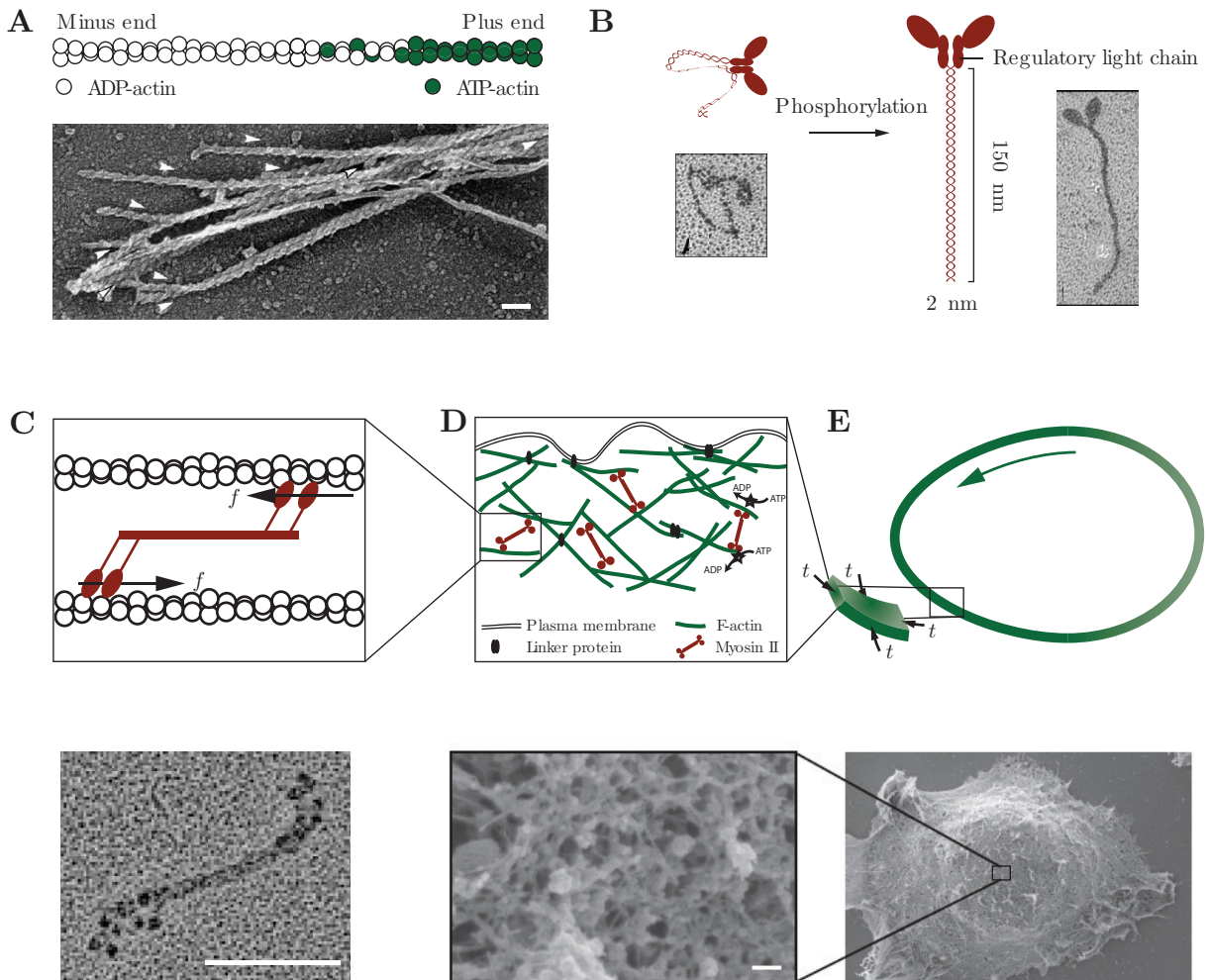


Figure 1.2: The actomyosin cortex and its constituents.

A. Actin filaments are assembled from asymmetric actin monomers, defining an axis of polarity. For treadmilling filaments, phosphorylated subunits (ATP-actin) are added to the plus end of the filament, while ADP-actin subunits dissociate from the minus end, such that the filament length is approximately maintained constant (adapted from [11]). Lower panel: Electron micrograph of myosin decorated actin filaments, from [122]. Arrowheads indicate direction of polarity. Scale bar: 100 nm. **B.** Myosin II motors change conformation upon phosphorylation of the regulatory light chain. In the open conformation, the heavy chain head domain can bind to and induce a stepping cycle along an actin filament when phosphorylated. Electron micrographs of smooth muscle myosin II taken from [64]. **C.** Myosin motors associate into bipolar minifilaments which bind actin at both ends, and move along or exert forces on the filament network. Lower panel: Field electron microscopic image of bipolar *Acanthamoeba* Myosin II minifilament with clustered heads from [81]. **D. - E.** In most cells, actin filaments, myosin motors and other cross-linking proteins form a thin layer underneath the plasma membrane, termed the actomyosin cortex. The ATP-dependent activity of myosin molecules results in contractile stresses in the actin network. Inhomogeneities in this active stress field generate flows within the cortical layer, as well as cell shape deformations. Lower panel: Scanning electron micrograph of the cortex of a mouse fibroblasts, from [11]. Scale bars: 100 nm.

the next sections, we present how these continuity equations are combined with constitutive equations, which state the mesoscopic properties of the material under study, to obtain the equations governing the hydrodynamic variables in the system. Specifically, the separation of scales between the fast microscopic and the slow macroscopic dynamics in a hydrodynamic system allows to assume that the system equilibrates within local volume elements at long times. Consequently, one may define a free energy density field in terms of the hydrodynamic variables. Then, generalized forces can be introduced conjugate to the hydrodynamic variables in the thermodynamic sense, and the constitutive equations are obtained as linear expansions of the generalized fluxes of hydrodynamic variables in the forces. Together with the conservation laws governing the hydrodynamic variables, these constitutive equations provide a closed form description of the spatiotemporal behavior of the material in the continuum limit. Here we will review the general hydrodynamic theory of active cytoskeletal matter, and present the derivation of a simple constitutive equation for actomyosin.

1.2.1 The hydrodynamic limit

In many body systems, conservation laws and continuously broken symmetries give rise to hydrodynamic variables, which change on length and time scales much larger than the microscopic scales governing the movements of individual particles [23]. Conservation laws can be stated as continuity equations of the form

$$\partial_t \phi + \nabla \cdot \mathbf{j} = 0 \quad (1.1)$$

with \mathbf{j} the flux density of a conserved quantity ϕ . Transformed to Fourier space, such equations state relationships between frequencies ω and wavenumbers k , which converge as

$$\lim_{k \rightarrow 0} \omega(k) = 0, \quad (1.2)$$

implying that long ranged variations in densities of conserved quantities are slow. On hydrodynamic timescales, microscopic processes thus locally relax to equilibrium. The notion of local equilibrium allows for the definition of a free energy density f , such that in a given volume V , the free energy is written as

$$F = \int dV f. \quad (1.3)$$

Thus, for systems with conserved quantities and/or continuously broken symmetries, one can construct a hydrodynamic theory with a free energy that is written in terms of slow, long-ranged variables. In the next section, we will introduce the generalized thermodynamic forces conjugate to these variables, and provide the linear approximation to the relationship between fluxes of hydrodynamic variables and generalized forces. These linearized equations are known as the constitutive relations of a material.

1.2.2 Linear response to generalized forcing

We can write the variation of the free energy in the hydrodynamic variables ϕ_i as the sum

$$\delta F = - \sum_i g_i \delta \phi_i, \quad (1.4)$$

where we have introduced the conjugate generalized forces

$$g_i = - \frac{\delta F}{\delta \phi_i}. \quad (1.5)$$

For a system, which is globally out of equilibrium, the generalized forces drive fluxes in the hydrodynamic variables $\partial_t \phi$, which act to return the system to the state of minimum free energy. To approximate the relationship between generalized fluxes and forces, we write the linear response of the system to small forcing away from equilibrium. In other words, we expand the generalized fluxes in the forces to linear order, introducing the coefficients L_{ij}

$$\partial_t \phi = \sum_i L_{ij} g_j. \quad (1.6)$$

The linear response captures the near-equilibrium dynamics of the system. Far away from equilibrium, nonlinear terms neglected in 1.6 may significantly influence the behavior of the system. The coefficients L_{ij} , coupling fluxes and forces, can be determined from microscopic theories describing the individual motion of particles, or have to be measured experimentally. Examples for such phenomenological coefficients are diffusion constants, which couple the flux of particles to gradients in concentration, or the electrical conductance relating the electric current to the applied voltage, or the viscosity of a fluid. The matrix of coefficients L_{ij} is called the Onsager matrix, after L. Onsager, who demonstrated that L_{ij} is a semi-positive matrix, which is either symmetric or antisymmetric, depending on the time-reversal properties of the couplings [99]. Equations of the form of 1.6 are known as the constitutive, or material equations, characterizing the behavior of the system of interest at the mesoscale. In the next section, we discuss the constitutive relation for the actomyosin cytoskeleton.

1.2.3 Constitutive relation for an active gel

Constitutive relations for active materials such as the actomyosin cytoskeleton have been derived previously, following the approach outlined in the previous section (see e. g. [70]), taking into account passive viscoelastic properties as well as the consequences of active polymerization and motor activity. In most parts of the actomyosin cytoskeleton, filaments form a crosslinked network, and the perpetual turnover of cross linking proteins in the cell introduces a viscoelastic timescale (see Sections 1.1.2 and 1.1.4). At timescales shorter than the characteristic turnover time, the actin network behaves as an elastic material, deforming under applied stresses. On longer timescales however, links between actin filaments are removed and formed in new places, giving rise to a viscous response to applied stress. Furthermore, the large aspect ratio of filamentous actin (see Section 1.1.1) may introduce anisotropies in the material due to actin filament

alignment. A nematic order parameter can then be introduced to describe the local ordering of filaments in the network. Moreover, since each filament has a well-defined plus- and minus-end (see Section 1.1.1 and Figure 1.1), a vectorial field characterizing the local polarity of filaments may be used instead. For example, local polarity effects drive the advancement of the lamellipodium in migrating cells [122] (also Chapter 3). The key difference between passive liquid crystals and cytoskeletal gels is given by the presence of associated motor proteins, which transduce chemical energy into work (see Section 1.1.3) and give rise to active internal stress fields driving the material out of equilibrium. Chirality effects, arising from the helical structure of actin filaments, have been discussed in [45]. For active cytoskeletal gels, hydrodynamic variables thus result from the conservation of momentum, angular momentum and mass of different components, as well as the continuously broken symmetry in the isotropic-to-nematic transition. Here, we briefly review the derivation of the constitutive relation for the stress tensor for an active gel. We consider the simple case of an active gel in the viscous limit and in the isotropic state. Similar calculations are presented in [70], [59] and [61]. Throughout the following, the Einstein summation convention will be used, and Greek indices α, β, γ will denote the Cartesian coordinates in three dimensions.

We begin by writing the relevant conservation laws in the continuum limit. The conservation of mass can be written as a continuity equation for the mass density ρ

$$\partial_t \rho + \partial_\alpha (\rho v_\alpha) = 0, \quad (1.7)$$

where we have introduced the velocity field v_α , describing the movement of material at each point as the center-of-mass velocity of local volume elements. In the absence of external forces acting on the system, the continuity equation for the momentum density $m_\alpha = \rho v_\alpha$ reads

$$\partial_t m_\alpha - \partial_\beta \sigma_{\alpha\beta}^{\text{tot}} = 0. \quad (1.8)$$

Here, we have introduced the total stress tensor $\sigma_{\alpha\beta}^{\text{tot}}$ as the negative momentum flux density tensor. Writing the free energy as a sum of kinetic and potential contributions, we have

$$F = \int dV \left[\frac{1}{2} m_\alpha v_\alpha + f_{\text{pot}} \right]. \quad (1.9)$$

The rate of change of free energy then reads

$$\frac{dF}{dt} = \int dV \left[\partial_t \left(\frac{1}{2} m_\alpha v_\alpha \right) + \partial_t f_{\text{pot}} \right] = \int dV \left[v_\alpha \partial_t m_\alpha - \frac{1}{2} v_\alpha v_\alpha \partial_t \rho + \partial_t f_{\text{pot}} \right]. \quad (1.10)$$

Rewriting the first terms using Equations 1.7-1.8 produces

$$\frac{dF}{dt} = \int dV \left[v_\alpha \partial_\beta \sigma_{\alpha\beta}^{\text{tot}} + \frac{1}{2} v_\alpha v_\alpha \partial_\beta (\rho v_\beta) + \partial_t f_{\text{pot}} \right], \quad (1.11)$$

and performing partial integrations, this can be recast into

$$\frac{dF}{dt} = \int dV \left[-(\sigma_{\alpha\beta}^{\text{tot}} + \frac{1}{2} \rho v_\beta v_\alpha) \partial_\beta v_\alpha + \partial_t f_{\text{pot}} \right]. \quad (1.12)$$

Note that the arising boundary terms vanish for isothermal systems with no fluxes or work at the boundaries. For an isotropic active fluid, $\partial_t f_{\text{pot}}$ can be written as

$$\partial_t f_{\text{pot}} = \sum_i \mu_i \partial_t n_i + r \Delta \mu_{\text{ATP}}, \quad (1.13)$$

where the n_i and μ_i are the particle number and chemical potentials of any different components constituting the active fluid, r is the reaction rate of ATP hydrolysis and $\Delta \mu_{\text{ATP}}$ is the difference in chemical potential between ATP and its reaction products. The Gibbs-Duhem relation $dP = \sum_i n_i d\mu_i$ connects changes in the pressure P to changes in the chemical potential gradients [59]. With these definitions, we obtain

$$\frac{dF}{dt} = \int dV \left[-(\sigma_{\alpha\beta}^{\text{tot}} + \frac{1}{2} \rho v_\beta v_\alpha + P \delta_{\alpha\beta}) \partial_\beta v_\alpha + r \Delta \mu_{\text{ATP}} \right]. \quad (1.14)$$

The final step is to introduce the dissipative stress tensor $\sigma_{\alpha\beta} = \sigma_{\alpha\beta}^{\text{tot}} + \rho v_\alpha v_\beta + P \delta_{\alpha\beta}$. It can be shown that $\sigma_{\alpha\beta}$ is symmetric for isotropic fluids [61], such that Equation 1.14 can be recast into

$$\frac{dF}{dt} = \int dV \left[-\sigma_{\alpha\beta} v_{\alpha\beta} + r \Delta \mu_{\text{ATP}} \right], \quad (1.15)$$

where $v_{\alpha\beta} = 1/2(\partial_\alpha v_\beta + \partial_\beta v_\alpha)$ is the symmetric part of the velocity gradient, also called the symmetric strain rate tensor. Thus, the generalized flux-force pairs are identified as $\sigma_{\alpha\beta} \leftrightarrow v_{\alpha\beta}$, and $r \leftrightarrow \Delta \mu_{\text{ATP}}$. Expanding the stress tensor to linear order in the generalized forces then produces

$$\sigma_{\alpha\beta} = \bar{\eta}_s \left(v_{\alpha\beta} - \frac{1}{3} v_{\gamma\gamma} \delta_{\alpha\beta} \right) + \bar{\eta}_b v_{\gamma\gamma} \delta_{\alpha\beta} + \bar{\zeta} \Delta \mu_{\text{ATP}} \delta_{\alpha\beta}, \quad (1.16)$$

where $\bar{\eta}_s$ (the shear viscosity), $\bar{\eta}_b$ (the bulk viscosity) and $\bar{\zeta}$ correspond to the phenomenological coupling coefficients L_{ij} in the linear response relation 1.6. According to our initial assumption, the ATP consuming activity of myosin motors results in an isotropic term in the stress.

Eq. 1.16 together with Eq. 1.8, which can be understood as a statement of force balance, provides an equation for the evolution over time of the velocity v_α at each point in the material. In the limit $\bar{\zeta} = 0$, corresponding to a simple passive fluid, we recover the well-known Navier-Stokes equations [75].

Actomyosin contractility

In the following, we set $\bar{\zeta} > 0$, which implies that myosin activity generates a *contractile* stress in the actomyosin network. We briefly discuss this choice. In muscle cells, myosin minifilaments are constrained by the sarcomere structure to generate contractile stresses. Contrarily, in the disordered actin networks of non-muscle cells, myosins can act as contractile or extensile force dipoles, depending on the microscopic configurations of actin filaments, myosin minifilaments and cross-linking proteins. In experiments, both cellular and *in vitro* reconstructed actomyosin networks have been observed to contract as a consequence of the activity of embedded myosins [9, 112, 71, 95]. Understanding how myosin activity results in macroscopic contractility in disordered actin networks has been the aim of several theoretical studies, and different suggestions

have been made. Some argue that nonlinear filament effects such as buckling may explain the contractility of actomyosin networks [83, 95], however, since the persistence length exceeds the average filament length in the cortex (see Section 1.1.1 and [41]), actin filaments may more appropriately be regarded as rigid in the cell cortex. A convincing possible explanation was presented in [30], and expanded on in [55], where it was shown that in a random cross-linked actin filament network, contractile configurations are energetically favorable compared to extensile ones. In the absence of filament cross-linking, these studies predict an increase in the frequency of extensile configurations over contractile ones. Some experiments on non-crosslinked motor filament systems [9, 65] have indeed found these to behave as extensile materials, supporting the importance of cross linking proteins to achieve contractility.

1.3 Objectives of this work

The goal of this work is to generate quantitative and experimentally validated descriptions of cytoskeletal processes in different cell biological contexts, using the hydrodynamic theory of active fluids. Our focus of interest is the actomyosin cell cortex. First, we detail the theoretical principles and considerations arising from the geometry of this structure, and derive the main equations used throughout this work in their general form. We then present results from highly collaborative efforts, where we applied this theoretical framework to address specific cell biological problems, in combination with experimental work. Each of these chapters begins with a brief introduction outlining the current state of research regarding the question investigated, followed by a presentation of results, and concludes with a discussion set within the context of the biological problem. In reporting our results, we focus on the theoretical aspects, but experimental data and images obtained in collaborating laboratories are also shown. Forming the most extensive part of this work, we studied a particular type of cell motility, which takes place in confined environments and does not require adhesive structures coupling the cell to its substrate, together with the lab of E. Paluch¹, specifically M. Bergert, as presented in chapter 3. Chapter 4 summarizes our collaboration with A.-C. Reymann and S. W. Grill², where we investigated the mechanics involved in furrow initiation at the onset of cell division. Chapter 5 contains mostly theoretical findings regarding the behavior of pseudostratified epithelia and the characteristic nuclear movements observed in these cells. This work arose from a collaboration with the group of C. Norden³. We conclude with a brief summary of our main findings and remaining open questions.

¹Medical Research Council, Laboratory for Molecular Cell Biology, University College London, UK.

²Biotechnology Center, Technical University Dresden, Germany

³Max Planck Institute of Molecular Cell Biology and Genetics, Dresden, Germany

List of symbols

i, j, \dots	Indices of different hydrodynamic variables
α, β, \dots	Indices of cartesian coordinates x, y, z
t	Time
k	Wavenumber
ω	Frequency
l_p	Persistence length of cytoskeletal filaments
ϕ_i	Hydrodynamic variable
j_α	Flux density
F	Free energy
f	Free energy density
V	Volume
g_i	Generalized force
L_{ij}	Onsager coupling coefficients
ρ	Mass density
v_α	Velocity
m_α	Momentum density
$\sigma_{\alpha\beta}^{\text{tot}}$	Total stress tensor
f_{pot}	Potential free energy density
μ	Chemical potential
n	Particle number
r	Reaction rate of ATP hydrolysis
$\Delta\mu_{\text{ATP}}$	Chemical potential difference between ATP and its reaction products
P	Pressure
$v_{\alpha\beta}$	Symmetric velocity gradient tensor
$\bar{\eta}_b$	Bulk viscosity
$\bar{\eta}_s$	Shear viscosity

$\bar{\zeta}$

Coupling coefficient between the chemical activity of myosin motors and the stress

Chapter 2

Continuum theory of the actomyosin cortex

The theory of active gels as outlined in the previous section has been successfully applied to describe the actin cytoskeleton in several cases (for example, in [62, 21]). We represent the actomyosin cell cortex as an active fluid in the thin-layer limit (see also [113, 86]). In this chapter, we present the main framework used throughout the remainder of this work to describe the mechanics of the cell cortex. Following a brief discussion of the geometrical assumptions underlying our theory and some remarks on notation, we introduce the relevant mathematical concepts, and proceed to derive the main equations governing the behavior of the cortical layer. We conclude with a discussion of some limiting cases.

2.1 Differential geometry of an axisymmetric surface

The thickness of the actomyosin cortex has been measured to be around 200 nm [26]. It is thus much smaller than the extensions of the cortex in the other directions, which are on the order of tens of μm (Figure 2.1 A). In the following, we will consider the thin-layer limit of the cortex and describe it as a two-dimensional object. It is thus assumed that the variation of the in-plane velocity across the layer thickness is sufficiently small to allow for a description in terms of average values, such that the cortical stress can be replaced by the tension tensor as given in Equation 2.24 in Section 2.3 (see also [113]).

Furthermore, we restrict the description to axisymmetric shapes. Our theory is thus applicable to processes where cells maintain an approximately rotationally symmetric cortex such as in the cases discussed in the following chapters.

To describe the curved shape of the cortical surface, we must first introduce several concepts from differential geometry. Choosing a parameterization of the surface, we derive the vectors tangent and normal to the surface at each point, the metric and curvature tensors, and introduce the covariant derivative. With these definitions, we can then express the balance of forces at each point on the cortex, to obtain - together with the constitutive relation for the cortical tension - the equations for the shape of the cortical surface and the velocity of flow on the surface. While

Greek letter indices are used to denote spatial coordinates in three dimensions as before, the letters i, j, k, \dots will index the coordinates defined on the surface, with upper and lower indices for contravariant and covariant vectors respectively.

2.1.1 Surface parameterization

We describe the cell cortex as a parametric surface embedded in three-dimensional Euclidean space, and introduce a pair of coordinates, the angle ϕ and the arc length s , to parameterize the surface (see Figure 2.1 B). In the Cartesian basis \mathbf{e}_x , \mathbf{e}_y and \mathbf{e}_z , a point on the surface is given by

$$\mathbf{X}(s, \phi) = x(s)\mathbf{e}_x + r(s) \sin \phi \mathbf{e}_y + r(s) \cos \phi \mathbf{e}_z. \quad (2.1)$$

The system is axisymmetric, i. e. invariant under changes of ϕ .

2.1.2 The local basis

The tangent space at each point on the surface is spanned by the tangent vectors

$$\mathbf{e}_s = \frac{\partial \mathbf{X}}{\partial s} = \begin{pmatrix} \partial_s x \\ \partial_s r \sin \phi \\ \partial_s r \cos \phi \end{pmatrix}, \quad \mathbf{e}_\phi = \frac{\partial \mathbf{X}}{\partial \phi} = \begin{pmatrix} 0 \\ r \cos \phi \\ -r \sin \phi \end{pmatrix}. \quad (2.2)$$

We restrict s to be an arc length parameter, such that $|\mathbf{e}_s| = \partial_s r^2 + \partial_s x^2 = 1$, and introduce ψ as the angle between \mathbf{e}_s and the plane normal to the x axis, for which the relations $\partial_s r = \cos \psi$ and $\partial_s x = \sin \psi$ must hold (see Figure 2.1 B).

Importantly, the tangent vectors on the curved surface do not form an orthonormal system. Thus, the dual vectors \mathbf{e}^s , \mathbf{e}^ϕ defined by $\mathbf{e}^i \cdot \mathbf{e}_j = \delta^i_j$, which span the cotangent space, do not coincide with the tangent vectors. The components of a vector expressed in the tangent space $\mathbf{v} = v^i \mathbf{e}_i$ or the cotangent space $\mathbf{v} = v_i \mathbf{e}^i$ are referred to as contravariant or covariant respectively. We denote contravariant components by upper indices, and covariant coordinates by lower indices. The metric tensor, introduced in Section 2.1.3, induces an isomorphism between the two bases.

The unit vector normal to the surface and pointing outward is given by

$$\mathbf{n} = \frac{\mathbf{e}_s \times \mathbf{e}_\phi}{|\mathbf{e}_s \times \mathbf{e}_\phi|} = \begin{pmatrix} -\cos \psi \\ \sin \phi \sin \psi \\ \cos \phi \sin \psi \end{pmatrix}. \quad (2.3)$$

The local basis defined by \mathbf{e}_s , \mathbf{e}_ϕ and \mathbf{n} is not invariant under a change of position on the surface. The curvature tensor defined in Section 2.1.4 describes the change of the local base along the surface.

2.1.3 The metric tensor

The physical properties of the surface, such as its area, or the length of a curve drawn along it, remain unchanged under a reparameterization of the surface or a spatial transformation. To compute these parameterization-invariant quantities, we introduce the metric tensor $g_{ij} = \mathbf{e}_i \cdot \mathbf{e}_j$

$$g_{ij} = \begin{pmatrix} 1 & 0 \\ 0 & r^2 \end{pmatrix}. \quad (2.4)$$

The metric tensor transforms contravariant to covariant vectors, an operation also referred to as the lowering of indices. Correspondingly, the inverse of the metric g^{ij} raises the indices. The metric tensor generalizes the notion of the inner product to curved spaces, providing a means to calculate the length of vectors, and angles between vectors, in the tangent space of the surface. Recalling that $\mathbf{e}^i \cdot \mathbf{e}_j = \delta^i_j$, the length of an arbitrary vector lying in tangent space $\mathbf{v} = v^s \mathbf{e}_s + v^\phi \mathbf{e}_\phi$ is given by $|\mathbf{v}| = v^i g_{ij} v^j$, and for the angle between two vectors \mathbf{v} and \mathbf{w} , we have $\cos \theta = v^i g_{ij} w^j / (|\mathbf{v}| |\mathbf{w}|)$. The area element of the surface is given by $d\mathcal{S} = \sqrt{\det g_{ij}} \, ds d\phi = r \, ds d\phi$.

2.1.4 Curvature tensor and Christoffel symbols

As one moves between points on the surface, the basis $(\mathbf{e}_s, \mathbf{e}_\phi, \mathbf{n})$ undergoes changes, which depend on the curvature of the surface. Writing the derivative of the local basis defines the curvature tensor C_{ij} , and the Christoffel symbols Γ_{ij}^k

$$\partial_i \mathbf{n} = C^j_i \mathbf{e}_j \quad (2.5)$$

$$\partial_i \mathbf{e}_j = -C_{ij} \mathbf{n} + \Gamma_{ij}^k \mathbf{e}_k. \quad (2.6)$$

Note that $\partial_i \mathbf{n}$ lies within the tangent plane, as follows from $\mathbf{n} \cdot \mathbf{n} = 1$ and $\mathbf{n} \cdot \partial_i \mathbf{n} = 0$. Multiplying Eq. 2.6 with \mathbf{n} gives the expression for the curvature tensor

$$C_{ij} = -\mathbf{n} \cdot \partial_i \mathbf{e}_j. \quad (2.7)$$

To express the Christoffel symbols, we multiply Eq. 2.6 with \mathbf{e}_l

$$\Gamma_{ij}^k \mathbf{e}_k \cdot \mathbf{e}_l = \partial_i \mathbf{e}_j \cdot \mathbf{e}_l \quad (2.8)$$

and use $\partial_i(\mathbf{e}_j \cdot \mathbf{e}_l) = \mathbf{e}_l \cdot \partial_i \mathbf{e}_j + \mathbf{e}_j \cdot \partial_i \mathbf{e}_l$ to obtain

$$\partial_i(\mathbf{e}_j \cdot \mathbf{e}_l) = \Gamma_{ij}^k \mathbf{e}_k \cdot \mathbf{e}_l + \Gamma_{il}^k \mathbf{e}_k \cdot \mathbf{e}_j. \quad (2.9)$$

Since the Christoffel symbols are symmetric with respect to an exchange of the lower indices [135], we can write $\partial_i g_{jl} + \partial_j g_{il} - \partial_l g_{ij} = 2\Gamma_{ij}^k g_{kl}$, where we have used the definition of the metric

tensor $g_{ij} = \mathbf{e}_i \cdot \mathbf{e}_j$. Thus, we obtain for the Christoffel symbols

$$\Gamma_{ij}^k = \frac{1}{2} g^{kl} (\partial_j g_{il} + \partial_i g_{jl} - \partial_l g_{ij}). \quad (2.10)$$

For the chosen parameterization, these quantities read

$$C_{ij} = \begin{pmatrix} \partial_s \psi & 0 \\ 0 & r \sin \psi \end{pmatrix}, \quad \Gamma_{ij}^s = \begin{pmatrix} 0 & 0 \\ 0 & -r \cos \psi \end{pmatrix}, \quad \Gamma_{ij}^\phi = \begin{pmatrix} 0 & \frac{\cos \psi}{r} \\ \frac{\cos \psi}{r} & 0 \end{pmatrix}. \quad (2.11)$$

The inverse eigenvalues of C^j_i correspond to the principal radii of curvature. As a consequence of the axisymmetry of the system, the curvature tensor is diagonal, and we have $R_1 = 1/\partial_s \psi$ and $R_2 = r/\sin \psi$. For a spherical shape for example, with $r = R \sin \psi$ and $\psi = s/R$, we find $R_1 = R_2 = R$, and for a cylinder with $r = R$ and $\psi = \pi/2$, we have $R_1 = \infty$ and $R_2 = R$. The mean curvature $H = 1/2(1/R_1 + 1/R_2)$ is $1/R$ for a sphere and $1/(2R)$ for a cylinder.

2.1.5 The covariant derivative

In the following sections we will consider the effects of different fields on the cortical surface, such as the velocity of material flows within the cortical layer, or active and passive tensions arising from the molecular interactions of motors, crosslinkers and actin filaments. In most cases, these fields are non-uniform along the cell surface. To describe how the corresponding vectors and tensors change as one moves along the surface, i. e. along a tangent vector, we introduce the covariant derivative. First, we consider the derivative of a vector expressed in contravariant components $\mathbf{v} = v^i \mathbf{e}_i$, given by

$$\begin{aligned} \partial_i \mathbf{v} &= (\partial_i v^j) \mathbf{e}_j + v^j (\partial_i \mathbf{e}_j) \\ &= (\partial_i v^j + \Gamma_{ik}^j v^k) \mathbf{e}_j - C_{ij} v^j \mathbf{n} \end{aligned} \quad (2.12)$$

where we have used Eq. 2.6 to separate the tangential and normal parts. The covariant derivative is the derivative in the tangential plane

$$\nabla_i v^j = \partial_i v^j + \Gamma_{ik}^j v^k. \quad (2.13)$$

For a vector in covariant components $\mathbf{w} = w_i \mathbf{e}^i$, we have

$$\nabla_i w_j = \partial_i w_j - \Gamma_{ij}^k w_k, \quad (2.14)$$

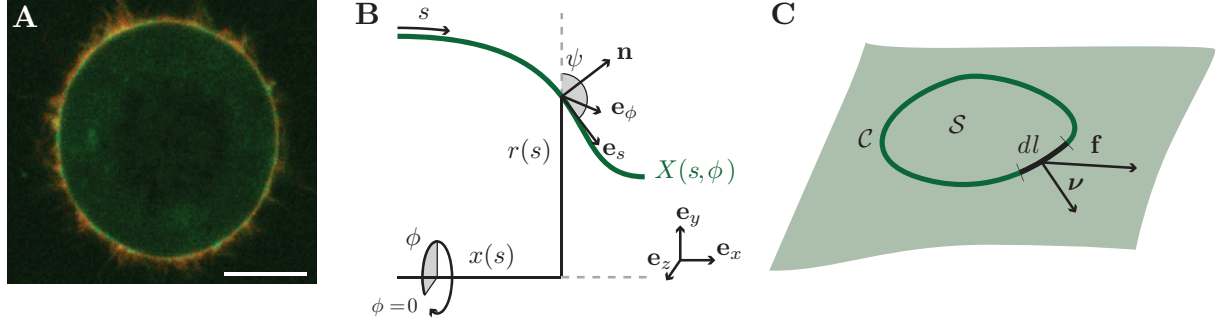


Figure 2.1: Parameterization of the cell surface.

A. Fluorescence microscopy image of the actomyosin cortex of a HeLa cell expressing actin-GFP (green) and the membrane marker mCherryCAAX (red), taken from [26]. The thickness of the actin cortex ~ 200 nm is much smaller than its extensions in other directions. Scale bar: $10 \mu\text{m}$. **B.** Parameterization of the cell surface. A point on the surface is given by $\mathbf{X}(\mathbf{s}, \phi)$, where we chose as coordinates the arc length s , and angle ϕ . The system is invariant to changes of ϕ . The constraint $|\mathbf{e}_s| = \partial_s r^2 + \partial_s x^2 = 1$ defines the angle ψ , for which $\partial_s r = \cos \psi$ and $\partial_s x = \sin \psi$ hold. The shape of the cell is given by $r(s)$. **C.** The sum of all forces acting on a closed region of the cortex must vanish. The contour and surface area of the region are denoted by \mathcal{C} and \mathcal{S} respectively. The force acting on a section of \mathcal{C} of length dl can be expressed as $\mathbf{f} = f^j \mathbf{e}_j = dl \nu_i t^{ij} \mathbf{e}_j$ with t^{ij} the tension tensor, and $\boldsymbol{\nu}$ the vector normal to dl .

as can be seen by considering the following. For the sum $v^j w_j$ we have $\nabla_i (v^j w_j) = \partial_i (v^j w_j)$, since $v^j w_j$ is a scalar quantity. Then, using Eq. 2.13 and the product rule, we have ([35])

$$\begin{aligned}
 v^j \nabla_i w_j + w_j \nabla_i v^j &= v^j \partial_i w_j + w_j \partial_i v^j \\
 v^j \nabla_i w_j + w_j (\partial_i v^j + \Gamma_{ik}^j v^k) &= v^j \partial_i w_j + w_j \partial_i v^j \\
 v^j \nabla_i w_j &= v^j \partial_i w_j - w_k \Gamma_{ij}^k v^j \\
 \nabla_i w_j &= \partial_i w_j - \Gamma_{ij}^k w_k.
 \end{aligned} \tag{2.15}$$

Similarly, for a tensor $\mathbf{t} = t^{ij} \mathbf{e}_i \otimes \mathbf{e}_j$, we have

$$\begin{aligned}
 \partial_i \mathbf{t} &= (\partial_i t^{jk}) \mathbf{e}_j \otimes \mathbf{e}_k + t^{jk} (\partial_i \mathbf{e}_j) \otimes \mathbf{e}_k + t^{jk} \mathbf{e}_j \otimes (\partial_i \mathbf{e}_k) \\
 &= (\partial_i t^{jk} + \Gamma_{il}^j t^{lk} + \Gamma_{il}^k t^{jl}) \mathbf{e}_j \otimes \mathbf{e}_k - C_{ij} t^{jk} \mathbf{n} \otimes \mathbf{e}_k - C_{ik} t^{jk} \mathbf{e}_j \otimes \mathbf{n},
 \end{aligned} \tag{2.16}$$

and the covariant derivative

$$\nabla_i t^{jk} = \partial_i t^{jk} + \Gamma_{il}^j t^{lk} + \Gamma_{il}^k t^{jl}. \tag{2.17}$$

With these definitions, we can now express the balance of forces on the curved cell surface.

2.2 Force balance on the shell

The forces exerted on one piece of the cortex arising from any internal or external sources present in the system must balance everywhere on the surface. We consider a section of length dl on the surface, with the unit vector $\boldsymbol{\nu}$ normal to the section, lying within the cortical shell (see

Figure 2.1 C). Expressed in the tangential base, the force acting on the section reads $\mathbf{f} = f^j \mathbf{e}_j$, with

$$f^j = dl \nu_i t^{ij}, \quad (2.18)$$

where t^{ij} is the tension tensor. Note that a significant gradient of tension *across* the thickness of the cortical layer gives rise to forces perpendicular to the surface, which are neglected here. The sum of all forces acting on a closed section with contour \mathcal{C} and surface area \mathcal{S} must vanish. External stresses act on the section from the inside and the outside of the cortical surface. We decompose the external stresses into shear stresses Σ and pressures P , and obtain

$$\int_{\mathcal{C}} dl \nu_i t^{ij} \mathbf{e}_j = \int_{\mathcal{S}} d\mathcal{S} \Sigma^j \mathbf{e}_j - P \mathbf{n}. \quad (2.19)$$

By the divergence theorem, we write this in the differential version

$$\begin{aligned} \int_{\mathcal{S}} d\mathcal{S} \nabla_i (t^{ij} \mathbf{e}_j) &= \int_{\mathcal{S}} d\mathcal{S} \Sigma^j \mathbf{e}_j - P \mathbf{n} \\ \nabla_i (t^{ij} \mathbf{e}_j) &= \Sigma^j \mathbf{e}_j - P \mathbf{n}. \end{aligned} \quad (2.20)$$

Then, using product rule and the Gauss-Weingarten equation $\nabla_i \mathbf{e}_j = -C_{ij} \mathbf{n}$ [53], we obtain the force balance equation in terms of its normal and tangential components

$$(\nabla_i t^{ij}) \mathbf{e}_j - t^{ij} C_{ij} \mathbf{n} = \Sigma^j \mathbf{e}_j - P \mathbf{n}. \quad (2.21)$$

Note that the Gauss-Weingarten equation can be recovered from Eq. 2.6 using Eq. 2.14, using that the basis vectors \mathbf{e}_i are covariant by definition.

2.3 Tensors on the axisymmetric shell

Here we provide the expressions of the physical quantities relevant for describing the behavior of the actomyosin shell in the parameterization introduced in the previous sections. The velocity on the surface can be decomposed into its tangential and normal parts

$$\mathbf{v} = v^s \mathbf{e}_s + v^\phi \mathbf{e}_\phi + v^n \mathbf{n}, \quad (2.22)$$

where v^s and v^ϕ describe the flow within the cortical layer in the s and ϕ directions, and v^n captures cortex deformations (see Figure 2.2). The assumption of axisymmetry implies that $v^\phi = 0$. In the chosen parameterization, the velocity gradient tensor $v_{ij} = 1/2 (\mathbf{e}_i \cdot \partial_j \mathbf{v} + \mathbf{e}_j \cdot \partial_i \mathbf{v})$ then reads

$$v_{ij} = \begin{pmatrix} \partial_s v^s + v^n \partial_s \psi & 0 \\ 0 & r(v^s \cos \psi + v^n \sin \psi) \end{pmatrix}. \quad (2.23)$$

Assuming that the cortical stress is constant along the height h of the layer, the tension tensor t_{ij} is related to the three-dimensional stress tensor $\sigma_{\alpha\beta}$ introduced in Section 1.2.3 (see Equation 1.16) by

$$t_{ij} = h \sigma_{ij} = h \sigma_{\alpha\beta} \mathbf{e}_i^\alpha \mathbf{e}_j^\beta, \quad (2.24)$$

(see also [14]). For the isotropic, viscous limit, we thus obtain the following constitutive relation for the cortical tension

$$t^i_j = \eta_s \left(v^i_j - \frac{1}{2} v^k_k \delta^i_j \right) + \eta_b v^k_k \delta^i_j + \zeta \delta^i_j \quad (2.25)$$

where the viscosities η_b and η_s are now two-dimensional viscosities, and we have absorbed the chemical potential difference between ATP and its reaction products $\Delta\mu_{\text{ATP}}$ (see Eq. 1.16) into the coefficient ζ for compactness. Thus, we can combine the force balance Equation 2.21 with the constitutive relation 2.25 to obtain the equations governing the flow within the cortical layer and the shape of the cell.

2.4 Equations of the axisymmetric active shell

The equations for the shape and flow of the cortical surface are obtained by inserting the constitutive relation for the cortical tension into the force balance equations. To proceed, it is useful to separate the tangential and normal directions in the force balance 2.21, obtaining the tangential and normal balance statements

$$\nabla_i t^{ij} = \Sigma^j, \quad (2.26)$$

$$t^{ij} C_{ij} = P. \quad (2.27)$$

Equation 2.25 describes the tension in a thin layer of an isotropic active fluid. Combining 2.25 with 2.26 - 2.27, we obtain a system of equations for the shape and flow of the cortical layer. In the direction of \mathbf{e}_s , we find

$$\begin{aligned} \Sigma^s = & \partial_s \zeta + \left(\eta_b + \frac{1}{2} \eta_s \right) \left(\partial_s^2 v^s + \partial_s v^n \partial_s \psi + v^n \partial_s^2 \psi + \frac{\cos \psi}{r} \left(\partial_s v^s + v^n \partial_s \psi - \frac{v^s \cos \psi + v^n \sin \psi}{r} \right) \right) \\ & + \left(\eta_b - \frac{1}{2} \eta_s \right) \frac{\sin \psi (\partial_s v^n - v^s \partial_s \psi)}{r}, \end{aligned} \quad (2.28)$$

and in the direction normal to the surface, the resulting equation reads

$$\begin{aligned} P = & \zeta \left(\partial_s \psi + \frac{\sin \psi}{r} \right) + \left(\eta_b + \frac{1}{2} \eta_s \right) \left(\partial_s \psi (\partial_s v^s + v^n \partial_s \psi) + \frac{\sin \psi (v^s \cos \psi + v^n \sin \psi)}{r^2} \right) \\ & + \left(\eta_b - \frac{1}{2} \eta_s \right) \frac{\sin \psi (\partial_s v^s + 2v^n \partial_s \psi) + \cos \psi \partial_s \psi v^s}{r}. \end{aligned} \quad (2.29)$$

The normal velocity v^n is related to temporal changes of the shape r (see Figure 2.2) by

$$v^n = \frac{1}{\sin \psi} \partial_t r, \quad (2.30)$$

which allows us to rewrite Equations 2.28 - 2.29 as a coupled, nonlinear system composed of an ordinary differential equation for v^s and a partial differential equation for r . We now analyze some limits of this system.

At steady state, where $\partial_t r = 0$, Equations 2.28-2.29 simplify to

$$\Sigma^s = \partial_s \zeta + \left(\eta_b + \frac{1}{2} \eta_s \right) \left(\partial_s^2 v^s + \frac{\cos \psi}{r} \left(\partial_s v^s - \frac{v^s \cos \psi}{r} \right) \right) - \left(\eta_b - \frac{1}{2} \eta_s \right) \frac{\sin \psi v^s \partial_s \psi}{r}, \quad (2.31)$$

$$P = \zeta \left(\partial_s \psi + \frac{\sin \psi}{r} \right) + \left(\eta_b + \frac{1}{2} \eta_s \right) \left(\partial_s \psi \partial_s v^s + \frac{\sin \psi v^s \cos \psi}{r^2} \right) + \left(\eta_b - \frac{1}{2} \eta_s \right) \frac{\sin \psi \partial_s v^s + \cos \psi \partial_s \psi v^s}{r}. \quad (2.32)$$

Intrinsic cortical flows in the shell are driven by gradients in the active stress. In the limit of constant active tension $\partial_s \zeta = 0$, Equation 2.31 is solved by $v^s = 0$ in the absence of any external shear stresses acting on the surface, that is for $\Sigma^s = 0$. We then obtain the following equation for the shape

$$P = \zeta \left(\partial_s \psi + \frac{\sin \psi}{r} \right). \quad (2.33)$$

Rewriting Equation 2.33 in terms of the mean curvature H (see Section 2.1.4), we obtain $P/(2\zeta) = H$. Thus, Equation 2.33 is solved by a class of constant-mean-curvature surfaces [22, 5]. Substituting $u = \sin \psi$, and using that $\partial_s r = \cos \psi$, we find

$$\frac{P}{\zeta} = \frac{\partial_s u}{\partial_s r} + \frac{u}{r} = \partial_r u + \frac{u}{r}, \quad (2.34)$$

which is solved by

$$u = C \frac{1}{r} + \frac{P}{2\zeta} r, \quad (2.35)$$

with C a constant of integration. If we impose that the shell is to surround some chosen volume V , the pressure P is set by the volume constraint

$$V = \pi \int_{s_1}^{s_2} ds \quad r^2 \sin \psi, \quad (2.36)$$

where s_1 and s_2 are the boundary points. In the case where the shape has a pole, i. e. the boundary condition for Equation 2.35 reads $u(r = 0) = 0$, the solution is given by a portion of a sphere

$$r = \frac{2\zeta}{P} \sin \psi, \quad \psi = \frac{s}{R_s} \quad (2.37)$$

with radius $R_s = 2\zeta/P$, and we recover that the pressure drop across the surface of a sphere is $P = 2\zeta/R_s$ [31]. If we instead impose the tangent $\partial_s r$ to be zero at some chosen $r = R$, i. e. $u(r = R) = 1$, we obtain

$$u = \frac{R}{r} + \frac{P}{2\zeta} \left(r - \frac{R^2}{r} \right). \quad (2.38)$$

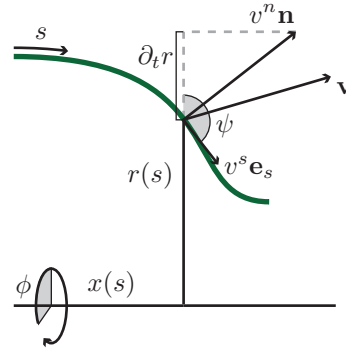


Figure 2.2: Velocity on the surface.

Resubstituting u , and using Equation 2.33 for the pressure, we obtain a second order differential equation for the shape r ,

$$\sin \psi = \frac{R}{r} + \frac{1}{2} \left(\partial_s \psi + \frac{\sin \psi}{r} \right) \left(r - \frac{R^2}{r} \right). \quad (2.39)$$

For $V = \pi R^2 L$ and with a second boundary condition $r(s_2) = R$, the solution is given by a cylinder $r = R$, $\psi = \pi/2$, $P = \zeta/R$. In Section 5.2.1, we discuss the resulting shapes for different volumes.

2.4.1 Linear stability of a cylinder

Whether the steady state solutions to Equations 2.31-2.32 persist under perturbations, depends on the choice of the mechanical and geometric parameters characterizing the cortex. We present here the stability analysis to linear order for the cylindrical solution with conserved volume, retrieved in the previous section for the case of constant active tension ζ . Following a similar approach, or using arguments based on the minimization of the surface energy, it can be shown that the sphere is always a stable solution of Equation 2.33 (e. g. [5]) given appropriate boundary conditions. We expand Equations 2.28-2.29 to linear order around the cylindrical steady state solution, i. e. we perform the substitutions $r = R + \delta r$, $\psi = \pi/2 - \partial_s \delta r$, $v^s = \delta v^s$, $P = \zeta/R + \delta P$, and neglect terms of quadratic or higher order in the perturbations. This produces a linear system of equations for the temporal evolution of perturbations away from the steady state

$$0 = \frac{\zeta(2\eta_b - \eta_s)}{R(2\eta_b + \eta_s)} \partial_s \delta r + \frac{R\zeta(2\eta_b - \eta_s)}{2\eta_b + \eta_s} \partial_s^3 \delta r + \frac{4\eta_b \eta_s}{2\eta_b + \eta_s} \partial_s^2 \delta v^s \quad (2.40)$$

$$\partial_t \delta r = \frac{2\zeta}{2\eta_b + \eta_s} \delta r + \frac{2R^2 \zeta}{2\eta_b + \eta_s} \partial_s^2 \delta r - \frac{R(2\eta_b - \eta_s)}{2\eta_b + \eta_s} \partial_s \delta v^s + \frac{2R^2}{2\eta_b + \eta_s} \delta P. \quad (2.41)$$

We solve the first equation for $\partial_s^2 \delta v^s$

$$\partial_s^2 \delta v^s = -\frac{\zeta(2\eta_b - \eta_s)}{4R\eta_b \eta_s} \partial_s \delta r - \frac{R\zeta(2\eta_b - \eta_s)}{4\eta_b \eta_s} \partial_s^3 \delta r, \quad (2.42)$$

and integrate both sides of the equation from 0 to s , obtaining

$$\partial_s \delta v^s = -\frac{\zeta(2\eta_b - \eta_s)}{4R\eta_b \eta_s} \delta r - \frac{R\zeta(2\eta_b - \eta_s)}{4\eta_b \eta_s} \partial_s^2 \delta r + C_1. \quad (2.43)$$

Combining Equation 2.43 with 2.41, and substituting $\tilde{\eta} = 4\eta_b \eta_s / (2\eta_b + \eta_s)$ we find

$$\tilde{\eta} \partial_t \delta r = \zeta \delta r + R^2 \zeta \partial_s^2 \delta r + C_2, \quad (2.44)$$

where we have absorbed all constant terms into $C_2 = 4\eta_b \eta_s R(2R\delta P + C_1(\eta_s - 2\eta_b)) / (2\eta_b + \eta_s)^2$. To analyze whether the perturbations δr grow or decay over time, we make the following ansatz

$$\delta r(s, t) = \tilde{\delta r}(s) \exp(\omega t), \quad (2.45)$$

and investigate the conditions for the existence of unstable solutions, for which the growth rate is greater than zero, i. e. $\omega > 0$. With 2.45, Equation 2.44 simplifies to

$$\tilde{\eta}\omega\delta r = \zeta\delta r + R^2\zeta\partial_s^2\delta r + C_2, \quad (2.46)$$

which is solved by

$$\delta r = A\cos(\lambda s) + B\sin(\lambda s) - \frac{C_2}{\zeta\lambda^2 R^2}, \quad (2.47)$$

where A and B are integration constants, and the wavelength is given by

$$\lambda = \frac{1}{R}\sqrt{1 - \omega\frac{\tilde{\eta}}{\zeta}}. \quad (2.48)$$

Imposing that the volume is conserved, i. e. $\int_0^L \delta r = 0$ and $\int_0^L \partial_t \delta r = 0$, we obtain

$$\begin{aligned} C_2 &= -R^2\zeta\frac{\partial_s\delta r(L) - \partial_s\delta r(0)}{L}, \\ &= -\frac{R^2\zeta\lambda}{L}(B(\cos(\lambda L) - 1) - A\sin(\lambda L)). \end{aligned} \quad (2.49)$$

Furthermore, we seek solutions fulfilling the boundary conditions

$$\delta r(0) = 0, \quad \delta r(L) = 0. \quad (2.50)$$

From Equations 2.49 - 2.50, we recover that perturbation wavelengths allowed by these conditions solve the transcendental equation

$$0 = \lambda L \sin(\lambda L) + 2(\cos(\lambda L) - 1), \quad (2.51)$$

which has the roots $\lambda = 2\pi n/L$ with $n \in \mathbb{Z}$ and a second set of solutions, for which it can be shown that $\lambda > 2\pi/L$. Using Equation 2.48 to relate ω and λ , the instability condition $\omega > 0$ is restated in terms of λ as

$$1 - R^2\lambda^2 > 0. \quad (2.52)$$

Since the smallest nonzero perturbation wavelength consistent with the boundary conditions is given by $2\pi/L$, the solution of the cylindrical steady state solution is unstable, if

$$L > 2\pi R, \quad (2.53)$$

and is therefore determined exclusively by the aspect ratio of the cylinder. The instability arises from the contractile tension acting to minimize the surface area of the shape. At constant volume, the surface area of a cylinder is reduced by radial modulations with wavelengths greater than the perimeter. Thus a cylindrical cortex is susceptible to unstable modes, if its length exceeds the perimeter. Just like a liquid jet subjected to surface tension, a contractile viscous cylindrical sheet then undergoes the Plateau-Rayleigh instability and breaks up into droplets [31, 38]. In Chapter 5, we discuss the effect of external elastic stresses on the stability of cortical shapes, such as may act on cells embedded in an elastic medium or surrounded by neighboring

cells within a tissue.

2.5 Conclusion

In this chapter, we have introduced the differential geometric definitions required to formulate the continuum mechanics theory used throughout the remainder of this work, we have derived the main equations governing the behavior of an axisymmetric, active fluid cortex, and we analyzed some limiting cases. In the following parts, we apply this framework to several cell biological settings, which meet our assumptions. Combining this theoretical approach with experimental measurements, we aim to gain insight into the processes involved in phenomena like cell migration and cell division. A fundamental limitation of the theory presented here resides in the assumption of axisymmetry for the cortical layer. Different approaches will be necessary to describe cellular systems in which axisymmetry is broken.

List of symbols

i, j, \dots	Indices of the coordinates on the surface
α, β, \dots	Indices of cartesian coordinates x, y, z
t	Time
s	Arclength surface coordinate
ϕ	Angle surface coordinate
∇_i	Covariant derivative operator
\mathbf{X}	Axisymmetric surface representing the cell cortex
$\mathbf{e}_x, \mathbf{e}_y, \mathbf{e}_z$	Cartesian basis vectors
r	Shape of the axisymmetric surface
$\mathbf{e}_s, \mathbf{e}_\phi$	Tangent basis vectors of the surface
\mathbf{n}	Normal vector of the surface
ψ	Surface angle
g_{ij}	Metric tensor
C_{ij}	Curvature tensor
Γ_{ij}^k	Christoffel symbols of the second kind
H	Mean curvature
\mathcal{S}	Surface area of a closed section on the surface
\mathcal{C}	Contour of a closed section on the surface
dl	Length of a section on the surface
ν_i	Vector normal to the section dl
f_i	Force acting on the section dl
t_{ij}	Tension tensor
Σ	Sum of shear stresses acting on the surface
P	Sum of pressures acting on the surface
v^s	Velocity of flow within the surface

v^n	Velocity normal to the surface
v_{ij}	Symmetric velocity gradient tensor
$\sigma_{\alpha\beta}$	Stress tensor
h	Height of the cortical layer
η_b	Two-dimensional bulk viscosity
η_s	Two-dimensional shear viscosity
ζ	Active tension
u	Substitution variable, $u = \sin \psi$
C	Integration constant
V	Volume
s_1, s_2	Boundary points
R_s	Radius of a sphere
R	Radius of a cylinder
L	Length of a cylinder
$\delta r, \delta v^s, \delta P$	Dynamic perturbations
C_1, C_2	Constants
$\tilde{\eta}$	Viscosity parameter, $\tilde{\eta} = 4\eta_b\eta_s/(2\eta_b + \eta_s)$
ω	Perturbation growth rate
λ	Perturbation wavelength
A, B	Integration constants

Chapter 3

Mechanics of non-adhesive cell migration

Many cells have the ability to move actively through their environment in a directional fashion, a behavior first observed by van Leewenhoeck in 1677 in a sample of rain water [132]. His letters to the Royal Society in London are surprisingly accurate. The following description for example is highly consistent with recent electron or fluorescence microscopy images such as shown in Figure 3.1:

'When these animalcula or living atoms did move, they put forth two little horns, continually moving themselves: The place between these two horns was flat, though the rest of the body was roundish, sharpning a little towards the end, where they had a tayl, near four times the length of the whole body, of the thickness (by my microscope) of a spiders-web; at the end of which appear'd a globul, of the bigness of one of those which made up the body.'

During cell migration, cytoskeletal processes, involving controlled cell deformations and cortex flows are coordinated to give rise to self-propelled motion. Movement at low Reynolds number requires the sustained input of energy achieved by the activity of the cytoskeleton. Over the course of the years, several different types - or modes - of cell migration have been identified and characterized, some of these are driven mostly by the directed ATP-dependent polymerization of actin filaments, while in other cases cell propulsion is predominantly achieved by the motor activity of myosin proteins [24, 74]. Cells are required to be motile in a variety of contexts, ranging from the movements of single celled organisms such as the slime mold *Dictyostelium* to the migration of embryonic cells during development, or the patrolling of immune cells through the lymphatic vessels and other tissues of the body [29]. Cell migration is also relevant in various pathological contexts such as cancer or inflammation. The mechanisms driving cell migration during these different processes are diverse [24].

3.1 Adhesive and non-adhesive cell movements

3.1.1 Adhesive cell movements

For a long time, the cell biology of migration has been studied by observing motile cells plated on flat microscopy cover slips. These studies established the canonical model of cell motility as a three-step cycle, which was first summarized by Abercrombie in 1978 [1]: Cells extend actin-rich protrusions at their leading edge, for example lamellipodia and/or narrower filopodia (see Figure 3.1), then subsequently form specific adhesive structures with the underlying substrate and exert large traction stresses on these, pulling themselves forward. In the last step, the cell rear is retracted. These substrate adhesions contain assemblies of integrins, specific transmembrane receptor proteins mediating the contact between the cell cortex and extracellular structures [63]. Numerous studies have investigated the role of focal adhesions in cell locomotion [25, 100, 46], and combining *in vitro* and *in vivo* experiments with mathematical modeling, a thorough understanding of the mechanics and the molecular interactions involved in adhesive, lamellipodial migration has been achieved [127, 90, 69, 89]. Lamellipodial migration is driven primarily by the polymerization of actin filaments at the leading edge of the cell [3]. Although the activity of myosin motors generates contractile stresses in the cell rear which result in the retraction of the trailing edge [66], myosin-independent movement is possible in the lamellipodial mode [60]. For adhesive cells on flat substrates, techniques such as traction force microscopy have proven to be very useful to measure the magnitude and distribution of forces exerted during migration. Fluorescent microbeads are inserted in the elastic migration substrate, allowing for the measurement of the induced deformation field from the displacement of the beads by the moving cell and the calculation of the traction stresses for known elastic constants of the substrate. Such measurements have established that single focal adhesions sustain forces of tens of nN [116] giving rise to traction stresses in the range of several kPa during adhesive migration [34]. Similarly, adhesive fibroblasts within hydrogels were found to exert traction stresses ranging from 0.1 to 5 kPa [79]. The distribution of stresses during adhesive migration is characterized by a negative, i. e. contractile, force dipole [118, 124]: pulling forces are exerted on the focal adhesion sites at the frontal protrusions of the cell (see Figure 3.1). Large traction stresses induce deformation fields in the elastic substrate of migrating cells, which may reorganize networks of extracellular materials [117, 118]. These deformations and stresses in turn may affect cell alignment and polarization [3], suggesting that traction stresses during cell migration may be crucial for cell-cell interactions and tissue organization in vertebrates.

3.1.2 Non-adhesive cell movements

As the technical capabilities to study cells and cell motility in different environments, i. e. within live tissue, are improving, observations accumulate which suggest that motile cells are often able to switch between a variety of different modes of migration. These involve different strategies to generate propulsion, and seem to adapt to the particular parameters of a cell's environment [24, 74, 51]. In particular, not all cellular movements appear to require receptor-

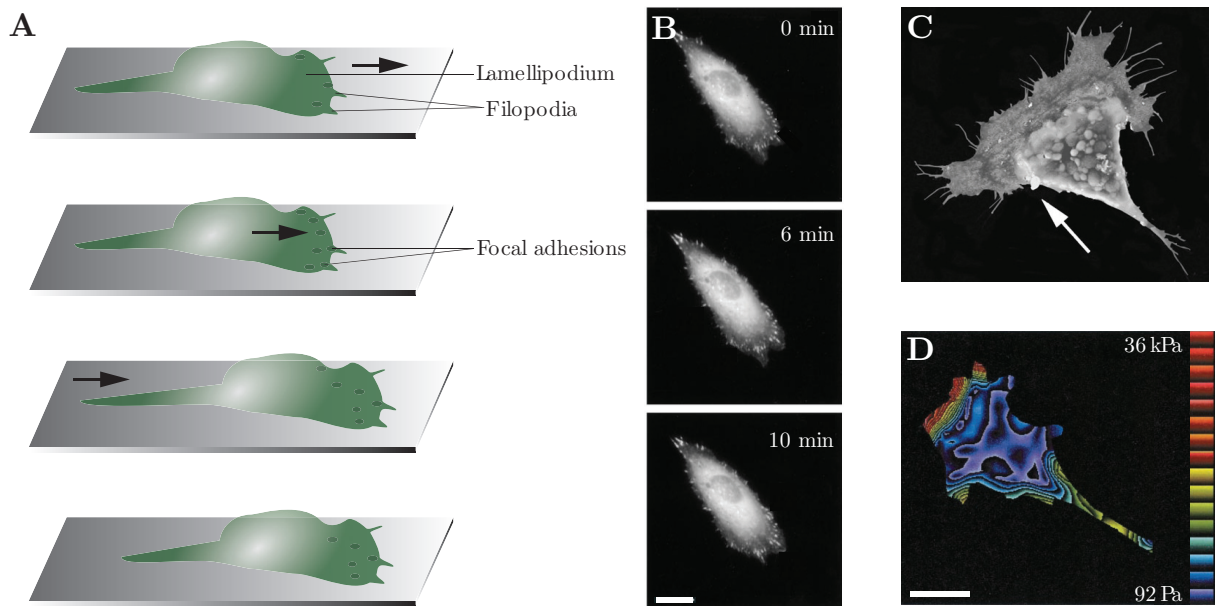


Figure 3.1: Adhesive cell migration.

A. Schematic representation of the classical three-step cycle of adhesive cell migration. Cells extend actin-based protrusions at their leading edge, form specific adhesion structures with the underlying substrate and pull the cell body forward, while the cell rear detaches. **B.** Time-lapse fluorescence microscopy images of a migrating fibroblast with fluorescent focal adhesions (GFP-zyxin). Adhesion points localize to the underside of protrusions at the leading edge. Scale bar: $20\ \mu\text{m}$. Image adapted from [10]. **C.** Electron micrograph of a migrating *Xenopus* neural crest cell with a well developed lamellipodium and filopodia at the leading edge and a retracting rear. Image from [72]. **D.** Traction force microscopy image of a migrating fibroblast, obtained by tracking fluorescent microbeads embedded in the substrate. The traction stresses involved in adhesive migration are in the kPa range, the stress distribution is characterized by a contractile, negative force dipole. Scale bar: $20\ \mu\text{m}$. Image adapted from [94].

mediated interactions between cells and their environment (see Figure 3.2). Laemmermann and colleagues conducted a cell race among leukocytes in the footpad of a mouse [73]. They compared cells lacking the ability to form substrate adhesions to unmodified wildtypes. Surprisingly, the two cell populations were found to require the same amount of time to reach the closest lymph node, demonstrating not only that these cells are able to migrate without specific substrate adhesions, but that they are not even slowed by their loss. Cells tend to switch to non-adhesive migration modes when they are confined by their environment. Liu et al. (2015) induced non-adhesive movements in a range of different cell types, including leukocytes, fibroblast and muscle cell precursors by compressing the cells between two plates [82]. Furthermore, Ruprecht et al. showed recently that zebrafish progenitor cells can move in a non-adhesive migration mode within the sphere-stage embryo *in vivo* [111]. Carcinosarcoma cells also migrate in the absence of specific substrate adhesions in a variety of confined environments (see Figure 3.2). Common characteristics observed in different cell types include the formation of spherical protrusions known as blebs, actomyosin accumulation in the rear, and dependence on myosin II activity [15, 73, 102, 111]. A detailed understanding of such integrin independent movement types is lacking however. It has remained unclear how cells transmit forces to their environment in the absence of specific substrate adhesions, and the magnitude and distribution of such forces is unknown. Our aim is to obtain a quantitative understanding of the mechanics and the physical principles underlying non-adhesive cell movements.

3.1.3 Cell polarization during migration

Cells need to be polarized to migrate, i. e. the symmetry between the front and the rear of a cell must be broken, giving rise to a leading and a trailing edge. The mechanisms underlying the process of polarization are similarly diverse as the migratory machinery involved in different modes of cell motility. The signaling machinery involved in establishing front-rear identities in adhesive migration have been intensively studied [3]. Signaling molecules simultaneously increase actin nucleation and cross-linking and at the cell front while locally inhibiting the contractile activity of myosin II, thereby preventing the formation of large stress fibers and stabilizing the lamellipodium. At the cell rear, myosin is phosphorylated, generating contractile tension involved in detaching focal adhesions. For adhesion-independent cell movements, the mechanically relevant difference between rear and front results from the difference in myosin-dependent active stresses. The establishment of front-rear polarity in non-adhesive blebbing cell movement has been investigated in zebrafish primordial germ cells [111] and in other cells [82] (see also Figure 3.2 D). Briefly, fluctuations in the density of contractile material in the cortex, induced by either biochemical, i. e. regulatory, or mechanical, i. e. through cell body confinement, perturbations result in a symmetry breaking in the distribution of active contractile stresses, which due to the positive feedback between cortical flows, motor transport in the cortical layer and myosin-induced active stresses leads to the establishment of a stable front-rear gradient in active myosin distribution.

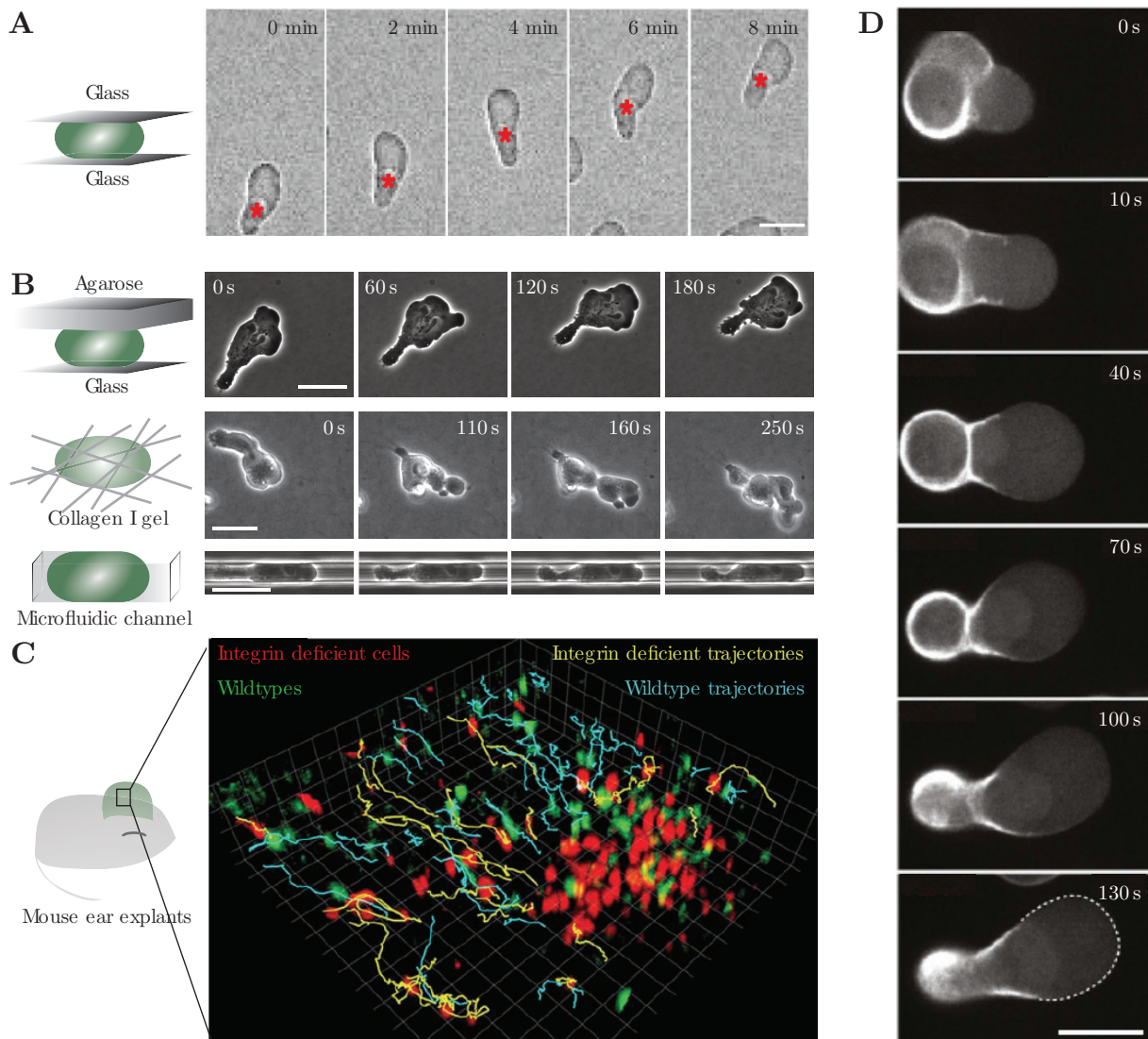


Figure 3.2: Various cell types are capable of non-adhesive cell migration in confined environments.

A. - C. Different cell types have been shown to migrate without specific substrate adhesions in confined environments *in vivo* and *in vitro*, including zebrafish germ layer progenitor cells (**A.**, image from [111]), carcinosarcoma cells (**B.**, image from [13]), and integrin-deficient dendritic cells (**C.**, image adapted from [73]). Scale bars: 20 μm . **D.** Cell polarization is achieved by establishing a stable gradient of active contractile tension in the cortex, as has been investigated in more detail in [111] and [82]. Here a zebrafish progenitor cell is shown with fluorescently labeled myosin II, exposed to a gradient of lysophosphatidic acid, an upstream regulator of myosin II. The induced symmetry breaking in the cortical contractility subsequently leads to a stable state with increased myosin density in the cell rear and a region devoid of cortical material in the cell front. Scale bar: 20 μm . Image from [111].

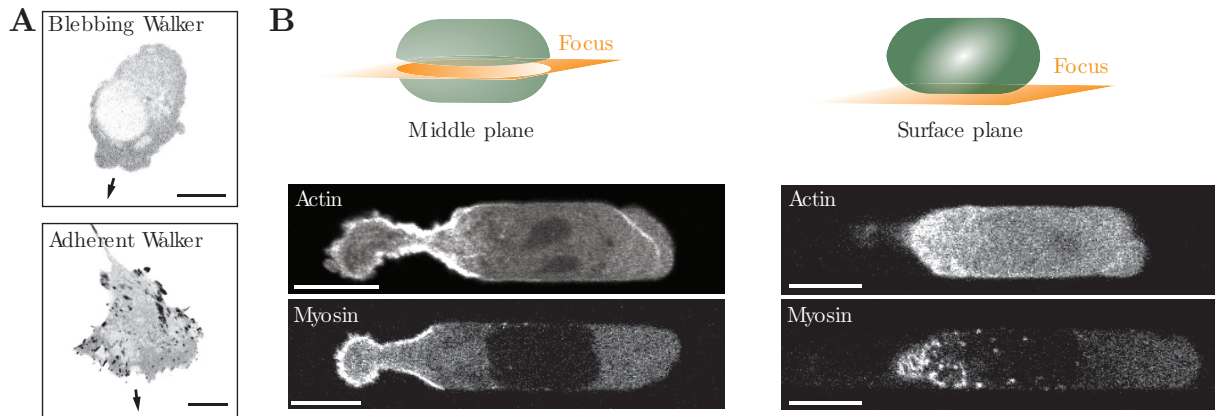


Figure 3.3: Blebbing Walker cells migrate without specific adhesions in microfluidic channels. **A.** Fluorescent labeling (Focal-Adhesion-Kinase-GFP) reveals no specific adhesive structures in blebbing Walker cells, while clearly visualizing focal adhesions in the adherent subline of Walker cells [12]. Images taken from cells migrating under agarose (top) or on glass (bottom), with arrows denoting the direction of movement. Scale bars: $10\ \mu\text{m}$. Panel also published in [13]. **B.** Blebbing Walker cells maintain a stationary gradient of actin and myosin density in the cortex, increasing towards the cell rear as visualized using fluorescence microscopy (LifeAct for actin and MRLC-GFP for myosin). Scale bars: $10\ \mu\text{m}$. Panel also published in [13].

3.2 Flows and forces during non-adhesive cell migration

Our goal is to understand the physics of adhesion-independent cell migration in confinement. We use continuum mechanics to describe the mesoscopic behavior of the involved cytoskeletal materials and compare our predictions to quantitative measurements combining live imaging and microfluidics. The work presented here is the result of a highly collaborative effort between our group and the lab of E. Paluch (UCL) and most results have been published in [13]¹. The experiments were performed on a non-adherent subline of rat cancer cells, which characteristically perform continuous blebbing (henceforth Walker cells). These cells polarize spontaneously, developing a blebbing side and a contracted side, but are unable to migrate on flat substrates or in suspension [11]. In confinement however, they move effectively and persistently, i. e. when placed under an agarose pad, inside a micropipette, or within collagen-I gels (see Figure 3.2 B). A number of experiments demonstrated that these cells move in the absence of any specific adhesion structures (see [13] for details). Figure 3.3 A shows the expression of fluorescent constructs, which localize to the adhesive structures in the cell, revealing stationary focal adhesions in adherent-subline Walker cells [12], but generating no signal in non-adherent blebbing Walker cells.

3.2.1 Observations of non-adhesive cell migration in microfluidic channels

When placed in microfluidic channels, the cells display a well defined, static morphology while migrating, featuring a blebbing leading edge, a cylindrical cell body and a contracted tail (Figure 3.2 B and 3.3 B). Fluorescence microscopy reveals that both filamentous actin and myosin II

¹M. Bergert (ETH Zurich, UCL previously) obtained the blebbing Walker cell line and performed all experiments presented here, with help from R. A. Desai (UCL) in the development of the microfluidic tools

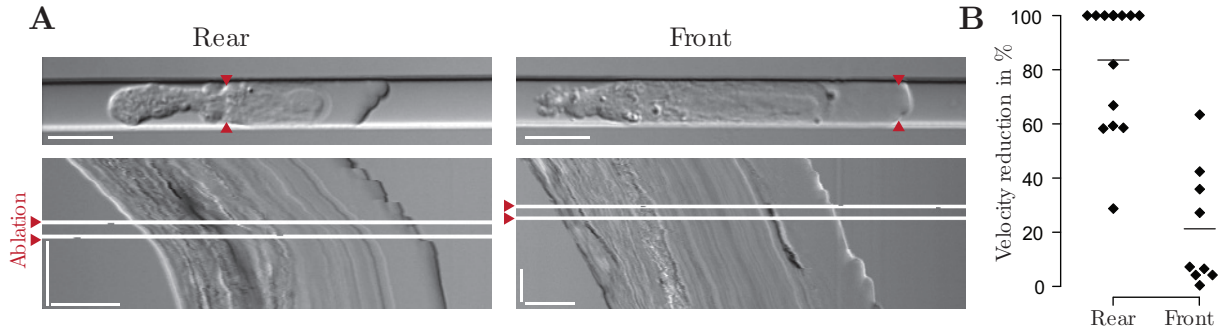


Figure 3.4: Cortical laser ablation experiments on migrating blebbing Walker cells.

A. Double laser ablation of the actomyosin cortex at the rear of the cell body, where the fluorescence intensities of both myosin and actin are highest, results in an instantaneous decrease in the migration velocity, a response not observed for ablations applied to the cell front, suggesting that blebbing Walker cell migration is driven by increased cortical contractility in the cell rear. Scale bars: 10 μm (horizontal), 50 s (vertical). Panel also published in [13]. **B.** Reduction of migration velocity in response to laser ablation applied to the cell rear ($N = 15$) and the cell front ($N = 9$). Migration velocity was significantly reduced upon actin network disruption in the rear part of the cell compared to ablation in the front. Panel also published in [13].

are enriched at the cell cortex and display a distinct concentration gradient increasing towards the cell rear (Figure 3.3 B). While cells are polarized, the actomyosin cortex continuously flows towards the rear of the cell. These flows are clearly visible due to a distinct cortical patterning: within the cell cortex, myosin enriches in small foci (Figure 3.3 B, right panels, and Figure 3.9 C), which appear near the middle of the cell and remain stationary for several minutes (see Figure 3.9 C). These observations suggest that myosin-dependent cortical contractility is increased in the cell rear in the polarized state, and may be relevant for moving the cell forward. Indeed, using a pulsed 405 nm laser, we ablated the cortical actin network in the cell rear and in the cell front, locally relaxing cortical contractility in the vicinity of the ablation spot [128], and found that disruption of the cortical actin network at the rear of the cell body strongly decreases cell velocity, while movement remains unaffected by ablation in the cell front (Figure 3.4).

3.2.2 Theoretical description of adhesion-independent cell migration

We developed a theoretical description of the mechanics of non-adherent blebbing Walker cells migrating in microfluidic channels. We describe the cell as an axisymmetric object confined in the channel with a contractile cortex at its surface, and consider the actin cortex as a thin layer of active, viscous fluid, subject to a spatially non-uniform internal contractile tension field. The internal contractile tension is generated by myosin II motor proteins and thus depends on the local concentration of phosphorylated myosin in the cell cortex. We assume that the profile of active tension is proportional to the profile of cortical myosin II fluorescence intensity, which we quantified from fluorescence microscopy images of migrating cells (see Figure C.1). During migration, myosin concentration is highest in the cell rear and decreases gradually towards the leading edge. A corresponding gradient in active tension can drive actomyosin flows in the cortical layer, and deformations of the cell surface. We assume that the cell shape is confined to a cylinder in the region where it is in contact with the microfluidic channel walls, and that the rear

and front pole regions are free to take the shape satisfying force balance (Figure 3.5). In addition to the stresses arising in the actomyosin cortex, we consider two external forces acting on the cell while it moves in the microfluidic channel. Frictional forces between the cortex and the channel walls arise, assuming that cortical flows in the contact region between the cell and the channel are resisted by a tangential friction force, proportional to the velocity of the flow relative to the channel wall. For example, transient binding and unbinding events between proteins at the cell surface and the channel coating may contribute to the friction coefficient. Furthermore, to take into account forces arising from the external medium, we introduce an effective drag coefficient arising from the motion of the external medium, which must flow around or through the cell, or be pushed forward as the cell moves. In Appendix A, we discuss the different contributions to the effective drag acting against cell motion in a channel. Following the approach outlined in Chapter 2, we derive and solve the equations governing the cell shape, the cell velocity and the cortical flow velocity profiles as functions of the mechanical and geometric parameters in the system. We find that the magnitude of the substrate friction coefficient is critical in determining the velocity of the moving cell. Above a threshold friction, myosin-dependent cortical flows produce sufficient thrust to propel the cell through the surrounding fluid, with the threshold friction coefficient depending on the drag coefficient and on the shape of the cell. In the following sections, we detail the model assumptions, and present the derivation and solution of the governing equations.

Main equations

Migrating Walker cells exhibit cortical flows on the timescale of minutes, exceeding the turnover rate of cortical crosslinkers (~ 20 s, [93]), at which elastic stresses in the actin network are released. Thus, we describe the cortex as a fluid layer, characterized by viscous coefficients. Furthermore, contractile stresses arising from the ATP driven activity of myosin motor proteins in the cortical actin network [30, 55] are captured by an active contractile tension term as detailed in Section 1.2.3. Since we could not detect any pattern of actin filament alignment in our observations of the actin architecture during blebbing Walker cell migration (see Figure 3.3 B, left), we take the actomyosin gel to be isotropic. Thus, the constitutive equation for the total tension tensor in the actomyosin cortex t^i_j is given by Equation 2.25. For simplicity, we assume here that the shear and bulk viscosities are related through $\eta_s = 2\eta_b = \eta$, corresponding to a ratio of bulk to shear viscosity $\eta_b/\eta_s = 1/2$, simplifying the constitutive relation to

$$t^i_j = \eta v^i_j + \zeta \delta^i_j. \quad (3.1)$$

As detailed in Section 2.2, the normal and tangential stresses arising from the intrinsic viscous and active tensions must balance pressures and shear stresses exerted by the medium surrounding the cortex. As derived, we obtain for the tangential force balance

$$\nabla_i t^{ij} = \Sigma_{\text{int}}^j - \Sigma_{\text{ext}}^j, \quad (3.2)$$

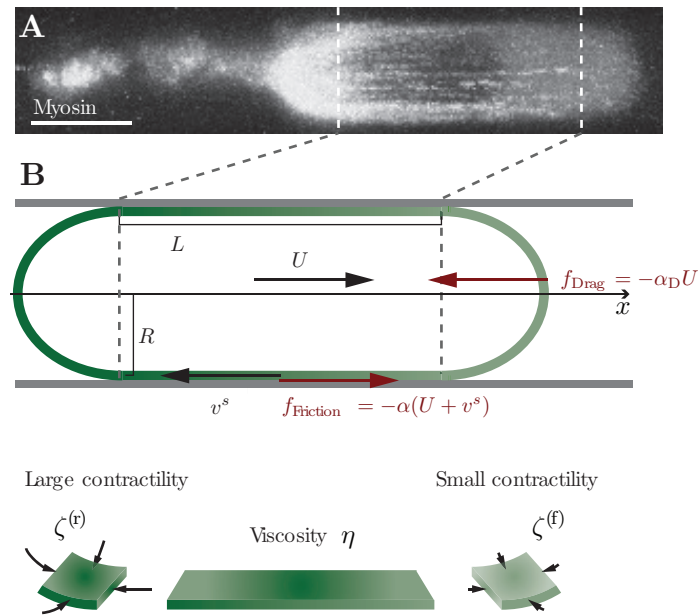


Figure 3.5: Parameters in the theoretical description of Walker cells in microfluidic channels. **A.** Time-averaged (3 min) and maximum intensity projected fluorescence microscopy image of a migrating Walker cell expressing fluorescent myosin II (MRLC-GFP). On timescales exceeding the period of bleb formation, the cell front exhibits a near-hemispherical shape. Scale bar: $10\ \mu\text{m}$. Panel also published in [13]. **B.** Schematic representation of the theoretical description and its parameters. The cell is confined to a cylinder with radius R where in contact with the channel wall. The length of the contact region is given by L . The cell cortex is taken as an axisymmetric fluid surface with a viscosity η , which is subject to the internal active tension ζ . In proportion with the density of myosin II motors, the active tension field decreases from the cell rear towards the cell front, i. e. $\zeta^{(r)} > \zeta^{(f)}$. The active tension gradient drives a retrograde flow within the cortical layer v^s , which gives rise to a frictional force density f_{Friction} acting on the contact area with the channel wall. For sufficiently large friction, the cell is propelled at velocity U through the external fluid in the channel against the fluid drag force f_{Drag} . The friction and drag forces are characterized by the coefficients α and α_D respectively. Similar panel published in [13].

where Σ_{int} and Σ_{ext} are the shear stresses acting on the cortex from the intracellular and extracellular sides. The normal force balance reads

$$C_{ij}t^{ij} = P_{\text{int}} - P_{\text{ext}}, \quad (3.3)$$

which is simply the Young-Laplace equation, with P_{int} the intracellular pressure, P_{ext} the extracellular pressure, such that $P_{\text{int}} - P_{\text{ext}}$ is the pressure drop across the surface. In what follows we assume that the shear stress Σ_{int} acting on the surface from inside the cell can be neglected compared to viscous and active stresses acting within the surface. In Appendix B, we consider an alternative case where an internal friction acts on the cortex resulting from the presence of the nucleus and other dense material inside the cell. The external shear stress Σ_{ext} and the pressure drop $P_{\text{int}} - P_{\text{ext}}$ have different values in the cylindrically confined part of the cell and in the pole regions. In the region where the cell is in contact with the channel walls, an external shear stress Σ_{ext} acts on the surface, which is proportional to the relative velocity between the flowing cortex and the channel. Expressing this proportionality, we write $\Sigma_{\text{ext}} = -\alpha v^s$, with α the associated friction coefficient (see Figure 3.5 B). The tangential force balance then has the simple expression

$$\partial_s t^s_s = \alpha v^s. \quad (3.4)$$

Furthermore, in the cylindrically confined cell part, the shape of the cell is constrained by the channel wall, and the normal force balance Equation 3.3 thus simply yields the pressure exerted by the cell on the channel, which in fact has no direct mechanical effect on cell migration, since in this region, forces normal to the cell surface are perpendicular to the direction of cell displacement and therefore do not contribute to propelling the cell. For a cell migrating at some velocity U , it is convenient to rewrite Eq. 3.4 in the reference frame of the moving cell

$$\partial_s t^s_s = \alpha(v^s + U), \quad (3.5)$$

where v^s is now a velocity taken in the cell reference frame. Together with the constitutive Equation 3.1, we obtain the following equation for the cortical flow velocity in the cylindrically confined cell region

$$\eta \partial_s^2 v^s = \alpha(v^s + U) - \partial_s \zeta, \quad (3.6)$$

which can be readily solved for a given profile of the active stress ζ . In the pole regions, where the cell is not confined and in contact with the medium in the microfluidic channel, we neglect external shear stresses. These may arise from the viscosity of the surrounding fluid, which however is very small (of the order of the viscosity of water, $\eta_{\text{ext}} \approx 10^{-3} \text{Pa}\cdot\text{s}$) compared to cytoskeletal viscosities. Therefore, the tangential and normal force balance equations 3.2-3.3 read

$$\partial_s t^s_s + \frac{\cos \psi}{r} (t^s_s - t^\phi_\phi) = 0 \quad (3.7)$$

$$\partial_s \psi t^s_s + \frac{\sin \psi}{r} t^\phi_\phi = P_{\text{int}} - P_{\text{ext}}. \quad (3.8)$$

Combining these equations with Eq. 3.1, we obtain the equations governing the velocity in the cortical layer, and shape of the cell in the unconfined pole regions. We take the active tension to be uniform in the pole surfaces, implying $\partial_s \zeta = 0$, and assume that the cell shape is in a stationary state, such that the normal velocity v^n vanishes (see Section 2.4). The resulting equations read

$$\partial_s^2 v^s + \frac{\cos \psi}{r} \left(\partial_s v^s - \frac{\cos \psi}{r} v^s \right) = 0 \quad (3.9)$$

$$\left(\partial_s \psi + \frac{\sin \psi}{r} \right) \zeta + \eta \left(\partial_s \psi \partial_s v^s + \frac{\sin \psi \cos \psi}{r^2} v^s \right) = P_{\text{int}} - P_{\text{ext}}. \quad (3.10)$$

Our observations of blebbing Walker cells migrating in microfluidic channels support the notion of a Galilean invariant stationary system (see Figure 3.9 C).

Profile of cortical flow velocity

We now proceed to obtain the solutions for the flow fields in the cylindrical and the pole cell regions. It is convenient to introduce the following coordinates used in the different cell parts, where the superscripts (r), (m) and (f) denote rear, middle and front cell region respectively (see Figure 3.6 A)

$$\theta^{(r)} = \frac{s}{R} \quad \text{in the rear pole region,} \quad (3.11)$$

$$x^{(m)} = s - R \frac{\pi}{2} \quad \text{in the contact region,} \quad (3.12)$$

$$\theta^{(f)} = \pi - \frac{s - L}{R} \quad \text{in the front pole region.} \quad (3.13)$$

We denote by R and L the radius of the microfluidic channel and the length of the contact area between channel and cell (see Figure 3.5 B). Walker cell motility in microfluidic channels relies on the polarized distribution of myosin motors within the cell cortex. The accumulation of myosin in the cell rear (see Figure 3.5 A) gives rise to a spatial profile of active tension $\zeta(x)$, decreasing from the cell rear to the front. We begin with the simple case of a piecewise linear profile of active tension (see Figure 3.6 B)

$$\zeta = \begin{cases} \zeta^{(r)} & \text{in the rear pole region} \\ \zeta^{(r)} - \frac{\zeta^{(r)} - \zeta^{(f)}}{L} x^{(m)} & \text{in the contact region} \\ \zeta^{(f)} & \text{in the front pole region} \end{cases} \quad (3.14)$$

For the calculations in Section 3.2.3, we evaluate more precisely the active tension profile by assuming a proportionality relation between the active tension and the myosin intensity profile $I(x)$, $\zeta(x) = \zeta^{(0)} I(x)$ (see Appendix C), in line with previous studies [86, 119, 7], and compare the resulting flow fields to the measured data from migrating cells. For a linear active tension profile, the general solution to Equation 3.6 for the cortical flow velocity in the cylindrical part

of the cell is given by

$$v^s = C_1 \exp\left(\frac{x^{(m)}}{l}\right) + C_2 \exp\left(-\frac{x^{(m)}}{l}\right) - U - \frac{\zeta^{(r)} - \zeta^{(f)}}{\alpha L} \quad \text{for } s \in [R\frac{\pi}{2}, R\frac{\pi}{2} + L], \quad (3.15)$$

where $l = \sqrt{\eta/\alpha}$ is a hydrodynamic length characterizing the range of cortical flows (see Figure 3.6 C). The integration constants C_1 and C_2 will be determined from the boundary conditions on the velocity and tension at the contact points where the pole regions are connected to the cylindrical part of the cell, as detailed below.

In the pole regions, the coupled non-linear Equations 3.9 - 3.10 govern the flow and the shape of the cell surface. To solve these equations, we perform an expansion around an unpolarized cell state where the active tension is uniform along the entire cell, in which case no flow arises in the cortex. The rear and front surfaces then take the shape of hemispherical caps. Without loss of generality, we present here only the solutions for the rear part of the cell, however the expressions in the front can be found by a simple symmetry transformation. For the cell rear, Eq.'s 3.9 - 3.10 and the appropriate boundary conditions ensuring the continuity of the shape and flow profiles, are solved by $v^s = 0$, $r = R \sin(s/R)$, $\psi = s/R$, with the pressure drop across the cell surface given by $P_{\text{int}}^{(r)} - P_{\text{ext}}^{(r)} = 2\zeta^{(r)}/R$. We linearize the shape and flow equations around this solution ($v^s = \delta v^s$, $\psi = s/R + \delta\psi$, $r = R \sin(s/R) + \delta r$, $P_{\text{int}}^{(r)} - P_{\text{ext}}^{(r)} = 2\zeta^{(r)}/R + \delta P$). This expansion is valid in the limit where the variation of active tension is small compared to the average cellular surface tension $(\zeta^{(r)} - \zeta^{(f)})/\bar{t} \ll 1$, where the average cellular surface tension \bar{t} includes both the average cortical tension and the cell membrane tension. For the Walker cells studied here, the total surface tension has been measured to be $279 \pm 50 \text{ pN } \mu\text{m}^{-1}$ [12]. Our final estimate of $\zeta^{(r)} - \zeta^{(f)} = 68 \pm 7 \text{ pN } \mu\text{m}^{-1}$ (see Section 3.2.3, Table 3.2) is thus consistent with the above assumption. Furthermore, the observed time-average cell shape in the pole regions indeed corresponds approximately to a hemisphere (see Figure 3.5 A).

Neglecting higher order terms and using 3.11, Equations 3.9-3.10 become

$$\left(\partial_\theta^2 + \cot\theta^{(r)}\partial_\theta - \cot^2\theta^{(r)}\right)\delta v^s = 0 \quad (3.16)$$

$$\left(\partial_\theta^2 + 1\right)\delta r = -\frac{\delta P R^2}{\zeta^{(r)}}\sin\theta^{(r)} + \frac{\eta}{\zeta^{(r)}}\partial_\theta(v^s \sin\theta^{(r)}). \quad (3.17)$$

In the partial derivatives, θ stands for $\theta^{(r)}$. The solution of Equation 3.16 is a linear combination of the associated Legendre polynomials $\mathcal{P}_\nu^1(\cos\theta^{(r)})$ and $\mathcal{Q}_\nu^1(\cos\theta^{(r)})$, with $\nu(\nu+1) = 1$. The solution cannot diverge in $\theta^{(r)} = 0$, therefore, $\mathcal{Q}_\nu^1(\cos\theta^{(r)})$ is not part of the solution and the velocity and tension profiles are given by

$$v^s = v^{(r)} \frac{\mathcal{P}_\nu^1(\cos\theta^{(r)})}{\mathcal{P}_\nu^1(0)} \quad (3.18)$$

$$t_s^s = \zeta^{(r)} + \eta \frac{v^{(r)}}{R} \frac{\partial_\theta \mathcal{P}_\nu^1(\cos\theta^{(r)})}{\mathcal{P}_\nu^1(0)} \quad (3.19)$$

where we denote by $v^{(r)}$ the cortical velocity at the contact point between the cell surface and the channel wall (see Figure 3.6 C). In the front pole region, the solutions for the cortex velocity

and the tension read

$$v^s = v^{(f)} \frac{\mathcal{P}_\nu(\cos \theta^{(f)})}{\mathcal{P}_\nu(0)} \quad (3.20)$$

$$t^s_s = \zeta^{(f)} - \eta \frac{v^{(f)}}{R} \frac{\partial_{\theta^{(f)}} \mathcal{P}_\nu(\cos \theta^{(f)})}{\mathcal{P}_\nu(0)} \quad (3.21)$$

The unknown constants C_1 , C_2 , $v^{(r)}$ and $v^{(f)}$ are obtained by imposing that the velocity and tension fields have to be continuous at the contact points (see Figure 3.6)

$$C_1 + C_2 - U - \frac{\zeta^{(r)} - \zeta^{(f)}}{\alpha L} = v^{(r)} \quad (3.22)$$

$$\frac{C_1 - C_2}{l} = \frac{v^{(r)}}{R} \frac{\partial_{\theta^{(r)}} \mathcal{P}_\nu^1(\cos \theta^{(r)})|_{\theta^{(r)}=\pi/2}}{\mathcal{P}_\nu^1(0)} \quad (3.23)$$

$$C_1 \exp\left(\frac{L}{l}\right) + C_2 \exp\left(-\frac{L}{l}\right) - U - \frac{\zeta^{(r)} - \zeta^{(f)}}{\alpha L} = v^{(f)} \quad (3.24)$$

$$\frac{C_1 \exp\left(\frac{L}{l}\right) - C_2 \exp\left(-\frac{L}{l}\right)}{l} = -\frac{v^{(f)}}{R} \frac{\partial_{\theta^{(f)}} \mathcal{P}_\nu^1(\cos \theta^{(f)})|_{\theta^{(f)}=\pi/2}}{\mathcal{P}_\nu^1(0)}. \quad (3.25)$$

To close the system of equations, we must obtain an expression for the cell velocity U . For this, we will first consider the shape of the cell in the unconfined pole regions at the front and the rear.

Cell shape in the pole regions

Integrating Equation 3.17 yields a general solution for the shape in the rear pole region of the cell. Imposing the boundary conditions $\partial_\theta \delta r = 0$ at $\theta^{(r)} = 0$, $\partial_\theta \delta r = 0$ at $\theta^{(r)} = \pi/2$ and $\delta r(\pi/2) = 0$ at $\theta^{(r)} = \pi/2$, which ensure that the shape is smooth at the cell pole and at the contact point to the channel, we obtain

$$\begin{aligned} \delta r = & \frac{\eta}{\zeta^{(r)}} v^{(r)} \left(a \left(\cos \theta^{(r)} (\theta^{(r)} - \frac{\pi}{2}) - \sin \theta^{(r)} \right) - \left(\int_0^{\frac{\pi}{2}} \cos \theta' \sin \theta' \frac{\mathcal{P}_\nu^1(\cos \theta')}{\mathcal{P}_\nu^1(0)} d\theta' - 1 \right) \cos \theta^{(r)} \right) \\ & + \frac{\eta}{\zeta^{(r)}} v^{(r)} \int_0^{\theta^{(r)}} \cos(\theta^{(r)} - \theta') \frac{\mathcal{P}_\nu^1(\cos \theta')}{\mathcal{P}_\nu^1(0)} \sin \theta' d\theta', \end{aligned} \quad (3.26)$$

and for the pressure drop across the cell surface

$$P_{\text{int}}^{(r)} - P_{\text{ext}}^{(r)} = \frac{2\zeta^{(r)}}{R} + \frac{2\eta}{R^2} v^{(r)} a, \quad (3.27)$$

where we have introduced the numerical coefficient $a = \int_0^{\frac{\pi}{2}} d\theta' \sin^2 \theta' \frac{\mathcal{P}_\nu^1(\cos \theta')}{\mathcal{P}_\nu^1(0)}$. For the cell front, the pressure difference reads

$$P_{\text{int}}^{(f)} - P_{\text{ext}}^{(f)} = \frac{2\zeta^{(f)}}{R} - \frac{2\eta}{R^2} v^{(f)} a. \quad (3.28)$$

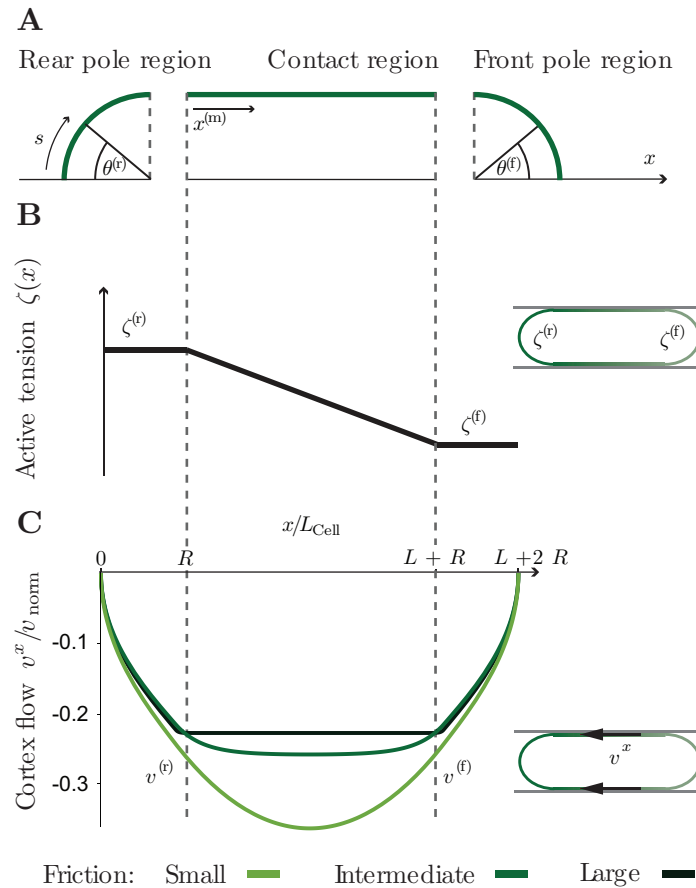


Figure 3.6: Description of cortical flows in migrating Walker cells.

A. Coordinates used in the pole and contact regions of the cell. **B.** Profile of active tension along the cell axis in the actomyosin cortex. A linear profile, decreasing from the rear towards the front of the cell was used for the general calculations (see Equation 3.14). **C.** Cortical flow velocity for a linear active tension profile and different values of the channel friction coefficient α , shown in the reference frame of the moving cell. $v_{\text{norm}} = (\zeta^{(r)} - \zeta^{(f)})L/\eta$. Similar panel published in [13].

See Figure 3.7 A for an overview of the pressures acting on the migrating cell. We can now obtain the solution for the velocity of the migrating cells by considering the balance of pressure inside the cell and in the fluid medium contained in the channel.

Cell velocity

The cytoplasm has been described as a poroelastic material with a rheological timescale below one second (e.g. in [88]). Accordingly, equilibration of intracellular pressure differences can be assumed fast compared to the timescales of cell motion, and the hydrostatic pressure inside the cell can be taken uniform

$$P_{\text{int}}^{(r)} = P_{\text{int}}^{(f)}. \quad (3.29)$$

From this relation, Equations 3.22 - 3.25 and Equations 3.27 - 3.28, an expression can be obtained for the the cell velocity of the following form

$$U = U_0 + \frac{1}{\chi}(P_{\text{ext}}^{(r)} - P_{\text{ext}}^{(f)}). \quad (3.30)$$

with U_0 defined as the intrinsic velocity the cell would achieve in the absence of any external resistance to cell motion, given by

$$U_0 = \frac{L(\zeta^{(r)} - \zeta^{(f)})}{\eta} \left(\frac{l}{2L} \frac{\exp\left(\frac{L}{l}\right) + 1}{\exp\left(\frac{L}{l}\right) - 1} + \frac{R}{2aL} - \frac{l^2}{L^2} \right), \quad (3.31)$$

and χ an effective cell friction,

$$\chi = \frac{a4\eta \left(\exp\left(\frac{L}{l}\right) - 1 \right)}{R \left(al - R + \exp\left(\frac{L}{l}\right) (al + R) \right)}. \quad (3.32)$$

The flow-velocity relationship predicted by Equation 3.30 is shown in Figure 3.7 B. The cell moves with a spontaneous cell velocity U_0 in the absence of any external force. In a fluid-filled channel subjected to a zero pressure difference at its boundaries, as corresponds to our experimental setup, the only contribution to the difference of pressure acting on the cell $P_{\text{ext}}^{(r)} - P_{\text{ext}}^{(f)}$ results from the drag of the medium acting against the motion of the cell. We assume here that the external pressure opposing cell movement is proportional to the cell velocity and can be written in terms of an effective drag coefficient α_D

$$P_{\text{ext}}^{(r)} - P_{\text{ext}}^{(f)} = -\alpha_D U. \quad (3.33)$$

Note that such a proportionality relation between the pressure difference on the cell and the cell velocity does not necessarily hold. Indeed, the drag depends also on the motion of the fluid in the channel. For instance, an externally applied pressure difference at the channel boundaries, generating a fluid flow, would modify Eq. 3.33. In Appendix A, we show that under the experimental conditions in this work, the pressure acting on the cell can be expressed in the form of Eq. 3.33, and we detail how the value of α_D is related to the flow permeability of the

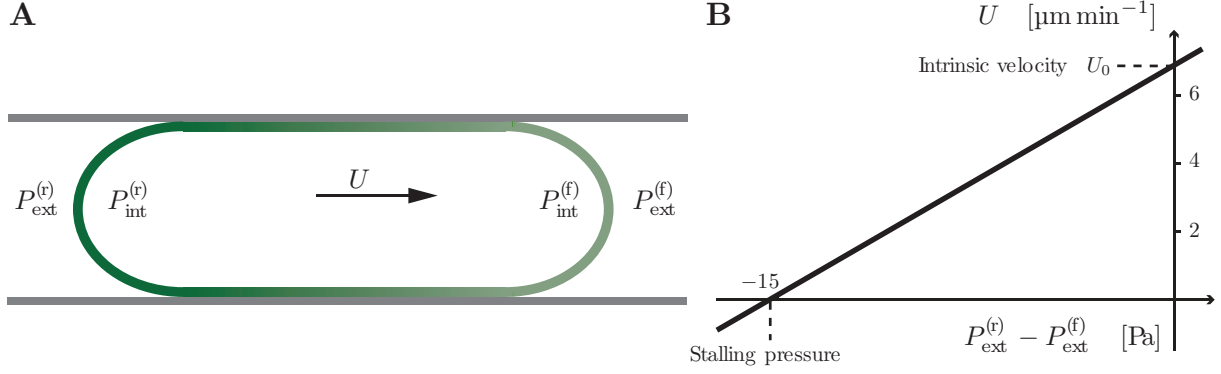


Figure 3.7: External pressure and cell velocity.

A. Schematic illustration of the intracellular and extracellular pressures acting on migrating Walker cells. **B.** Relationship between the velocity of a cell and the external pressure difference acting on the rear and front of the moving cell (see Equation 3.30). In the absence of any external dissipation, the cell moves at the intrinsic velocity U_0 . This figure is plotted for the parameters listed in Table 3.1 estimated for non-adhesive Walker cells in microfluidic channels. The predicted cell stalling pressure -15 Pa is several orders of magnitude lower than reported values for adhesive cells moving in microfluidic channels [131], consistent with the differences in traction forces. Similar panels published in [13].

channel and the migrating cells.

Using Equation 3.33, we solve Equation 3.30 for the cell velocity U , obtaining

$$U = \frac{2(\zeta^{(r)} - \zeta^{(f)})(al(2l + L + \exp\left(\frac{L}{l}\right)(L - 2l)) + (\exp\left(\frac{L}{l}\right) - 1)LR}{L(alR\alpha_D - R^2\alpha_D - 4a\eta + \exp\left(\frac{L}{l}\right)(R(al + R)\alpha_D + 4a\eta))}. \quad (3.34)$$

This expression describes the cell velocity as a function of the hydrodynamic length l , the cell geometric parameters R and L , the gradient of active tension $(\zeta^{(r)} - \zeta^{(f)})/L$ and the external drag α_D . Figure 3.10 B shows the predicted cell velocity as a function of the friction coefficient α . For small friction compared to the external drag $\alpha \ll \alpha_D$, the velocity U vanishes, as the resistance to cortical flow is not sufficient to propel the cell.

Threshold friction for cell movement As shown in Figure 3.10, the cell velocity U exhibits two different regimes for small and large friction α . In this section, we perform an approximate calculation of the threshold friction above which cells are able to achieve nonzero migration velocities. To this end, we expand U around the limit of zero friction ($l/L \rightarrow \infty$)

$$U = \frac{(\zeta^{(r)} - \zeta^{(f)})L(aL + 6R)}{6aR\alpha_D l^2} - \frac{(\zeta^{(r)} - \zeta^{(f)})L^2(30\alpha_D R^3 + 10aR(LR\alpha_D + 12\eta) + a^2L(LR\alpha_D + 20\eta))}{60(aR\alpha_D)^2 l^4} + \mathcal{O}\left(\frac{1}{l^5}\right). \quad (3.35)$$

The second term is negative and is responsible for the cell velocity leveling off as the friction coefficient α is increased. The ratio of the first two terms in the expansion therefore defines a

critical hydrodynamic length l^* , below which friction is not sufficient to drive cell movement

$$\left(\frac{l^*}{L}\right)^2 = \frac{R}{2La} + \frac{1}{60} \left(5 + \frac{aL}{aL + 6R}\right) + \frac{2\eta}{LR\alpha_D}. \quad (3.36)$$

For the fitted values of η and α_D (see Section 3.2.3 and Tables 3.1 - 3.2), the last term dominates $(l^*/L)^2 \approx 2\eta/(LR\alpha_D)$. Thus, we find the following expression for the critical friction coefficient enabling cell movement

$$\alpha^* \approx \frac{R\alpha_D}{2L}. \quad (3.37)$$

To estimate more precisely the critical friction for cell motion, we numerically evaluated the first inflection point of $U(\alpha)$, for different values of α_D (Figure 3.8), and find that the approximation Eq. 3.37 yields a very good estimate for the inflection point of $U(\alpha)$ in the regime of small drag coefficients. Eq. 3.37 indicates that the cell velocity is critically dependent on the ratio of the friction to drag coefficient, α^*/α_D . Cell locomotion can only be achieved provided that the friction coefficient is of the same order or larger than the drag coefficient. This very simple criterion provides a quantitative prediction for conditions enabling cell motion driven by cortical flow and friction. To summarize, we have calculated the cell

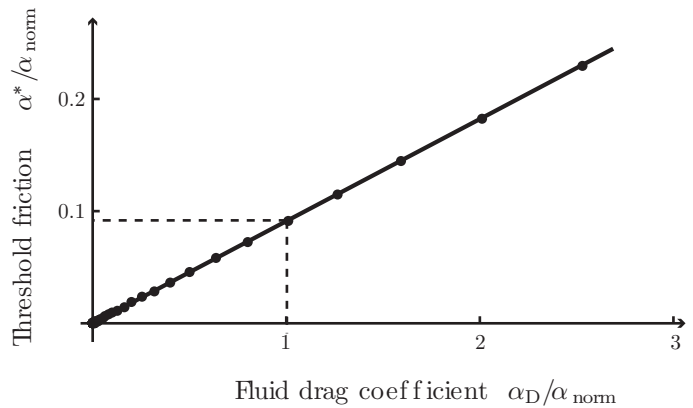


Figure 3.8: Comparison between the numerically computed threshold friction (dots), and the approximate estimate $\alpha^* \approx R\alpha_D/(2L)$ (line). Dashed lines indicate the value of α^* estimated for migrating Walker cells in microfluidic channels, and α_{norm} is the fluid drag coefficient for this case, as obtained from the fitting procedure (see Table 3.1). Similar panel published in [13].

velocity U and the rearward cortical flow field v^s resulting from a gradient of active cortical tension, and we find that cortical flows enable cell movement at a finite velocity only if sufficient substrate friction is available to overcome fluid drag. Our predictions on cortical flows and cell velocities at different friction coefficients can be directly compared to experimental measurements.

3.2.3 Cell velocity and cortex flows depend critically on the substrate friction

Varying and measuring the friction coefficient

As our calculations suggest that a threshold friction exists, below which the cell cannot move forward (Figure 3.10 B), we sought to test this behavior experimentally by modifying and measuring the friction coefficient present in the microfluidic channels. To vary the surface properties of the channels, we coated the walls with different chemical compounds. The observations summarized in Section 3.2.1 were made in channels treated with bovine serum albumin (BSA), a

non-adhesive compound, which may give rise to non-specific friction by means of weak molecular interactions with cell surface proteins (for a discussion of the origin of friction, see Section 3.3.2). For comparison, we functionalized a set of channels with Pluronic F127, a derivative of polyethylene glycol, known to provide a non-adhesive substrate with low friction [20]. To obtain channels with intermediate friction, we applied a mixture of BSA and F127.

In channels coated with F127, cells were unable to migrate, while nonetheless remaining polarized, continuously forming blebs. Moreover, following the motion of fluorescent myosin foci in the cortex, we observed cortical flows towards the contracted tail region of the cells, similar to the BSA condition. In the intermediate channels, cell velocities were significantly lower than in purely BSA treated channels, where cells achieved an average velocity of $7.6 \pm 0.5 \mu\text{m min}^{-1}$, compared to $5.2 \pm 0.4 \mu\text{m min}^{-1}$ for BSA/F127 cells (sample sizes: $N_{\text{BSA}} = 18$ and $N_{\text{BSA/F127}} = 25$, error: standard error of the mean, $p < 0.01$). Furthermore, we observed slippage between the cortex and the channel walls in BSA/F127 experiments (see Figure 3.9 C).

To quantitatively assess whether these coatings modulate friction between the cell and the channel surface in our setup, we developed a microfluidic assay to directly measure the friction coefficient, consisting of a long, narrow channel, which we coated in the same way as the microfluidic channels used to observe cell migration behaviors. The device allows for the introduction of individual cells into the channel. Upon application of a set of controlled pressure differences, we monitored the resulting velocities of single cells, propelled by the fluid flow (Figure 3.9 A). The ratio between the pressure-induced free flow in the channel and the cell velocities allows to extract the friction coefficient between the cells and the channel in the velocity range relevant to the migration of blebbing Walker cells. Friction measurements were performed on unpolarized cells, which did not display any motility. To estimate the friction, we first measured the average free flow velocity $\bar{v}_{\text{ext,free}}$ in the channel without cells, generated by the applied pressure difference $P_{\text{applied}} = P_{\text{in}} - P_{\text{out}}$ by monitoring the motion of fluorescent microbeads in the fluid. The free flow velocity is proportional to the applied pressure

$$P_{\text{applied}} = \xi_{\text{ext}} \pi R^2 \bar{v}_{\text{ext,free}}, \quad (3.38)$$

where $\xi_{\text{ext}} = 8\eta_{\text{ext}}L_{\text{ext}}/(R^4\pi)$ is the hydraulic resistance of the channel, with η_{ext} the viscosity of water and L_{ext} the length of the channel. After introducing a single cell into the channel, we measured its velocity U at the same applied pressure P_{applied} . The cell velocity is related to the friction coefficient α and to the applied pressure through the following equation

$$P_{\text{applied}} = \left(\left(\frac{\xi_{\text{ext}}}{\xi} + 1 \right) \frac{2L\alpha}{R} + \xi_{\text{ext}} \pi R^2 \right) U. \quad (3.39)$$

Here, ξ refers to the flow resistance of a channel segment containing a cell (see Figure 3.11 A). In Appendix A, we discuss in more detail the hydraulics of the channel-cell system and present the derivation of Eq. 3.39. The hydraulic resistance of the cell ξ was estimated self-consistently together with the fitting procedure for cellular retrograde flows, as explained in the next section. Using this estimate, we computed the friction coefficients in different conditions from Eq. 3.39. We find that the friction coefficients of BSA, F127 and mixed channels differ by several orders of

magnitude, with BSA providing a large friction environment, which is decreased by the addition of F127, and a very low friction coefficient for purely F127 coated channels (see Figure 3.9 B). These results show that cell migration velocity depends strongly on the magnitude of substrate friction present in the microfluidic channels, as predicted by our calculations.

Cortical flow profiles in different friction conditions - Comparison between theory and experiments

To further compare the theoretical predictions to experimental measurements of Walker cells migrating in microfluidic channels, we analyzed in more detail the cortical flow fields in the different friction conditions. We estimated the cortical actomyosin flow fields from time-lapse images of migrating cells with fluorescent myosin II, taken at 2 s intervals in the focal plane of the cell cortex (see Figure 3.9 C and Appendix C). We applied a particle image velocimetry algorithm ([86]), obtaining an estimate of the velocity of traceable structures by computing the cross-correlation between subsequent images. The distinct patterning of the cortex in blebbing Walker cells, featuring clear, stationary myosin spots, allowed for the accurate extraction of flow fields in the rear part of the cells (see Figure 3.10 C). Furthermore, we quantified the distribution of fluorescent myosin II in the cortex of migrating Walker cells, to use the profile of fluorescence intensity as an estimate of the myosin-dependent active tension field (see Appendix C). Specifically, we introduce a scaling factor $\zeta^{(0)}$ connecting the relative myosin fluorescence intensity to the active tension ζ

$$\zeta(x) = \zeta^{(0)} \frac{I_{\text{top}}(x) - I_{\text{middle}}(x)}{\bar{I}} \quad (3.40)$$

where $I_{\text{top}}(x)$ and $I_{\text{middle}}(x)$ are the fluorescence intensity profiles in the focal plane adjacent to the channel wall and at the center of the cell (see Figure C.1). \bar{I} is the average fluorescence intensity in a region of the image at the front of the cell where both middle and top planes are devoid of bright myosin foci. We remove the cytoplasmic fluorescence signal contained in $I_{\text{top}}(x)$ by subtracting $I_{\text{middle}}(x)$, thereby achieving a better readout of the active, cortical myosin density.

For an arbitrary active tension profile $\zeta(x)$, the cortical velocity in the cylindrically confined cell part reads (as follows from Eq. 3.5)

$$\begin{aligned} v^s = & C_1 \exp\left(\frac{x^{(m)}}{l}\right) + C_2 \exp\left(-\frac{x^{(m)}}{l}\right) - U \\ & - \frac{1}{2\eta} \left(\exp\left(\frac{x^{(m)}}{l}\right) \int_{x_0}^{x^{(m)}} \exp\left(-\frac{x'}{l}\right) \zeta(x') dx' + \exp\left(-\frac{x^{(m)}}{l}\right) \int_{x_0}^{x^{(m)}} \exp\left(\frac{x'}{l}\right) \zeta(x') dx' \right). \end{aligned} \quad (3.41)$$

To obtain a noise-reduced estimate of $\zeta(x)$, we approximated the myosin fluorescence intensity profiles with a fifth-degree polynomial, where the six free coefficients were determined by minimizing the sum of squared errors between the curve and the fluorescence intensity data points. The resulting expression was used to analytically evaluate the integrals of $\zeta(x)$ in Eq. 3.41.

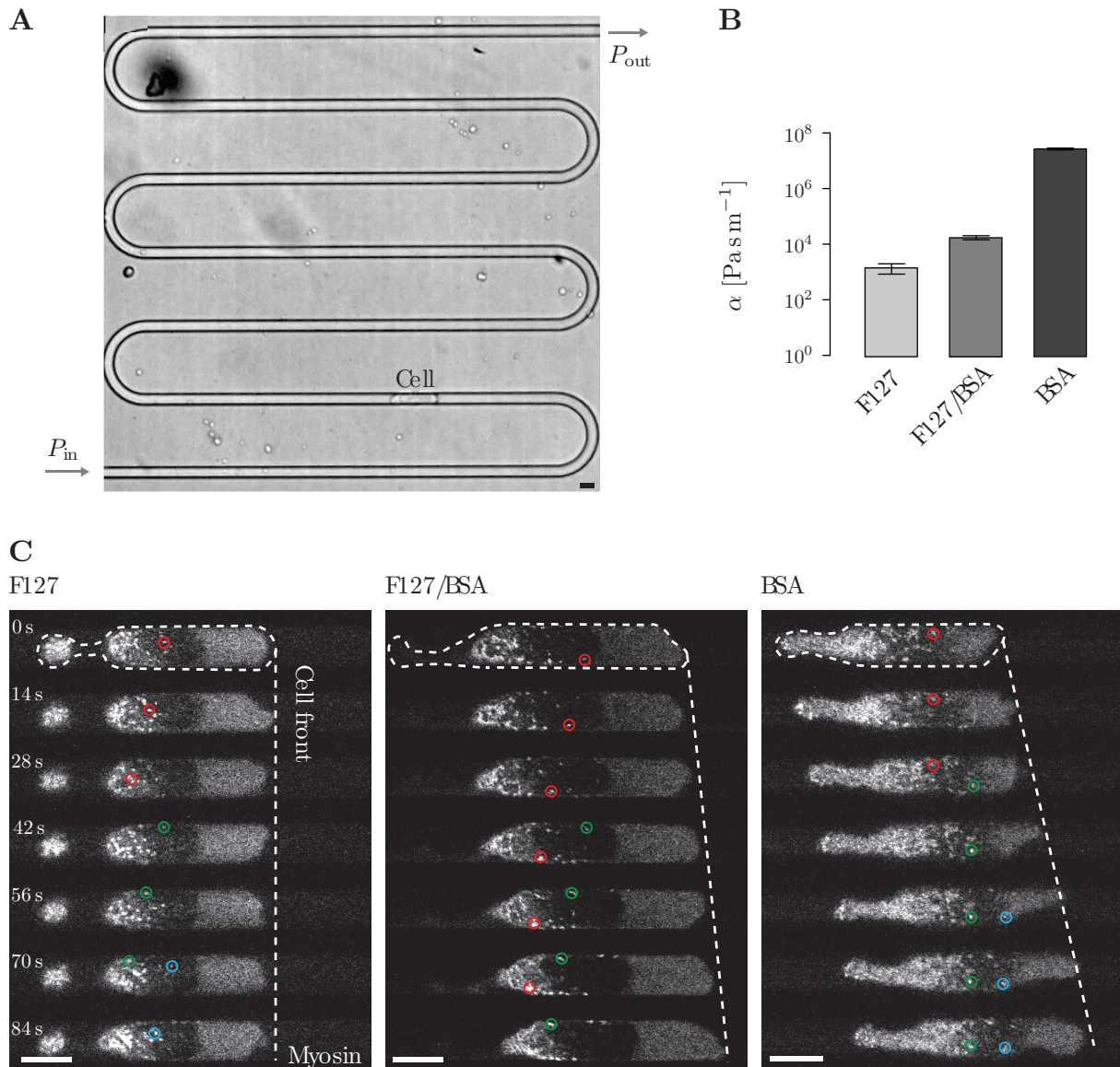


Figure 3.9: Varying and measuring the friction coefficient.

A. Microfluidic channel used to measure the friction coefficient between an inserted Walker cell and channel walls treated with different coatings (BSA, F127). A controlled pressure difference $P_{\text{in}} - P_{\text{out}}$ is applied to the channel inlet and outlet, and the resulting velocity of the cell is recorded. The friction coefficients are then calculated as described in Section 3.2.3, see also Appendix A. The microfluidic setup was assembled by M. Bergert and R. A. Desai, based on [103]. Scale bar: $10\ \mu\text{m}$. **B.** Friction coefficients measured in channels coated with F127 ($N = 9$), a 40:60 mixture of F127:BSA ($N = 10$) and BSA ($N = 9$). Sample sizes are given in brackets, error bars denote the standard error of the mean. We find that treatment with F127 and BSA create environments with small and large friction coefficients respectively. Panel also published in [13]. **C.** Time lapse fluorescence images of Walker cells migrating in low (left panels), intermediate (middle panels), and large friction channels (right panels). Images are taken in the focal plane of the cortex, with myosin II labeled fluorescently. Individual myosin foci are circled in color to highlight the flow of the cortex relative to the channel walls. In F127 coated channels, the frictional forces are not sufficient to propel the cell forward, but polarity state, morphology and cortical flows persist. At intermediate friction values, the cells achieve a velocity of $5.2 \pm 0.4\ \mu\text{m}\ \text{min}^{-1}$, but slippage between the cortex and the channel walls is still present. In large friction conditions, the cortex is stationary with respect to the channel walls and the cells move at $7.6 \pm 0.5\ \mu\text{m}\ \text{min}^{-1}$. Scale bars: $10\ \mu\text{m}$. Similar panel published in [13].

Parameter	Value
Large friction α	$27 \pm 2 \times 10^6 \text{ Pa s m}^{-1}$
Intermediate friction α	$18 \pm 3 \times 10^3 \text{ Pa s m}^{-1}$
Small friction α	$15 \pm 6 \times 10^2 \text{ Pa s m}^{-1}$
Contact length L	$24.7 \pm 0.5 \mu\text{m}$
Channel radius R	$4.4 \mu\text{m}$
Viscosity η_{2D}	$27 \pm 3 \times 10^{-4} \text{ Pa s m}$
Cell flow resistance ξ	$3.5 \pm 0.5 \times 10^{15} \text{ Pa s m}^{-3}$
Myosin scaling factor $\zeta^{(0)}$	$54 \pm 6 \text{ pN } \mu\text{m}^{-1}$

Table 3.1: Model parameters. Quantities obtained from the fitting procedure are highlighted in bold.

The particle image velocimetry analysis provided us with $k = 3$ datasets of the average cortical flow velocity \hat{v}_{ki} at points x_i along the cell, with $i = 1 \dots N_k$, where $N_k = 15, 14, 15$ for small, intermediate and large friction conditions respectively. Furthermore, we measured the average migration velocity \hat{U}_k of cells in the three different conditions. Using the microfluidic measurements of the friction coefficients α as functions of the cell flow resistance ξ , we fitted the remaining unknown parameters η , ξ and $\zeta^{(0)}$ to match the theoretical cortical flow field to the experimental data. To this end, we first projected the expression for the cortical velocity (Equations 3.18, 3.20 and 3.41) onto the x-axis using the transformations

$$\theta^{(r)} = \arccos \frac{R - x}{R} \quad (3.42)$$

$$x^{(m)} = x - R \quad (3.43)$$

$$\theta^{(f)} = \arccos \frac{x - R - L}{R}. \quad (3.44)$$

The fitting was then performed by minimizing the objective function

$$S(\eta, \xi, \zeta^{(0)}) = \sum_{\text{friction condition } k=1}^3 \left(\frac{1}{N_k} \sum_{i=1}^{N_k} \left(v_k(x_i; \eta, \xi, \zeta^{(0)}) - \hat{v}_{ki} \right)^2 + \left(U(\alpha_k; \eta, \xi, \zeta^{(0)}) - \hat{U}_k \right)^2 \right), \quad (3.45)$$

with the hat denoting measured data. The resulting estimates of η , ξ and $\zeta^{(0)}$ are given in Table 3.1. Assuming a thickness of the cortical layer of $h = 200 \text{ nm}$ ([26]), we calculate from the fitted value η the three-dimensional viscosity, obtaining $\eta_{3D} = \eta/h = 13.4 \pm 1.4 \text{ kPa.s}$. Furthermore, using Equation A.14, the fluid drag coefficient can be obtained from the fitted value of ξ ; we find $\alpha_D = 208 \pm 29 \text{ kPa.s/m}$. A summary of the physical quantities obtained from the fitting procedure is given in Table 3.2.

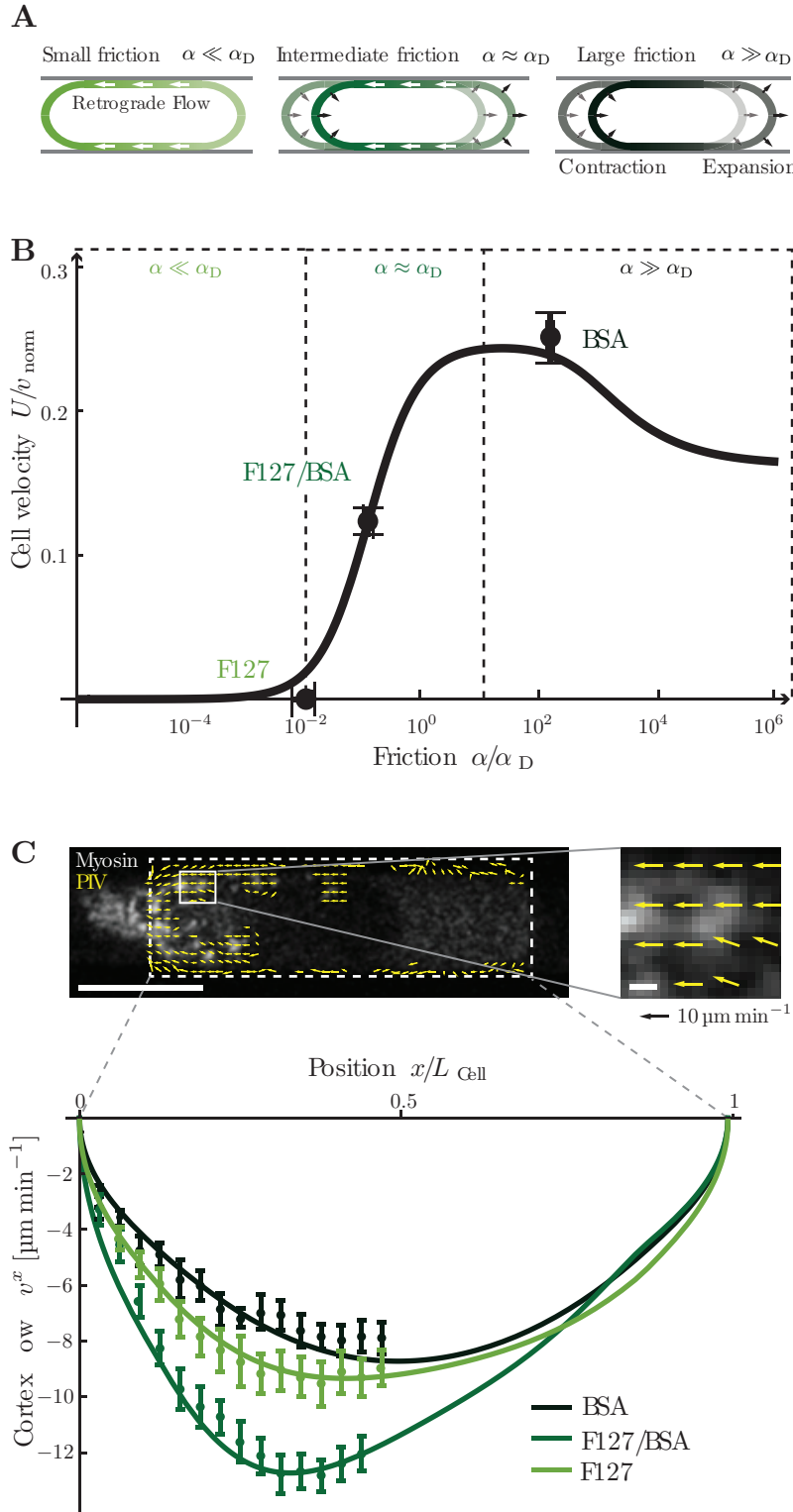


Figure 3.10:

The role of channel friction for cell migration mechanics.

A. Schematic representation of cell migration mechanics at different friction conditions relative to the fluid drag coefficient α_D . For $\alpha \ll \alpha_D$, the cortex fully slips along the channel walls and the cell does not translocate. For $\alpha \approx \alpha_D$, frictional effects resulting from cortex flows and deformations in the cell rear and front contribute to cell movement simultaneously. For $\alpha \gg \alpha_D$, the cells move by contracting the cell rear and expanding the front, with frictional forces keeping the cell body in place.

B. Cell migration velocity as a function of channel friction. Below a critical value of α set by the fluid drag coefficient α_D , frictional forces are not sufficient to push the cell against the fluid in the channel. $v_{\text{norm}} = (\zeta^{(r)} - \zeta^{(f)})L/\eta$.

C. Cortical flow velocities measured at different friction coefficients using particle image velocimetry (PIV), see Appendix C. Solid lines denote fitted curves of the theoretical description, calculated for measured profiles of myosin distribution along the cell. The fitting yields estimates for the parameters $\eta = 13.4 \pm 1.4 \text{ kPa s}$, $\alpha_D = 208 \pm 29 \text{ kPa s m}^{-1}$ and $(\zeta^{(r)} - \zeta^{(f)}) = 68 \pm 7 \text{ pN } \mu\text{m}^{-1}$. Scale bars: $10 \mu\text{m}$, and $0.5 \mu\text{m}$ for the zoom-in. Error bars denote the standard error of the mean. Similar figure published in [13].

Parameter	Estimate
Bulk viscosity η_{3D}	$13.4 \pm 1.4 \text{ kPa s}$
Active tension drop ($\zeta^{(r)} - \zeta^{(f)}$)	$68 \pm 7 \text{ pN } \mu\text{m}^{-1}$
Fluid drag coefficient α_D	$208 \pm 29 \text{ kPa s m}^{-1}$

Table 3.2: Mechanical parameters derived from fitted estimates.

Verification of fit results

Our final estimates of the cortex viscosity and the active tension drop obtained from the fitting procedures are in very good agreement with previously reported values. Bergert et al. measured the total surface tension of Walker cells using micropipette aspiration techniques in control cells and compared the values to cells treated with the myosin II inhibitor blebbistatin [12]. They measured $279 \pm 50 \text{ pN } \mu\text{m}^{-1}$ for the unperturbed condition and $65 \pm 20 \text{ pN } \mu\text{m}^{-1}$ for the blebbistatin condition. The difference in surface tension, which can be attributed to the active contribution from myosin motors is consistent with the difference in active tension between the myosin-depleted cell front and the highly contractile cell rear that we find in migrating blebbing Walker cells.

Although to our knowledge, no direct measurement of the viscosity of the actomyosin cortex has been performed in live cells to date, our estimate for the 3D viscosity of actomyosin obtain from the fitting procedure is in the range of values measured *in vitro* for reconstituted actin networks [98] and agrees with total-cell viscosities reported previously [91].

The cell flow resistance To assess the value of the cell flow resistance ξ yielded by the fit of the flow equations to the data, we investigated the flow of the medium induced by migrating cells in the microfluidic channel. From our calculations presented in Appendix A, we obtain the following relation between the flow resistance of a cell ξ and the average induced fluid flow of the external medium

$$\bar{v}_{\text{ext}} = \frac{\xi}{N\xi + \xi_{\text{ext}}} \sum_{i=1}^N U_i. \quad (3.46)$$

Quantifying the average number of cells per channel $N = 14 \pm 1$, and the average cell velocity $\bar{U} = 2.22 \pm 0.36 \text{ } \mu\text{m min}^{-1}$ in large friction conditions (see Figure 3.11), and using our estimate for ξ from the fitting procedure, we calculated that the cells induce an average fluid flow of $\bar{v}_{\text{ext}} = 1.4 \pm 0.2 \text{ } \mu\text{m min}^{-1}$ in the channel. To test this prediction and experimentally measure the average fluid flow, we injected microbeads into channels together with migrating cells and tracked their position over time in a bright field microscope (Figure 3.11 A - B). We proceeded to relate the average velocity of microbeads \bar{v}_{bead} to the average fluid flow velocity \bar{v}_{ext} in the following way. Assuming Hagen-Poiseuille flow in the channel, $v_{\text{ext}}(r)$ is related to the average fluid velocity \bar{v}_{ext} by

$$v_{\text{ext}}(r) = 2\bar{v}_{\text{ext}} \frac{R^2 - r^2}{R^2}. \quad (3.47)$$

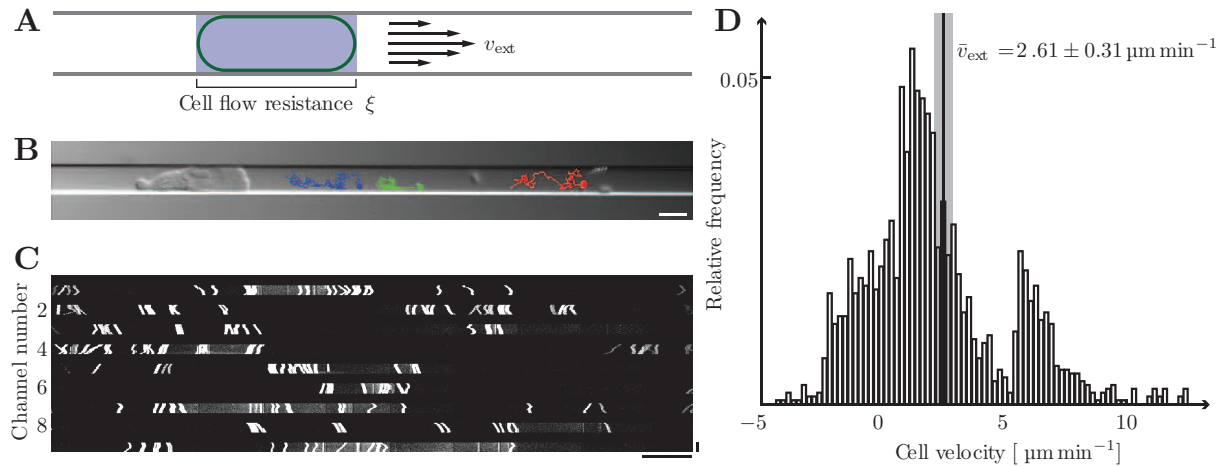


Figure 3.11: Fluid flow induced by migrating Walker cells in microfluidic channels.

A. Schematic representation of a migrating Walker cell in a microfluidic channel. The flow of the external medium is denoted by v_{ext} . The channel segment containing the cell offers a resistance to fluid flow characterized by ξ . Note that we do not distinguish between fluid passing through the cell itself or in between the cell surface and the channel walls. **B.** We measured the velocity of fluid flow induced by rapidly migrating Walker cells by quantifying the displacement over time of microbeads inserted in the channel (see Section 3.2.3 for details). The bead trajectories are highlighted in color. Scale bar: $10\ \mu\text{m}$. **C.** Kymograph of an ensemble of fluorescently labeled Walker cells migrating in a parallel system of 9 microfluidic channels treated with BSA. Scale bars: $100\ \mu\text{m}$ (horizontal), $30\ \text{min}$ (vertical). **D.** Histogram of cell velocities in BSA-coated channels obtained from kymographs of the full microfluidic channel array. To allow for comparison with fluid flow measurements in channels with rapidly migrating cells (see panel B), time-windows without cell velocities above $5.45\ \mu\text{m}\ \text{min}^{-1}$ were discarded. The threshold was chosen according to the 0.1 quantile of the velocity distribution of polarized, fast cells used for cortical flow analysis. Sample size: $N=164$ cells from 2 independent experiments. The average induced fluid flow \bar{v}_{ext} is shown on top. Panels B - D also published in [13].

Furthermore, the average velocity of the microbeads is related to the fluid flow $v_{\text{ext}}(r)$ by

$$\bar{v}_{\text{bead}} = 2\pi \int r dr p(r) v_{\text{ext}}(r), \quad (3.48)$$

where $p(r)$ is the radial distribution of bead positions. The distribution of bead positions obtained in the bright-field microscope is projected onto the y -axis. To estimate the radial distribution $p(r)$ from the projected distribution of bead positions $p(y)$, we used the inverse Abel transform [104]. From Equations 3.47-3.48, we then find $\hat{v}_{\text{ext}} = 2.61 \pm 0.31\ \mu\text{m}\ \text{min}^{-1}$, close to our prediction.

In summary, our theoretical description accurately accounts for cortical flows during blebbing Walker cell migration in microfluidic channels for all three friction conditions, relying on a single set of three fit parameters.

3.2.4 Force density on the cell surface

Using the parameter estimates obtained from fitting the cortical flow profiles as described in Section 3.2.3, we calculate the forces exerted by the cells on the channel walls during migration (see Figure 3.12). The two-dimensional force density on the surrounding walls is given by the product of the friction coefficient α and the relative velocity between the cortex and the wall at each point

$$f = \alpha(v^s + U). \quad (3.49)$$

We show the resulting spatial force pattern f in Figure 3.12. In a multipole expansion, the force monopole τ , the force dipole ρ and the force quadrupole γ characterize the first three terms. Taking the integrals over the contact surface between the cell and the channel, we obtain

$$\tau = 2\pi R \int_0^L dx \quad f, \quad (3.50)$$

$$\rho = 2\pi R \int_0^L dx \quad xf, \quad (3.51)$$

$$\gamma = 2\pi R \int_0^L dx \quad x^2 f, \quad (3.52)$$

where x refers to $x^{(m)}$, see Figure 3.6 A. At low Reynolds number, the total force transmitted by the cell to its environment is zero [106]. Thus, the force transmitted to the substrate by a crawling cell equals the drag force exerted on it by the surrounding fluid. The drag forces in a narrow channel are comparable to forces exerted by the cell on the substrate; therefore, the total force exerted by the cell on the channel does not vanish and gives rise to a non-zero force monopole τ (Table 3.3). We find that the next term in the multipole expansion, the force dipole ρ , is positive for all friction conditions (Table 3.3), indicating that a higher propulsive force is generated at the cell rear compared to the cell front. This observation is in sharp contrast with adhesive cell motility, where the force dipole has been measured to be negative (reviewed in [118]). Finally, we note that the quadrupole γ has a significant contribution to the force distribution for cells moving in large friction conditions. The ratio of quadrupole to dipole moments in this case yields a length much larger than the size of a single cell (average $\gamma/\rho \approx 100 \mu\text{m}$). Thus, flow and/or deformation fields induced by the cellular forces at large friction conditions are predominantly characterized by the quadrupole moment of the force distribution at distances below a few millimeters.

Multipole	Large friction	Intermediate friction	Low friction
Monopole τ	$-1.6 \times 10^{-12} \text{ N}$	$-1.0 \times 10^{-12} \text{ N}$	$-1.4 \times 10^{-13} \text{ N}$
Dipole ρ	$7.7 \times 10^{-17} \text{ N m}$	$2.5 \times 10^{-18} \text{ N m}$	$4.4 \times 10^{-20} \text{ N m}$
Quadrupole γ	$1.4 \times 10^{-20} \text{ N m}^2$	$-3.9 \times 10^{-23} \text{ N m}^2$	$-5.9 \times 10^{-24} \text{ N m}^2$

Table 3.3: Multipole moments of the force density exerted by migrating Walker cells on large, intermediate and small friction channels.

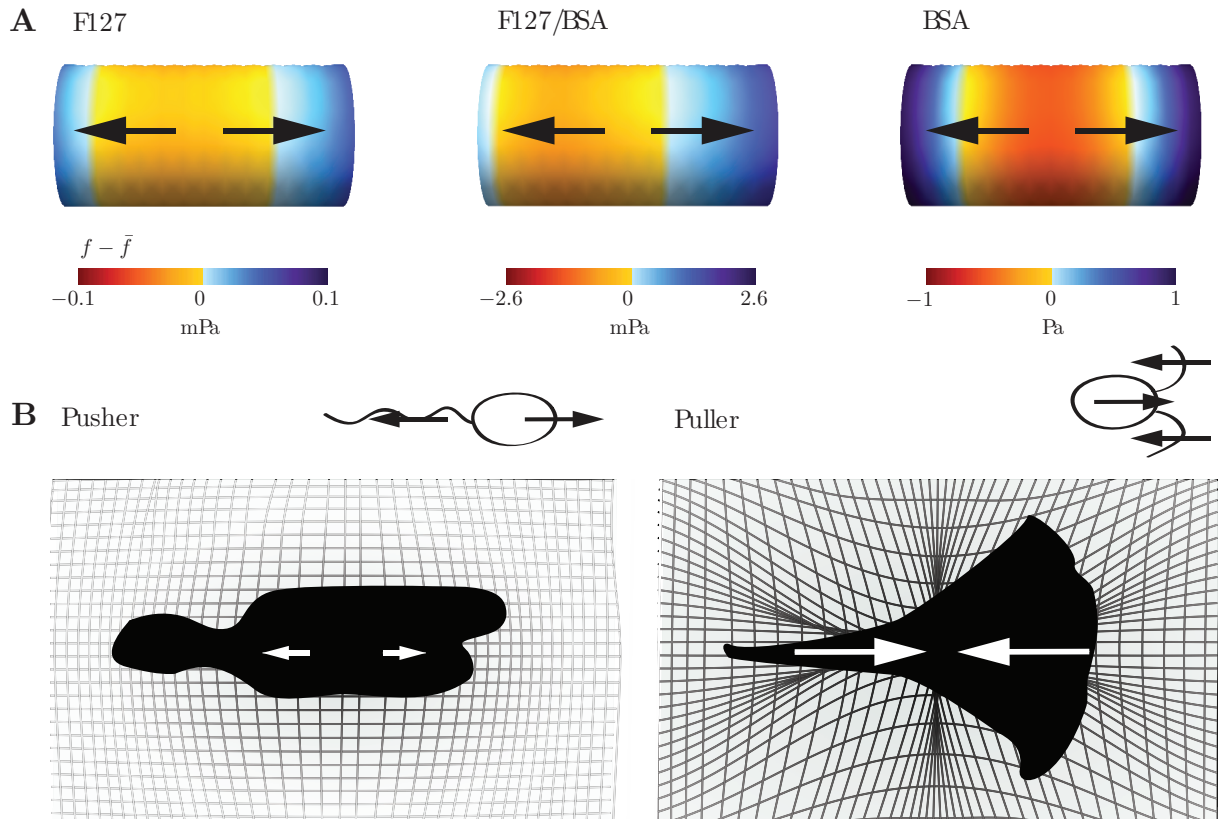


Figure 3.12: Forces exerted by migrating Walker cells.

A. Variation of the stress on the walls of the microfluidic channels during non-adhesive migration of Walker cells for different friction coefficients α . Total stress magnitudes are below 1 Pa for all friction conditions, see [13]. The forces involved in non-adhesive cell migration are thus several orders of magnitude smaller than for cells migrating with specific substrate adhesions (see e. g. Figure 3.1), and the distribution of the traction stress is characterized by a positive, expansile force dipole (indicated by arrows). **B.** Schematic representation of “pusher” and “puller” motility types, as distinguished by the sign of the force dipole. For swimming cells, several examples for each group are known, i. e. *Escherichia coli* bacteria (left panel) or *Chlamydomonas reinhardtii* algae (right panel). To our knowledge, non-adhesive Walker cells constitute the first example of a “pusher” type for crawling cells. All adhesive migration modes studied to date rely on pulling forces located in the cell front, giving rise to a negative force dipole. The force dipole characterizes the deformation field induced by a migrating cell in its environment. Similar figure published in [13].

3.3 Discussion

A variety of cell types including immune, embryonic and cancer cells, have recently been discovered to migrate without specific substrate adhesions [73, 111, 82], contrary to expectations based on the classical understanding of cell migration mechanics [3]. We aimed to uncover the physical principles underlying this migration mode and to quantify the forces transmitted during adhesion-independent cell movements. We show that non-adherent blebbing Walker cells move in microfluidic channels by establishing a gradient of myosin II-dependent active tension decreasing towards the cell front. Increased contractility at the cell rear drives cortical flows which generate sufficient propulsive force to move the cell body forward, if the friction between the cell surface and the channel wall exceeds the effect of fluid drag exerted by the medium surrounding the cell. Additionally, the cells perform deformations, which contribute to the cell velocity. Resulting from the myosin-dependent active tension gradient, the cells contract and expand in the rear and the front respectively. We identify three different regimes of cell migration behavior, for different values of the substrate friction, depending on the magnitude of the fluid drag coefficient (see Figure 3.10). For very small friction, cells cannot push themselves forward through the microfluidic channel, but remain in place with the cortex fully slipping along the channel walls. At intermediate friction conditions, cells achieve forward movement while still exhibiting slippage of the cortex, and at large channel friction, cells move effectively with the cortex fully coupled to the surrounding walls.

3.3.1 The fluid drag coefficient governs the threshold friction for adhesion-independent cell movement

We show that cell migration velocity depends strongly on the magnitude of the friction coefficient, characterizing the interactions between the cell cortex and the channel walls along the contact surface (see Figure 3.5). The threshold friction separating the moving and the non-moving regimes is governed by the fluid drag coefficient, which strongly depends on the geometry of the cell's environment (see Equation 3.37). Based on this relation, our theory makes a prediction regarding the conditions for non-adhesive cell movements in other confining geometries. Specifically, environments offering a smaller resistance to cell movement compared to the microfluidic channel arrangement should enable cells to move at smaller substrate friction coefficients. For example, the threshold friction is expected to be shifted to a smaller value for cells migrating between two flat surfaces, where the surrounding fluid medium can be displaced laterally as the cell moves forward, at a lower dissipative cost than for cells in narrow microfluidic channels. In fact, the experiments shown in Figure 3.2 B were performed on a glass plate coated with polyethylene glycol, a compound almost identical to F127, which was used in the low-friction experiments in microfluidic channels. Thus, a friction coefficient which is too small to enable cell movement in microfluidic channels, appears to be sufficient to drive cell movement between two plates, supporting the argument outlined above.

3.3.2 Possibilities regarding the origin of substrate friction in non-adhesive cell migration

The friction coefficient introduced in our theory of adhesion-independent cell migration (see Equation 3.4) describes the mesoscopic effect of both nonspecific molecular interactions between the cell surface and the channel walls, and possible mechanical effects. We discuss here the different possibilities for contributions to this quantity. Molecular interactions generating friction acting on the cell cortex may in principle involve any cortex-associated transmembrane proteins. Experiments on cells during cytokinesis [134] and cell polarization [40] for example have shown that microfabricated beads binding to surface receptors move at the outer surface of the plasma membrane in coupling with cortical flows. Importantly, molecular interactions giving rise to substrate friction in our system do not rely on the presence of a specific set of molecules as is the case for focal adhesion mediated couplings. In our experiments, cell migration behavior did not depend specifically on the molecule used to treat the channel walls. Cells exhibit identical behavior to the reported large friction experiments taken in BSA coated channels when migrating in channels functionalized with β -Lactoglobulin [13]. Even without applying any coating, the surface of the silicone rubber used for fabricating the channels (polydimethylsiloxane) provides sufficient friction to enable rapid cell migration (unpublished data from M. Bergert and I. Aspalter, 2015). Preliminary experiments interfering with different molecules present on the cell surface using degrading enzymes indicate that cell surface proteins may contribute to generating friction, while the polysaccharide groups present on many transmembrane proteins as well as lipids, known as the glycocalix, appear to be irrelevant for friction generation in Walker cells (unpublished data from M. Bergert and I. Aspalter, 2015).

In addition to molecular interactions, it should also be considered that a thin boundary layer of the fluid medium may be present in between the cell and the channel surface, and could potentially contribute to the arising friction. The movement of the cell surface relative to the channel wall would induce a steep velocity gradient within such a fluid layer, which, depending on the viscosity of the medium, may give rise to significant dissipation. While in the microfluidic channels used in our study, this effect obviously cannot account for the difference between the chemically obtained friction conditions, it may be relevant to explain friction in low-drag geometries.

The nonspecificity of the mechanisms involved in friction generation in non-adhesive cell migration has significant implications regarding the regulation of cell motility. While focal adhesions are actively assembled and spatiotemporally regulated by the cells, the nonspecific friction-based migration mechanism allows the cell to efficiently exploit an external source of dissipation, which automatically arises in confinement, simply by generating cortex flows resulting in a propulsive distribution of forces on the cell. Indeed, it has been proposed that adhesion-independent migration modes may be advantageous for cells moving through rapidly changing environments, such as immune and metastatic cells [108]. Furthermore, in strong confinement, where the contact area between the surrounding substrate and the cell surface is large, integrin-dependent adhesive motility may be disadvantaged and slowed by the large number of adhesion points [52, 6].

3.3.3 The role of forces and force dipoles for cell-cell interactions during collective cell migration

The stresses exerted by non-adherent Walker cells during migration in microfluidic channels are several orders of magnitude smaller than the traction stresses reported for adhesive cell migration, which range from hundreds to thousands of Pa [34, 94, 124], while the achieved migration velocities are similar. The large difference in the forces involved in non-adhesive cell movements compared to adhesive motility raises questions regarding the functional importance of large stresses sustained by focal adhesions. Rather than contributing to cell propulsion, strong adhesions may function to guide persistent motion and stabilize the shape of cells [6, 102, 100], for example, by anchoring actin filament bundles to integrin complexes at the cell periphery - functions which in fact lose relevance in cells moving in strong confinement where the local direction of migration and the shape of the cell is imposed by the surrounding environment. Furthermore, strong traction stresses during adhesive cell migration have been proposed to result in active substrate deformations, facilitating collective migration of groups of cells, for example inducing the alignment of collagen fibers in the direction of migration [117]. However, in environments such as narrow capillaries or dense extracellular matrix networks, a cell's ability to exploit and mold into pre-existing gaps and passages may be more advantageous than to maintain a rigid shape or to induce deformations [77].

The deformation field induced in an elastic medium by embedded motile cells depends on the force density distribution on the surface of the cells, in the same way as the velocity fields induced in a fluid medium by swimming microorganisms [76]. We find that the force density distribution on the surface of migrating Walker cells differs strongly from what has been observed in adhesive cells. Lamellipodial cells contract their substrate, exerting pulling forces in the front part, corresponding to a negative force dipole [118, 124], while non-adhesive Walker cells are characterized by a positive force dipole, with the cells generating more pushing forces in the rear (see Figure 3.12). While for swimming microorganisms, the classification according to “pusher” and “puller” strategies is common [76], to our knowledge, this work corresponds to the first description of a “pushing”-mechanism for crawling cells. Furthermore, for blebbing Walker cells, the quadrupole moment dominates over the dipole up to distances several times larger than the size of a cell (see Section 3.2.4). This effect is well known for so-called “squirmers”, swimming cells which move by inducing a retrograde flow at their surface. For example, the unicellular organism *Paramecium* uses a carpet of beating cilia [36] to accomplish this, and the physical principle is very similar to the propulsive effect of retrograde cortical flows in Walker cells.

To understand the interactions between collectively migrating cells in microfluidic channels, or more generally in any fluid-filled vessels, it will however likely be more important to consider the fraction of forces transmitted to the fluid, rather than to the surrounding walls. While for cells migrating on flat surfaces, the fraction of forces passed to the surrounding fluid is negligible, this is not the case for the strong confinement in narrow capillaries. The magnitude of this force corresponds to the value of the force monopole, listed in Table 3.3 for the Walker cells

under study. In fact, preliminary observations indicate that repolarization events leading to a switch of the direction of migration are correlated across blebbing Walker cells moving in the same channel (see Figure 3.11 C), suggesting that monopole-monopole interactions influence collective cell migration in microfluidic channels. Such effects may be relevant for understanding phenomena such as collective metastasis across blood and lymph systems [42].

List of symbols

i, j, \dots	Indices of the coordinates on the surface
α, β, \dots	Indices of cartesian coordinates x, y, z
(r), (m), (f)	Superscripts denoting the rear, middle and front parts of the cell
t	Time
s	Arclength surface coordinate
ϕ	Angle surface coordinate
$\theta^{(r)}, x^{(m)}, \theta^{(f)}$	Coordinates used for the rear, middle and front cell parts
∇_i	Covariant derivative operator
$\mathcal{P}_\nu^1, \mathcal{Q}_\nu^1$	Associated Legendre polynomials
X	Axisymmetric surface representing the cell cortex
$\mathbf{e}_x, \mathbf{e}_y, \mathbf{e}_z$	Cartesian basis vectors
r	Shape of the axisymmetric surface
$\mathbf{e}_s, \mathbf{e}_\phi$	Tangent basis vectors of the surface
n	Normal vector of the surface
ψ	Surface angle
g_{ij}	Metric tensor
C_{ij}	Curvature tensor
Γ_{ij}^k	Christoffel symbols of the second kind
t_{ij}	Tension tensor
$\Sigma_{\text{int}}, \Sigma_{\text{ext}}$	Intracellular and extracellular shear stresses acting on the cortex
$P_{\text{int}}, P_{\text{ext}}$	Intracellular and extracellular pressures acting on the cortex
v^s	Velocity of flow within the surface
v^n	Velocity normal to the surface
v_{ij}	Symmetric velocity gradient tensor
η	Viscosity parameter

ζ	Active tension
α	Friction coefficient
U	Cell velocity
R	Radius of microfluidic channel
L	Length of contact area between cell and channel
α_D	Fluid drag coefficient
η_{ext}	Viscosity of extracellular medium
I	Relative myosin fluorescence intensity
$\zeta^{(0)}$	Proportionality constant between myosin intensity and active tension
l	Hydrodynamic length, $l = \sqrt{\eta/\alpha}$
C_1, C_2	Integration constants
$\delta r, \delta \psi, \delta v^s, \delta P$	Deviations from the spherical reference solution
\bar{t}	Average cellular surface tension
$v^{(r)}, v^{(f)}$	Velocity at the contact points between the cylindrical and pole cell regions in the rear and front
a	Numerical coefficient
U_0	Intrinsic cell velocity, i. e. cell velocity in the absence of external dissipation
χ	Effective cell friction
\bar{v}_{ext}	Average flow velocity of the extracellular medium
\bar{v}_{bead}	Average velocity of microbeads
$\bar{v}_{\text{ext,free}}$	Average flow velocity of the extracellular medium in the absence of cells
P_{applied}	Pressure difference applied to the inlet and outlet of the microfluidic channel: $P_{\text{applied}} = P_{\text{in}} - P_{\text{out}}$
ξ	Hydraulic resistance of a channel segment containing a cell
ξ_{ext}	Hydraulic resistance of the microfluidic channel
L_{ext}	Length of the microfluidic channel
S	Objective function
h	Height of the cortical layer
N	Number of cells
p	Distribution of bead positions
f	Force density
τ	Force monopole
ρ	Force dipole
γ	Force quadrupole

Chapter 4

Furrow initiation in pseudocleavage and cytokinesis

When cells divide, their cytoplasm is cleaved into two parts to form the daughter cells. This process, driven by a contractile actomyosin band [3], is known as cytokinesis. The correct execution of cell cleavage is crucial in determining the fate of the daughter cells. Correspondingly, cytokinesis underlies heavy spatiotemporal regulation in the cell, with biochemical signaling and mechanical effects interacting to achieve a robust and precise machinery. Here we take advantage of a particular cell biological model system, in which a non-cytokinetic contractile ring forms in the absence of cytokinetic biochemical regulation, thus enabling the study of mechanical feedbacks in the actomyosin cortex, which result in the initiation of a cleavage furrow independent of signaling effects. After a brief introduction to the general background of the problem and our experimental system, we present a theoretical description of furrow initiation expanding on the framework introduced in previous chapters. Specifically, we investigate the effect of anisotropies in the cortical tension arising from the alignment of actin filaments along the contractile ring. We compare the predictions from this description to experimental data obtained during the initial phases of furrowing, and conclude with a brief discussion.

4.1 Contractile rings and the initiation of cytokinesis

Contractile rings of actomyosin are formed during constriction processes at both the tissue and cell level, such as during wound healing, or the cleavage of daughter cells in cell division [8]. The rings formed during the healing of ruptures in epithelial sheets, or when apoptotic cells are extruded span several cells, while the closure of plasma membrane lesions and the ingression of the cell division furrow involve single cell structures (see Figure 4.1, [8, 27]). Contractile rings are ancient; specifically the cytokinetic actomyosin ring is evolutionarily conserved across animal cells, fungi as well as slime molds [8]. The contractile ring appearing at the initiation of cytokinesis, the final step of the cell cycle, is assembled from aligned actin filaments, myosin II motors and associated regulatory and structural proteins [3]. The thickness and width of the cytokinetic ring ranges from $0.1\ \mu\text{m}$ to $0.2\ \mu\text{m}$ and $1\ \mu\text{m}$ to $20\ \mu\text{m}$ respectively, depending

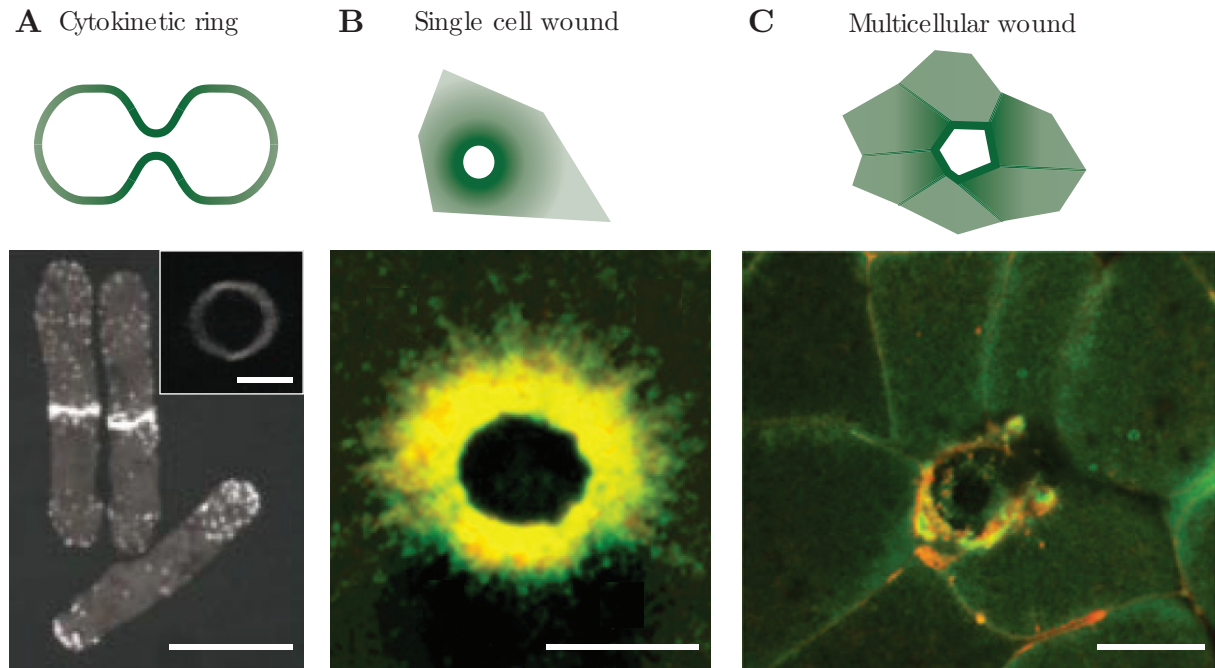


Figure 4.1: Actomyosin contractile rings in single cells and tissues.

A. Dividing cells of the fission yeast *Schizosaccharomyces pombe* stained for filamentous actin with the fluorophor AlexaFluor 488 phalloidin. Scale bar: 5 μm . Inset: Top view of the contractile ring marked with GFP-cdc4. Scale bar: 2.5 μm . Images taken from [101]. **B.** Cortical ring formed during single cell wound healing in a fixed cell of the *Xenopus laevis* embryo, stained for actin (red, Alexa 568 phalloidin) and active myosin II (green, α -p-RMLC). Scale bar: 50 μm . Image taken from [27]. **C.** Multicellular contractile ring during wound healing of *Xenopus laevis* embryonic tissue. Actin filaments, labeled in red (mCherry-UtrCH) accumulate at the cell edges around the wound. Scale bar: 50 μm . Image taken from [27].

on the cell type [49]. The assembly of the cytokinetic ring is heavily regulated, and involves the local activation of myosin II, minifilament formation as well as the polymerization of new, unbranched actin filaments [3], which control the local actin architecture within the ring. The spatiotemporal control of furrow initiation appears to depend on the microtubules involved in the formation of the cell division spindle (see Section 1.1.1). In large marine invertebrate egg cells, it has been shown that a displacement of the cleavage furrow is achieved by displacing the spindle [107]. In addition to biochemical regulatory processes, mechanical effects may contribute to the formation of the cleavage furrow. During cytokinesis, the cell cortex exhibits long-ranged flows, which have been proposed to influence the architecture of the actin network, inducing the preferential alignment of filaments along the cell equator, where the contractile ring is formed [18]. Local alignment of actin filaments in turn may induce anisotropies in motor-mediated active stresses by introducing a preferred direction for motor-filament interactions [113]. In metazoan cells, two phases of contractile ring formation are distinguished, the furrow initiation, where a broad contractile band is formed, and the subsequent transformation of the broad band into a thin ring at the tip of the furrow. Our work focuses on the first phase, the initiation of the cleavage furrow. Specifically, we study the interplay between cortical flows, actin filament alignment and active stresses involved in the formation of the cleavage furrow and ring assembly.

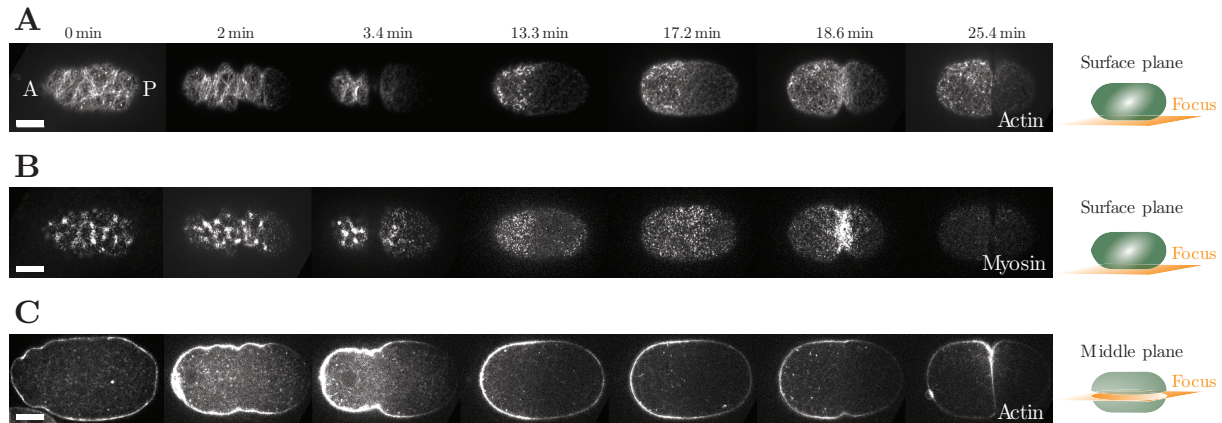


Figure 4.2: Dynamics of the actomyosin cortex during pseudocleavage and cytokinesis in the *C. elegans* embryo.

A. - C. One-cell embryo of *C. elegans* with fluorescently labeled actin filaments (Life-Act::mKate2, panel A and C) and myosin II (NMY-2::GFP, panel B), undergoing pseudocleavage and cytokinesis. The anterior side of the embryo (A) is to the left, posterior to the right (P). The filaments align perpendicular to the antero-posterior cell axis during furrow initiation at 2 min and 18.6 min. Scale bars: 10 μm . Microscopy images obtained by A.-C. Reymann.

4.2 Furrow initiation in the *C. elegans* zygote

The nematode *Caenorhabditis elegans* provides good experimental access to the cytoskeleton during the initial stages of embryonic development [50, 28]. Adult *C. elegans* hermaphrodites are able to self-inseminate, thereby producing fertilized eggs which later develop into larvae. We take advantage of a particular phenomenon in *C. elegans* zygotes, where the actomyosin cortex undergoes a particular sequence of reorganizations over the time interval from fertilization to the first cell division, involving the subsequent formation of *two* contractile rings [4, 56]. After sperm entry at fertilization, a rigid egg shell is formed around the embryo, which takes on a prolate ellipsoid shape (see Figure 4.4 A). The position of the male pronucleus defines the posterior pole of the embryo. After the initial symmetry breaking event, the cell polarizes along the antero-posterior cell axis, establishing two cortical domains with different properties [28]. The polarization process involves long-ranged cortical flows directed towards the anterior side, involved in the segregation of polarity cues [86]. During this phase, the first contractile ring appears. It is termed the pseudocleavage furrow because it generates a constriction, which does not fully cleave the cell (see Figure 4.2, [120, 4, 56]). It is not known whether the pseudocleavage furrow serves a particular biological function [130]. Approximately 15 min later, the initiation of cytokinesis starts with the spatially and temporally regulated recruitment of actin, myosin and numerous regulating proteins to the location of the cleavage plane, where a fully constricting ring forms. It has been proposed that myosin II activity at the location of furrow formation drives cortical flows, which reorient the actin filaments into an ordered ring, such that both the direct myosin-dependent stress and the stress-alignment coupling act together to form the cell ingression [113]. However, in contrast to the cytokinetic ring, the pseudocleavage plane is not characterized by a spatially regulated increase in myosin II activity [130]. On the contrary, during this developmental stage, the myosin distribution decreases along the length of the cell, giving

rise to the polarizing cortical flows [86]. Figure 4.2 B and Figure 4.3 C - D show the distribution of cortical myosin along the antero-posterior cell axis. Both phases however are characterized by similar patterns of actin filament alignment, with a distinct peak near the mid-position (see Figure 4.2 A and Figure 4.3 C - D). By comparing the cortical dynamics and cell shape changes during the two furrowing phases, we hope to understand how stress-alignment coupling, i. e. the influence of the local actin architecture on the active cortical stress, contributes to the formation of a cell ingression.

4.2.1 Theoretical description of furrow initiation

Both during pseudocleavage and cytokinesis, the shape ingressions are driven by the behavior of the actomyosin cortex in the zygote. Following a similar approach to the preceding chapters, we represent the actomyosin cortex as an active, viscous material, and describe how the combination of isotropic and anisotropic cortical tensions, resulting from the interplay of motor activity and actin alignment, induces furrow initiation. We use experimental data for the distribution of myosin II along the antero-posterior axis, the magnitude of cortex flows, and the level of actin filament alignment (Figure 4.3), which were obtained from quantitative live imaging with fluorescent markers of actin and myosin¹. With these measurements, we calculate the cell shapes during pseudocleavage and cytokinesis, and compare our predictions to the measured level of ingression.

Nematic ordering of actin filaments

We describe the local alignment of actin filaments by a nematic order parameter, defined as in liquid crystal theory [32]

$$Q^i_j = \langle n^i n_j - \frac{1}{2} \delta^i_j \rangle, \quad (4.1)$$

with n_i the nematic director field defined to have unit length, such that the nematic tensor is traceless by construction². We assume the following free energy density for filament interactions

$$f_n = \frac{\chi}{2} Q^i_j Q^i_j + \frac{\iota}{2} \partial_k Q^i_j \partial_k Q^i_j, \quad (4.2)$$

where χ is the inverse nematic susceptibility, characterizing the resistance of the nematic to isotropy, and the second term is the distortion energy according to the one-constant approximation of Franks free energy for nematic liquid crystals. This free energy describes a nematic liquid crystal in the isotropic state. The generalized conjugate force to the nematic director is the molecular field h_i given by (see Section 1.2.2)

$$h_i = -\frac{\delta F_n}{\delta Q^i_j} = -\chi Q^i_j + \iota \partial_k^2 Q^i_j, \quad (4.3)$$

¹A.-C. Reymann (BIOTEC, TU Dresden) obtained and analyzed all experimental data presented in this chapter.

²The nematic theory for the actomyosin cortex used here was developed by F. Staniscia and G. Salbreux (MPI-PKS, Dresden), for details see [113, 16, 109]

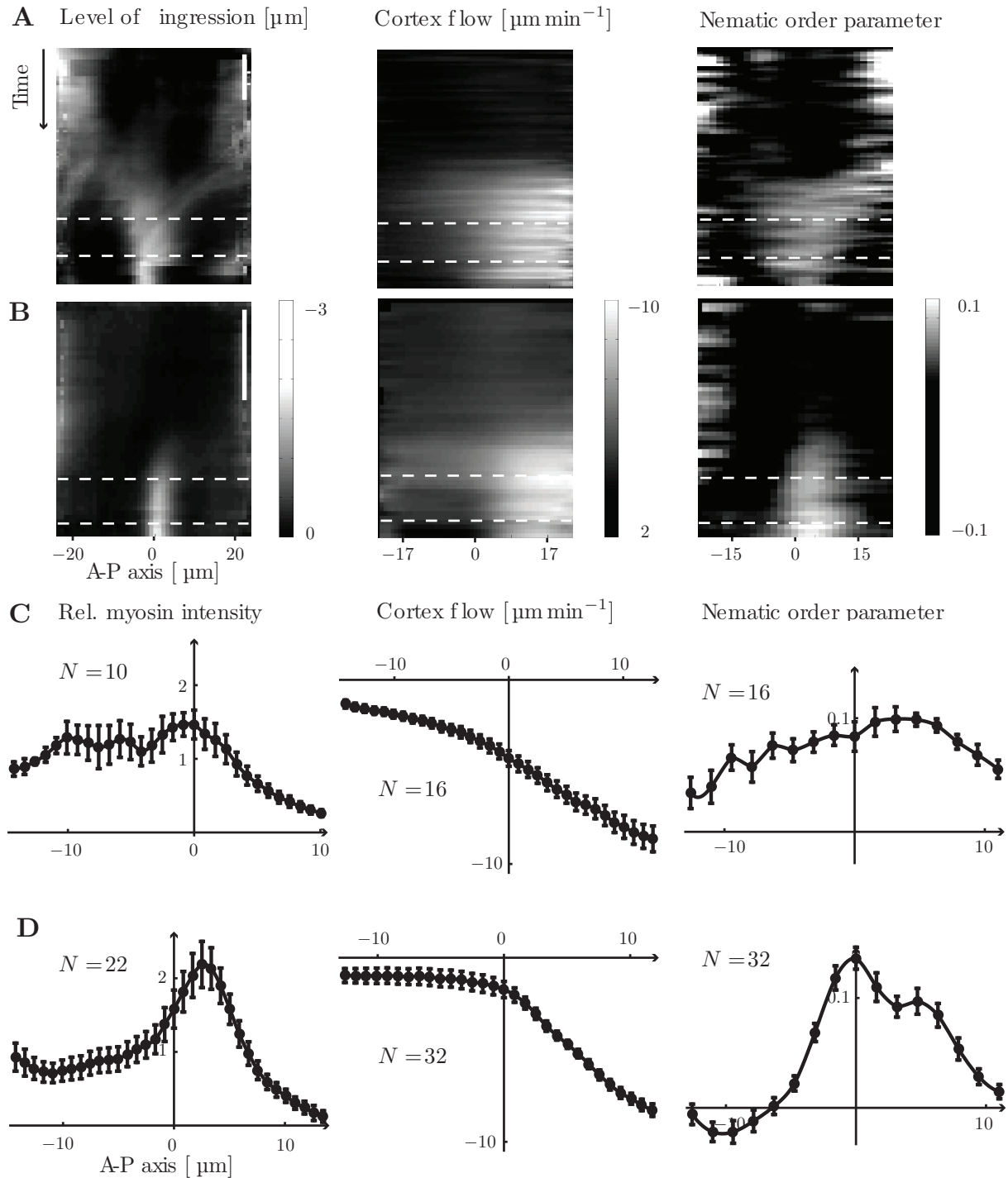


Figure 4.3: Myosin distribution, flow velocities and actin ordering in the cortex.

A. - B. Kymographs of the level of ingression (left), the magnitude of cortex flows (middle) and the nematic order parameter (right) along the antero-posterior cell axis, during pseudocleavage formation (panels A, averaged over $N = 10$ embryos) and cytokinesis initiation (panels B, averaged over $N = 12$ embryos). The stationary phase is marked by dashed lines. Scale bars: 100 min. Kymographs created by A.-C. Reymann. **C. - D.** Profiles of the relative intensity of myosin II motors, the cortical flow and the nematic order parameter along the antero-posterior cell axis, during pseudocleavage (panels C) and cytokinesis (panels D). The profiles are obtained as averages over several embryos with N denoting the number of embryos in each panel, and averages over the stationary time interval as marked in the kymographs. While actin filament alignment shows a peak near the cell equator in both furrowing phases, the distribution of myosin is peaked in cytokinesis only, and decreases along the antero-posterior cell axis during pseudocleavage. The flow profiles were obtained using particle image velocimetry, and the nematic order parameter was quantified using a Fourier-transform based method, see [109] for details. Data measured and analyzed by A.-C. Reymann. Error bars denote the standard error of the mean.

where F_n is the nematic free energy. Thus, the free energy is minimized in the isotropic state, where $Q^i_j = 0$, implying that actin filament interactions do not result in spontaneous alignment and any ordering arises as a consequence of cortical flows. We assume the following constitutive relation for Q^i_j

$$\partial_t Q^i_j + v_k \partial_k Q^i_j = -\frac{1}{\tau} Q^i_j + \frac{l^2}{\tau} \partial_k^2 Q^i_j + \beta \left(v^i_j - \frac{v^k_k}{2} \delta^i_j \right), \quad (4.4)$$

where the left hand side is the convected derivative of Q^i_j , and β characterizes the flow-alignment coupling. Here we have introduced the characteristic time- and length scales τ and l , which are related to the coefficients in Equation 4.3 by $\tau \propto 1/\chi$ and $l = \sqrt{\iota/\chi}$. In [109], Equation 4.4 is used to explain the pattern of nematic ordering in the cortex as a result of long-ranged cortical flows during pseudocleavage and cytokinesis. Here, we focus on the effect of actin filament alignment on the cortical tension and the shape of the cell.

Main equations

Taking into account the coupling between the local orientation of actin filaments and the active tension generated by myosin motor activity, we add a term to the constitutive relation for the tension tensor in the cortex as introduced in Section 2.3 (see also [105])

$$t^i_j = \eta_s \left(v^i_j - \frac{1}{2} v^k_k \delta^i_j \right) + \eta_b v^k_k \delta^i_j + \zeta \delta^i_j + \xi Q^i_j. \quad (4.5)$$

As before, v^i_j is the velocity gradient tensor. The coupling coefficients ζ and ξ represent the effect of active motors in the cortical layer. In section 4.2.1 we relate these coefficients to the measured distribution of active motors in the cortex.

The *C. elegans* zygote is surrounded by a confining rigid egg shell (see Figure 4.4 A), such that two contact points between the cortex and the egg shell appear, when the embryo forms an ingression during pseudocleavage and cytokinesis. While outside of the ingression zone, the cell is constrained by the egg shell, the shape taken between the contact points is determined by actomyosin-intrinsic forces and the pressures in the surrounding fluids (see Figure 4.4 B). Considering the balance of forces in the direction normal to the cell surface in this region thus allows to calculate the level of ingression.

Using the parameterization of the cortical surface introduced in Chapter 2, we combine the force balance Equations 2.26 - 2.27 with the modified constitutive material Equation 4.5 to recover the equations governing the flow v^s in the cortical layer, and the shape r of the cell. Both ingression processes feature a stationary phase, during which the cortical profiles of flow and actin alignment, as well as the cell shape remain approximately unchanging (see Figure 4.3 A - B). We aim to describe the level of ingression during these stationary phases and therefore seek steady state solutions of the shape such that the velocity normal to the cortical surface vanishes

$v^n = 0$. The cortex equations derived as in Chapter 2 then read

$$0 = \partial_s(\xi Q^s_s) + \partial_s \zeta + \left(\eta_b + \frac{1}{2}\eta_s\right) \partial_s^2 v^s - \frac{\sin \psi}{r} \left(\eta_b - \frac{1}{2}\eta_s\right) v^s \partial_s \psi + \frac{\cos \psi}{r} \left(\xi(Q^s_s - Q^\phi_\phi) + \left(\eta_b + \frac{1}{2}\eta_s\right) \left(\partial_s v^s - \frac{v^s \cos \psi}{r}\right)\right), \quad (4.6)$$

and

$$P_{\text{int}} - P_{\text{ext}} = \partial_s \psi \left(\xi Q^s_s + \zeta + \left(\eta_b + \frac{1}{2}\eta_s\right) \partial_s v^s\right) + \frac{\sin \psi}{r} \left(\xi Q^\phi_\phi + \zeta + \left(\eta_b + \frac{1}{2}\eta_s\right) \frac{v^s \cos \psi}{r}\right) + \left(\eta_b - \frac{1}{2}\eta_s\right) \left(\frac{\sin \psi}{r} \partial_s v^s + \frac{\cos \psi}{r} \partial_s \psi v^s\right), \quad (4.7)$$

where we have neglected any external shear stresses. The second equation relates the shape of the cell to the profiles of the cortex velocity, the nematic order parameter, and the myosin-dependent active tension and alignment-coupling.

The linearized shape equation

Active isotropic and anisotropic stresses in the cortex result from motor forces. We assume that the spatial profiles of ζ and ξ scale with the density of myosin II molecules in the cortical layer. Using fluorescence microscopy to estimate the distribution of active myosin II along the embryo, we write linear relationships introducing the coupling coefficients $\zeta^{(0)}$ and $\xi^{(0)}$

$$\zeta(s) = \zeta^{(0)} \frac{I(s)}{\bar{I}}, \quad (4.8)$$

$$\xi(s) = \xi^{(0)} \frac{I(s)}{\bar{I}}, \quad (4.9)$$

where $I(s)$ is the relative fluorescence intensity of cortical myosin motors.

We now consider a reference state, where the distribution of motors in the cortex is uniform such that ζ and ξ are constant in s , and assume that the deviation from this reference state is small, i. e.

$$\zeta = \zeta^{(0)} + \delta\zeta \quad (4.10)$$

$$\xi = \xi^{(0)} + \delta\xi, \quad (4.11)$$

with $\delta\zeta = \zeta^{(0)}(I(s) - \bar{I})/\bar{I}$ and $\delta\xi = \xi^{(0)}(I(s) - \bar{I})/\bar{I}$. In the reference state, the cell does not form an ingression, the flow in the cortex is zero and the actin network is isotropic: Eq.'s 4.4 and 4.6 - 4.7 are solved by $r = R$, $\psi = \pi/2$, $v^s = 0$, $Q^i_j = 0$, $P_{\text{int}} - P_{\text{ext}} = \zeta^{(0)}/R$, where we denote the radius of the egg shell by R and assume that it is constant in s (see Figure 4.4 B). Performing a linear expansion around this state ($r = R + \delta r$, $\psi = \pi/2 - \partial\delta r/\partial s$, $v^s = \delta v^s$, $Q^i_j = \delta Q^i_j$, $P_{\text{int}} - P_{\text{ext}} = \zeta^{(0)}/R + \delta P$), we obtain the linearized shape equation (see Eq. 4.7)

for the level of ingression δr

$$0 = \frac{\delta\zeta + \xi^{(0)}\delta Q^\phi_\phi - R\delta P}{\zeta^{(0)}} + \frac{2\eta_b - \eta_s}{2\zeta^{(0)}}\partial_s\delta v^s - \frac{1}{R}\delta r - R\frac{\partial^2\delta r}{\partial s^2}, \quad (4.12)$$

The solution to this equation describes the deviation of the cell radius from the egg shell when the zygote forms an ingression at the onset of pseudocleavage and cytokinesis, in response to the isotropic and anisotropic tensions arising from spatial heterogeneities in the distribution of active motors.

The level of ingression

Solving Eq. 4.12, we obtain the level of ingression δr as a function of the geometric and mechanical properties of the cell, and the profiles of cortical flow, myosin distribution and nematic ordering

$$\begin{aligned} \delta r = & \cos\left(\frac{s}{R}\right)C_1 + \sin\left(\frac{s}{R}\right)C_2 - R\left(\frac{R\delta P}{\zeta^{(0)}} + 1\right) + \frac{2\eta_b - \eta_s}{2R\zeta^{(0)}}\int_{s_0}^s ds' \left[\cos\left(\frac{s-s'}{R}\right)\delta v^s(s')\right] \\ & + \frac{\xi^{(0)}}{\zeta^{(0)}}\int_{s_0}^s ds' \left[\sin\left(\frac{s-s'}{R}\right)\delta Q^\phi_\phi(s')\right] + \int_{s_0}^s ds' \left[\sin\left(\frac{s-s'}{R}\right)\frac{I(s')}{\bar{I}}\right], \end{aligned} \quad (4.13)$$

where C_1 and C_2 denote constants of integration. Given a set of boundary conditions, we can thus express the shape of the zygote as a function of its mechanical and geometric parameters, and the profiles of cortical flow and nematic order parameter. At the points s_1 and s_2 , the cortex of the embryo is touching the egg shell: the shape in these points is given by R , and has to be smoothly connected to the contact regions. Thus, δr has to fulfill the following four conditions

$$\delta r(s = s_1) = 0, \quad \left.\frac{\partial\delta r}{\partial s}\right|_{s=s_1} = 0, \quad \delta r(s = s_2) = 0, \quad \left.\frac{\partial\delta r}{\partial s}\right|_{s=s_2} = 0. \quad (4.14)$$

We determine the position of s_1 and s_2 from experimental measurements (see [109]). Grouping the unknown parameters into

$$p_1 = \frac{R\delta P}{\zeta^{(0)}}, \quad p_2 = \frac{2\eta_b - \eta_s}{2R\zeta^{(0)}}, \quad p_3 = \frac{\xi^{(0)}}{\zeta^{(0)}}, \quad (4.15)$$

we use Eq.'s 4.14 to determine the integration constants C_1 and C_2 as well as the dimensionless pressure parameter p_1 and the viscosity parameter p_2 . Finally, we estimate the profiles of Q^ϕ_ϕ and the cortex flow v^s by interpolating the experimentally measured values along the embryo (Figure 4.3), and fit the shape solution Eq. 4.13 to the data for the level of ingression during pseudocleavage and cytokinesis. Specifically, we estimate the single remaining unknown parameter p_3 by minimizing the difference between the experimental data points and the theoretical curve using the objective function

$$S(p_3) = \frac{1}{N_{\text{pc}}} \sum_{i=1}^{N_{\text{pc}}} (\delta\hat{r}_{i,\text{pc}} - \delta r_{\text{pc}}(x_i; p_3))^2 + \frac{1}{N_{\text{ck}}} \sum_{i=1}^{N_{\text{ck}}} (\delta\hat{r}_{i,\text{ck}} - \delta r_{\text{ck}}(x_i; p_3))^2, \quad (4.16)$$

where pc and ck are short for pseudocleavage and cytokinesis respectively, and the hat denotes measured data. The parameter estimates are summarized in Table 4.1. Fitting a single parameter to the experimental data from both developmental phases achieves a close correspondence between the theoretical description and the measurements (see Figure 4.4 C). We find that the cortex deformations observed during furrow initiation are best matched with a myosin coupling ratio $\xi^{(0)}/\zeta^{(0)} = 21 \pm 5$. Multiplying this ratio with the maximum order parameter along the embryo, gives an estimate for the relative influence of anisotropic versus isotropic myosin-dependent stresses in driving the ingression. We find 2 for pseudocleavage, and 3 for cytokinesis. Thus, the anisotropic stress resulting from nematic ordering of actin filaments plays an important role in furrow initiation in pseudocleavage and cytokinesis.

4.3 Discussion

4.3.1 The pseudocleavage furrow arises from the processes polarizing the cell

Discovered more than 30 years ago [120, 4], it has yet remained unanswered, why a pseudocleavage forms in *C. elegans* embryos and whether it is itself associated with any functionally relevant mechanism for the cell. Here we have shown that the phenomenon can be explained as a consequence of the cortical processes undergone by the polarizing cell. The density of myosin motors decreases from the anterior towards the posterior end of the cell (see Figure 4.2 B and 4.3 C), and drives a sustained flow of cortical material, which distributes cell-fate determinants across the two halves of the embryo to establish the first asymmetric cell division. The compression of material due to the gradient in the cortical flow (see Figure 4.3 C - D) aligns the actin filaments, resulting in the observed peak of filament ordering, as is detailed in [109]. The arising anisotropy in the active contractile tension then leads to the ingression of the cell cortex. Thus, simply the requirement for polarizing cortical flows together with the couplings present in the actin cortex, which connect velocity gradients, filament alignment and tension (see Equations 4.4 - 4.5), is sufficient to explain the phenomenon of pseudocleavage in *C. elegans* embryos.

4.3.2 Robustness of the pseudocleavage and cytokinetic furrows

We identify a general mechanism underlying the furrow ingression during pseudocleavage and cytokinesis, which is based on the flow-induced alignment of actin filaments and resulting anisotropies in the cortical stress leading to the observed cell shape changes. This effect may be expected to arise and play a role in many other systems, where the cortex displays velocity gradients. It remains to be investigated how the required couplings depend on properties of the actin network, such as the level of cross-linking, which may vary between different cells. Additional experiments interfering with actin architecture using RNA interference of actin associated proteins (for details, see [109]) suggest that flow-alignment coupling in the *C. elegans* cortex is quite robust with respect to changes in local properties of the cortex, such as the amount of bundling, and the presence of myosin foci. It appears however, that during the pseudocleavage phase, the characteristic peak of alignment arises only for a limited range of velocity gradients;

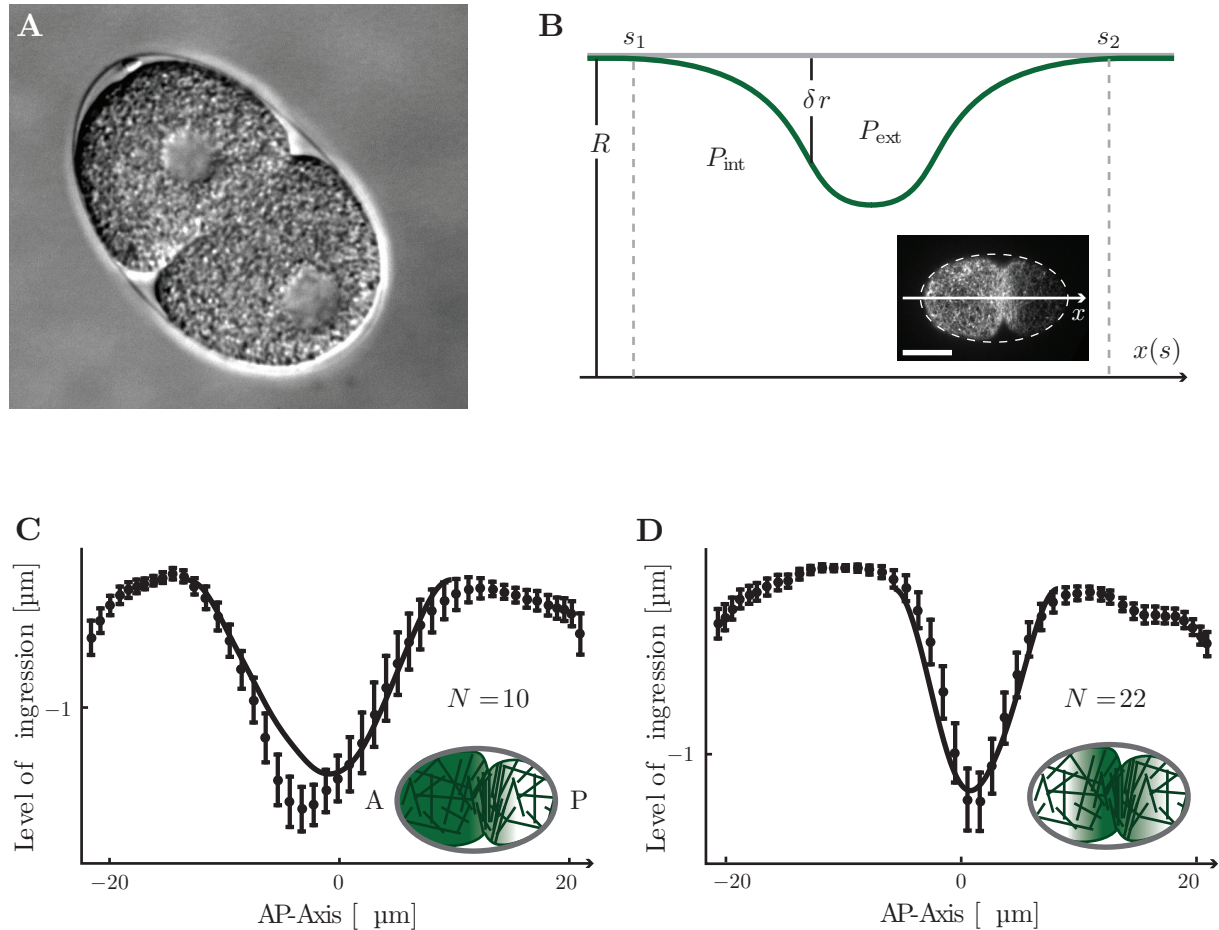


Figure 4.4: Theoretical description of furrow initiation in the *C. elegans* zygote. **A.** Bright field microscopy image of the cell during pseudocleavage. The embryo is confined by an egg shell outside of the ingression zone. **B.** Schematic representation of the cortical surface in the ingression zone. The egg shell is assumed to have a constant radius R in the ingression zone. The contact points with the cortex are denoted s_1 and s_2 . Inset: LifeAct::mKate fluorescence microscopy image of the *C. elegans* cortex during cytokinesis (also shown in Figure 4.2). Scale bar: $10 \mu\text{m}$. **D-E** Comparison between measured data for the level of ingression in pseudocleavage (panel **C**.) and cytokinesis (panel **D**.) and the fitted theoretical curve (solid lines). The fitting yields the parameter estimate $\xi^{(0)}/\zeta^{(0)} = 21 \pm 5$. The number of embryos is denoted by N ; error bars represent the standard error of the mean. Microscopy images and shape data acquired by A.-C. Reymann.

Parameter	Estimate pseudocleavage	Estimate cytokinesis
Egg-shell radius R	$14.0 \pm 0.1 \mu\text{m}$	
Pressure parameter $p_1 = \frac{R\delta P}{\zeta^{(0)}}$	1.4 ± 0.4	1.8 ± 0.5
Viscosity parameter $p_2 = \frac{2\eta_b - \eta_s}{2R\zeta^{(0)}}$	$0.07 \pm 0.07 \text{ min } \mu\text{m}^{-1}$	$0.08 \pm 0.03 \text{ min } \mu\text{m}^{-1}$
Nematic-to-myosin ratio $p_3 = \frac{\xi^{(0)}}{\zeta^{(0)}}$	21 ± 5	

Table 4.1: Parameters in the theoretical description.

a reduction of cortical flows achieved by perturbing myosin activity patterns has a strong effect on actin ordering and ingression levels, indicating that compression has to exceed some level to induce filament ordering. In contrast, the actin alignment peak as well as furrow formation in cytokinesis persist under these perturbations [109]. Additional regulatory mechanisms may be in place to ensure the successful formation of the cytokinetic furrow, which determines the fate of the developing larva in the most fundamental way.

In conclusion, isotropic and anisotropic active tensions act together to generate the cell ingressions during pseudocleavage and cytokinesis. While the pseudocleavage furrow has no known functional relevance, and can be understood as a phenomenon arising from the particular cortical dynamics taking place during cell polarization, the cytokinetic ring is subject to a spatiotemporal regulatory machinery ensuring the proper positioning and successful completion of cell cleavage.

List of symbols

i, j, \dots	Indices of the coordinates on the surface
α, β, \dots	Indices of cartesian coordinates x, y, z
t	Time
s	Arclength surface coordinate
ϕ	Angle surface coordinate
∇_i	Covariant derivative operator
Q_{ij}	Nematic order parameter
n_i	Nematic director field
h_i	Molecular field
F_n	Nematic free energy
f_n	Nematic free energy density
χ	Inverse nematic susceptibility
ι	Nematic elastic constant
τ	Characteristic nematic time scale
l	Characteristic nematic length scale
β	Flow-alignment coupling coefficient
t_{ij}	Tension tensor
v_{ij}	Symmetric velocity gradient tensor
$P_{\text{int}}, P_{\text{ext}}$	Intracellular and extracellular pressures acting on the cortex
v^s	Velocity of flow within the surface
v^n	Velocity normal to the surface
v_{ij}	Symmetric velocity gradient tensor
η_b	Bulk viscosity
η_s	Shear viscosity
ζ, ξ	Isotropic and anisotropic active tension coefficients

\mathbf{X}	Axisymmetric surface representing the cell cortex
$\mathbf{e}_x, \mathbf{e}_y, \mathbf{e}_z$	Cartesian basis vectors
r	Shape of the axisymmetric surface
ψ	Surface angle
I	Relative myosin fluorescence intensity
$\zeta^{(0)}, \xi^{(0)}$	Proportionality constants between myosin intensity and isotropic and anisotropic active tension
R	Radius of the egg shell
$\delta\zeta, \delta\xi$	Deviations from a uniform active tension profile
$\delta r, \delta v^s, \delta Q_{ij}, \delta P$	Deviations from the cylindrical reference solution
C_1, C_2	Integration constants
s_1, s_2	Contact points between the cortex and the egg shell
p_1, p_2, p_3	Parameters
S	Objective function
N_{pc}, N_{ck}	Number of available datapoints for pseudocleavage and cytokinesis

Chapter 5

Nuclear movements in pseudostratified epithelia

The vertebrate organism is composed of thousands of different cell types, which form a variety of organs and tissues with diverse morphologies, physical properties and functions. While the preceding chapters have focused on the cytoskeletal mechanics of isolated single cells, we now consider cells within their tissue context. Our structure of interest is the pseudostratified epithelium, an embryonic tissue found in a wide range of organisms from different phyla, including vertebrates, where it forms the basis of the developing nervous system [126, 87]. These tissues consist of densely packed elongated cells, which exhibit characteristic movements of the nuclei [78] along the long cell axis, coordinated with the cell division cycle. We aim to obtain a detailed understanding of the mechanics of nuclear movements in pseudostratified epithelia, and address how the properties of the constraining tissue influence the mechanics of nuclear movements within single cells. We begin by analyzing a simplified, three-dimensional description of a pseudostratified tissue, and derive a theoretical relationship between the large-scale elastic properties of the epithelium, and the mechanical and geometric parameters of its constituting single cells. In the second part of this chapter, we return to the framework used in previous chapters, and present a single-cell theory, which explores possible mechanisms underlying the nuclear movements observed within the cells of pseudostratified tissues.

5.1 Pseudostratified epithelia and interkinetic nuclear migration

All components of the central nervous system in vertebrates develop from pseudostratified neuroepithelia. These comprise of a single stratum of cells with well-defined polarity between the apical and basal sides of the cells [48]. The nuclei of neuroepithelial cells are distributed along the apico-basal cell axis, giving rise to a layered appearance of the tissue, hence the name pseudostratified epithelium (see Figure 5.1). Furthermore, the nuclei in these highly proliferative tissues exhibit characteristic movements, which are coordinated with the cell division cycle

[114]; for historic reasons, these movements are termed “interkinetic nuclear migration” (INM). In the last phase of the cell cycle before division, the nuclei travel to the apical side of the cell, where they undergo mitosis and cytokinesis, such that all cell divisions take place at the apical surface of the epithelium (see Figure 5.1 B). Several studies show a link between perturbed INM and impairments in neural development [33, 121]. It has been proposed that the location of the nucleus along the cell axis regulates its exposure to signaling molecules, such that INM may function as a cell-intrinsic timer for differentiation [33, 126]. Furthermore, many polarity cues are contained in the apical domain of neuroepithelial cells [19]. INM thus may function to maintain tissue integrity by restricting cell divisions to the apical side of the epithelium [121]. These nuclear movements are not specific to neural tissues however. They have been observed in all pseudostratified epithelia, and in a wide variety of organisms, including anemones, insects and mammals [87]. The molecular machinery underlying INM however appears to differ between tissues and organisms in a possibly size-dependent manner. In the highly elongated cells of the vertebrate neocortex, nuclear movements rely on active transport along the microtubule cytoskeleton, driven by dynein and possibly kinesin motors coupled to the nucleoskeleton via protein complexes spanning the nuclear envelope [129] (see Section 1.1.1). In shorter cells, for example in the wing disc of *Drosophila* pupae, or in the developing retina of the zebrafish *Danio rerio*, INM depends on actomyosin and appears highly robust with respect to perturbations of the microtubule system [97, 87]. While migration to the apical side prior to cell division is directed, subsequent basal displacements of the daughter nuclei are stochastic and can be explained as a passive effect arising from the motion of other nuclei in the tissue [80]. Here, we focus on the mechanics of actomyosin-driven apical migration of nuclei in pseudostratified epithelia.

5.2 Nuclear movements in cells of pseudostratified epithelia

We consider single cells embedded in a pseudostratified epithelium, and explore mechanisms potentially underlying the characteristic nuclear movements observed in these cells. We take the cortical shell to be an axisymmetric, viscous surface, subjected to myosin-induced active tension (see Figure 5.2 A). Thus, we neglect deviations from axisymmetry imposed by neighboring cells and consider a time- or tissue-average cell shape; in analogy with simple foam models, where individual bubbles are treated as spherical (e.g. [37]). Furthermore, the shell is assumed to surround a conserved volume. As detailed in Section 2.4, for a segment of length L , the choice $V = \pi R^2 L$ leads to the simplest steady state solution, a straight cylinder. We begin by discussing the stability of this solution in the presence of external elastic stresses, which result from the surrounding cells, and proceed to derive a general solution for the shape and flow of the cortex for small deviations from the cylindrical volume. Next, we investigate the movement of the nucleus. Focusing on the active apical migration of nuclei [80], we explore different scenarios leading to persistent apical motion, driven by myosin-dependent contractility in the cortical shell. These involve different regimes of nucleo- and cell-mechanical parameters, as well as different profiles of active tension along the cell. We divide the cell into three segments, a basal, an apical and a nuclear segment (see Figure 5.3) with lengths $L^{(b)}$, $L^{(n)}$ and $L^{(a)}$ respectively, and let the shape

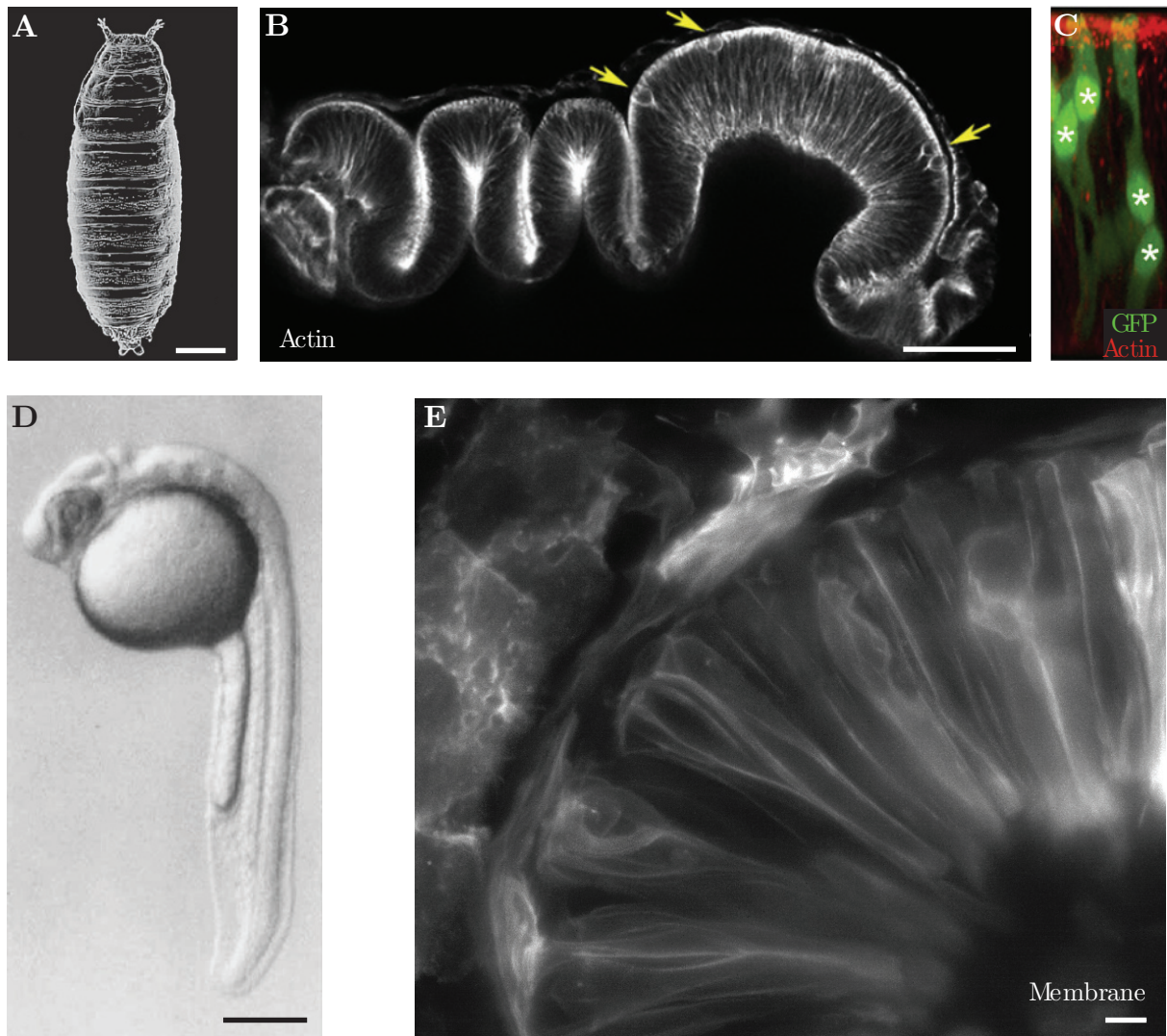


Figure 5.1: Examples of pseudostratified tissues in developing organisms.

A. Pupa of the fruit fly *Drosophila melanogaster* (scanning electron micrograph). Scale bar: 100 μm . Image taken from [137]. **B.** Fluorescently stained image of the pseudostratified epithelium in the developing *Drosophila* wing, viewed from the lateral side. Actin filaments are stained with phalloidin. Yellow arrows denote cells rounded up for division, which always takes place on the apical side of the epithelium. Scale bar: 50 μm . Image taken from [87]. **C.** Mosaic of labeled cells within the wing disc. The nuclei are distributed along the apico-basal cell axis. Image taken from [87]. **D.** Bright field image of the embryo of the zebrafish *Danio rerio*. Scale bar: 250 μm . Image taken from [68]. **E.** Maximum projection fluorescence image of the developing zebrafish retina with labeled cell membranes (Ras-GFP). Cells are tightly packed. Scale bar: 10 μm . Image recorded by M. Matejic (2014).

of the basal and apical segments be governed by the cortex equations introduced in Section 2.4, where we now also take into account the elasticity of the surrounding tissue. Basally, adhesive structures anchor the cells to an extracellular basal lamina, and the apical surfaces are spanned by the adherens junction network and associated actin cables [48]. We assume here that these non-cortical structures control the apical and basal surfaces, and consider the cell shape to be constrained on both apical and basal sides to a fixed radius R . In the nuclear segment, the shell is also set to a prescribed nuclear shape. In the pseudostratified epithelial cells of the zebrafish retina, the nuclei indeed appear to bulge the cell cortex, see Figure 5.3 A. We consider the nucleus to be a rigid cylindrical body, but the description may be improved by using nuclear shapes measured from microscopy images. For simplicity, the radius of the nucleus is also chosen to be R , i. e. equal to the radii at the boundaries of the cell. We consider a profile of active tension within the cortical surface, taking constant values along the basal and apical segments, and decreasing linearly in the nuclear segment (see Figure 5.3 C)

$$\zeta(s) = \begin{cases} \zeta^{(b)} & \text{in the basal segment} \\ \zeta^{(b)} - \frac{\zeta^{(b)} - \zeta^{(a)}}{L^{(n)}}(s - L^{(b)}) & \text{in the nuclear segment} \\ \zeta^{(a)} & \text{in the apical segment.} \end{cases} \quad (5.1)$$

With these assumptions, we derive differential equations for the position of the nucleus and the distribution of cytoplasmic volume between basal and apical segments, where we take the segment shapes to relax to equilibrium much faster than the dynamics of nuclear position and segment volumes. We explore the behavior of the system in different regimes of the parameters.

5.2.1 Segment shapes

Stability

First, we consider the shape of a single segment with length L and volume V (Figure 5.2 A). The linearized cortex equations for cylindrical shapes are derived in Section 2.4, and read

$$0 = \frac{\zeta(2\eta_b - \eta_s)}{R(2\eta_b + \eta_s)} \partial_s \delta r + \frac{R\zeta(2\eta_b - \eta_s)}{2\eta_b + \eta_s} \partial_s^3 \delta r + \frac{4\eta_b \eta_s}{2\eta_b + \eta_s} \partial_s^2 \delta v^s, \quad (5.2)$$

$$\partial_t \delta r = \frac{2\zeta}{2\eta_b + \eta_s} \delta r + \frac{2R^2 \zeta}{2\eta_b + \eta_s} \partial_s^2 \delta r - \frac{R(2\eta_b - \eta_s)}{2\eta_b + \eta_s} \partial_s \delta v^s + \frac{2R^2}{2\eta_b + \eta_s} \delta P. \quad (5.3)$$

For cells embedded in an epithelial tissue, external elastic forces act on the surface of single cells, arising from the presence of their neighbors. We represent these elastic stresses by introducing an elastic constant κ associated to deformations away from the reference shape given by R . The pressure difference on the cortical shell can then be written as

$$\delta P = \delta P_{\text{int}} - \kappa \delta r, \quad (5.4)$$

and Equation 5.3 modifies to

$$\partial_t \delta r = \frac{2(\zeta - R^2 \kappa)}{2\eta_b + \eta_s} \delta r + \frac{2R^2 \zeta}{2\eta_b + \eta_s} \partial_s^2 \delta r - \frac{R(2\eta_b - \eta_s)}{2\eta_b + \eta_s} \partial_s \delta v^s + \frac{2R^2}{2\eta_b + \eta_s} \delta P_{\text{int}}. \quad (5.5)$$

Following the steps presented in Section 2.4.1, we uncouple the flow and shape equations, and perform the substitution $\delta r(s, t) = \tilde{\delta r}(s) \exp(\omega t)$. We ask whether the cylindrical steady state solution is stable with respect to the perturbations δr , we seek for the conditions giving rise to a positive growth rate ω . As before, we recover that the shape perturbation has the form (see Equation 2.47 in Section 2.4.1)

$$\delta r = A \cos(\lambda s) + B \sin(\lambda s) + C, \quad (5.6)$$

where C is a constant in t and s , A and B are constants in s , and the wavelength is given by

$$\lambda = \frac{1}{R} \sqrt{1 - \frac{R^2 \kappa + \tilde{\eta} \omega}{\zeta}}, \quad (5.7)$$

where again $\tilde{\eta} = 4\eta_b \eta_s / (2\eta_b + \eta_s)$. Perturbations grow over time, if $\omega > 0$, or equivalently, if

$$\zeta - R^2(\lambda^2 \zeta + \kappa) > 0. \quad (5.8)$$

For the boundary conditions considered here, given by $\delta r(0) = \delta r(L) = 0$, the length of the segment L imposes a lower bound on the wavelength $\lambda \geq 2\pi/L$ (see Section 2.4.1). Thus, for a segment of arbitrary length, stability is achieved if $\kappa > \zeta/R^2$, i. e. the stability of the segment shape depends on the elastic constant κ , the active tension ζ and the cylinder radius R (Figure 5.2). If the contractile active tension dominates over the elastic tension, shells of greater length than perimeter undergo a Plateau-Rayleigh instability (Section 2.4.1 and [38]). In the following, we consider parameter regimes, where the cell segments maintain stable steady state shapes.

Segment shapes at different volumes

The cell segment volume may not exactly correspond to the volume of a cylinder. In this section, we derive the solution for the steady state shape at volumes close to $V_0 = \pi R^2 L$. We impose that the volume is given by $V = V_0 + \delta V$ and expand the steady state equations in δV , obtaining

$$0 = \left(\eta_b + \frac{1}{2} \eta_s \right) \partial_s^2 \delta v^s, \quad (5.9)$$

$$\delta P_{\text{int}} = \left(\kappa - \frac{\zeta}{R^2} \right) \delta r - \zeta \partial_s^2 \delta r + \frac{2\eta_b - \eta_s}{2R} \partial_s \delta v^s. \quad (5.10)$$

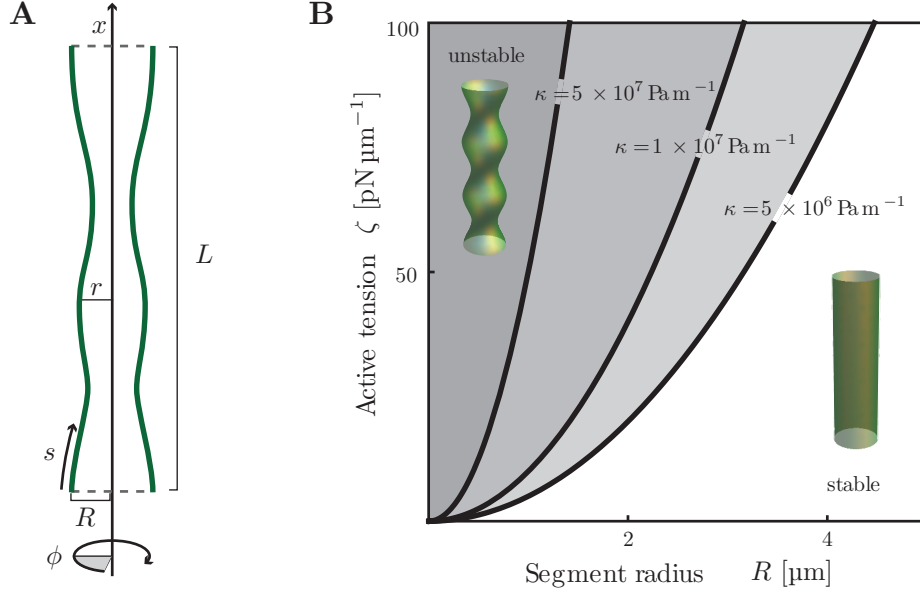


Figure 5.2: Linear stability analysis of cortex shell segments with external elasticity. **A.** Parameterization of cortex shell segments with length L and boundary radius R . **B.** Stability diagram of cortex shell segments with external elasticity. Cylindrical shapes with large aspect ratios found in the cells of most pseudostratified tissues (i. e. $R : L > 1 : 10$) are stable, if the elastic stresses exerted by the surrounding tissue, characterized by the constant κ , dominate over the effect of contractile active tension ζ . The stability criterion in the limit $L \rightarrow \infty$ reads $R^2\kappa > \zeta$ (solid line, for different values of κ).

These equations are solved by

$$\delta v^s = C_1 + C_2 s \quad (5.11)$$

$$\delta r = -\frac{2R^2\delta P_{\text{int}} + C_2 R(\eta_s - 2\eta_b)}{2(\zeta - R^2\kappa)} + \frac{C_3 2(\zeta - R^2\kappa) + C_2 R(\eta_s - 2\eta_b)}{2(\zeta - R^2\kappa)} \cosh\left(\frac{s}{l}\right) - \frac{C_4 R^2 \zeta}{l(\zeta - R^2\kappa)} \sinh\left(\frac{s}{l}\right), \quad (5.12)$$

where the characteristic length is given by $l = R^2\zeta/\sqrt{R^2\zeta(R^2\kappa - \zeta)}$, and $C_1 = \delta v^s(0)$ and $C_2 = (\delta v^s(L) - \delta v^s(0))/L$.

We use the following conditions to obtain expressions for C_3 and C_4

$$\delta r(s=0) = 0, \quad (5.13)$$

$$\delta r(s=L) = 0. \quad (5.14)$$

By this choice, we assume that the shape is fixed to $r = R$ at the boundaries, which - depending on the segment - correspond to the basal or apical boundary and the contact point with the

nucleus. We obtain

$$C_3 = \frac{R^2 \delta P_{\text{int}}}{\zeta - R^2 \kappa}, \quad (5.15)$$

$$C_4 = \frac{\left(e^{\left(\frac{L}{l}\right)} - 1\right) l (C_2(\eta_s - 2\eta_b) + 2R\delta P_{\text{int}})}{2\left(e^{\left(\frac{L}{l}\right)} + 1\right) R\zeta}. \quad (5.16)$$

Finally, we determine δP_{int} by imposing that the volume has to be conserved. To linear order, the volume can be written as

$$V = V_0 + \delta V = \pi \int_0^{s_{\text{max}}} ds (r_0 + \delta r)^2 \sin(\psi_0 + \delta\psi) \approx \pi R^2 L + 2\pi R \int_0^L ds \delta r, \quad (5.17)$$

where we used that

$$\partial_s x = \sin \psi = \sqrt{1 - \cos\left(\frac{\pi}{2} + \delta\psi\right)} = 1 + \mathcal{O}(\delta\psi^2), \quad (5.18)$$

and thus $L \approx s_{\text{max}}$. The internal pressure is given by

$$\delta P_{\text{int}} = \frac{C_2(2\eta_b - \eta_s)}{2R} + \frac{\zeta - R^2 \kappa}{2\pi R^3 \left(2l \tanh\left(\frac{L}{2l}\right) - L\right)} \delta V, \quad (5.19)$$

and the final solution reads

$$\delta r = \frac{\sinh\left(\frac{L-s}{2l}\right) \sinh\left(\frac{s}{2l}\right)}{L\pi R \cosh\left(\frac{L}{2l}\right) - 2l\pi R \sinh\left(\frac{L}{2l}\right)} \delta V. \quad (5.20)$$

Thus, for a given length L and volume V of the apical and basal segments, we can express the shape of the cortical shell as a function of the characteristic length l , set by the mechanical parameters κ and ζ .

Cortical flow field

The force balance equation in the direction tangential to the cortical surface leads to a differential equation governing the flow field within the surface, given by Equation 5.9 for the basal and apical segments. In these cell parts, the flow field is linear (see Equation 5.11). In the nuclear segment, the active tension is not constant, but is assumed to change linearly (see 5.1). Furthermore, where the cortex is in contact with the nuclear envelope, we associate a friction coefficient α to movements of the cortex relative to the nucleus. Thus, for the nuclear segment, Equation 5.9 modifies to

$$\alpha \left(\delta v^s - \frac{dL^{(b)}}{dt} \right) = \frac{\zeta^{(a)} - \zeta^{(b)}}{L^{(n)}} + \left(\eta_b + \frac{1}{2}\eta_s \right) \partial_s^2 \delta v^s, \quad (5.21)$$

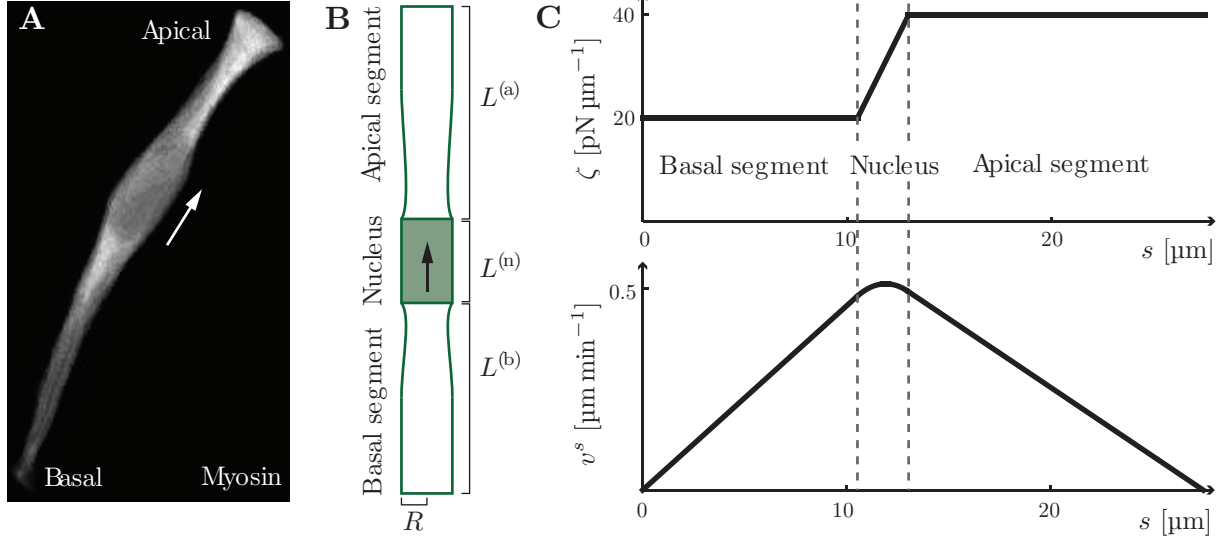


Figure 5.3: Three-segment description of cells in pseudostratified epithelia.

A. Fluorescence microscopy image of an embryonic zebrafish cell embedded in the developing pseudostratified retina, obtained by mosaic fluorescence labeling and cell shape segmentation. The cell nucleus is migrating towards the apical side of the epithelium before cell division. Arrow denotes direction of the nucleus. Image recorded by H. O. Lee (2013). **B.** Schematic of segment arrangement in the single-cell description. **C.** Example profiles of active tension ζ and cortical flow field v^s . Parameters are listed in Figure 5.4 E (right).

which is solved by

$$\delta v^s = C_1^{(n)} e^{s \sqrt{\frac{2\alpha}{2\eta_b + \eta_s}}} + C_2^{(n)} e^{-s \sqrt{\frac{2\alpha}{2\eta_b + \eta_s}}} + \frac{dL^{(b)}}{dt} + \frac{\zeta^{(a)} - \zeta^{(b)}}{L^{(n)}\alpha}. \quad (5.22)$$

Connecting this solution to Equation 5.11 for the flow in the apical and basal segments, imposing that the velocity profile has to be smooth and continuous at $L^{(b)}$ and $L^{(b)} + L^{(n)}$, and using that the velocity has to vanish at the apical and basal boundaries $v^s(s = 0) = 0$, and $v^s(s = L^{(b)} + L^{(n)} + L^{(a)}) = 0$, we can compute all integration constants and obtain the profile of cortical flow along the cell as a function of the velocity of the nucleus. Figure 5.3 C shows an example.

5.2.2 Nuclear dynamics

We now derive differential equations governing the position of the nucleus, and the flow of cytoplasmic volume between the basal and apical segments, assuming that segment shapes relax to equilibrium fast, compared to the dynamics of nuclear position and segment volumes. Importantly, the total length of the apical and basal segments $L_{\text{tot}} = L^{(a)} + L^{(b)}$ - corresponding to the length of the cell without the nucleus -, as well as the total apical and basal volume $V_{\text{tot}} = V^{(b)} + V^{(a)}$ are considered fixed. The position of the nucleus is expressed in terms of the length of the basal segment $L^{(b)}$, and the distribution of cytoplasmic volume by the basal volume $V^{(b)}$. We consider a frictional force, arising from the movement of the nucleus relative to the cortex, as well as the fluid pressure acting on the basal and apical contact areas between

the nucleus and the cytoplasm, and write that the sum of forces on the nucleus must be zero

$$\alpha 2\pi R \int_{L^{(b)}}^{L^{(b)}+L_n} ds \left[\delta v^s - \frac{dL^{(b)}}{dt} \right] + 2\pi R^2 (P^{(b)} - P^{(a)}) = 0, \quad (5.23)$$

with $P^{(b)}$ and $P^{(a)}$ the intracellular pressures in the basal and apical segments respectively. Furthermore, we consider the nuclear segment to be permeable to fluid flow. With ξ denoting the fluid flow resistance of the nuclear segment, the equation for the volumetric flow rate in the reference frame of the nucleus reads

$$P^{(b)} - P^{(a)} = -\xi \frac{d(V^{(b)} - V^{(a)})}{dt}, \quad (5.24)$$

which can be recast into

$$\frac{dV^{(b)}}{dt} = -\frac{1}{2\xi} (P^{(b)} - P^{(a)}), \quad (5.25)$$

using that $dV_{\text{tot}}/dt = 0$. Equations 5.23 and 5.25 describe the movement of the nucleus and the flow of cytoplasmic volume in the cell, given the segment pressures $P^{(b)}$ and $P^{(a)}$, and the velocity of cortical material v^s . For a given length and volume of the segments, the expressions for $P^{(b)}$, $P^{(a)}$ and v^s are obtained from the calculations presented in Section 5.2.1 using Equations 5.19 and 5.22, where $P^{(b)} = \zeta^{(b)}/R + \delta P_{\text{int}}^{(b)}$, and $P^{(a)} = \zeta^{(a)}/R + \delta P_{\text{int}}^{(a)}$. Starting from some initial configuration, we can thus compute step by step how the nucleus and the cytoplasm move in response to the frictional and pressure forces arising from the active stresses in the cortical shell, and at each step, we obtain the shape of the segments, and the flow profile in the cortex.

Given a difference in active tension between the basal and apical segments, competing effects arise from the pressure and the frictional forces acting on the nucleus. Figure 5.4 shows the trajectories for two limiting cases, which both lead to apical migration of the nucleus as observed in the cells of pseudostratified epithelia. If the frictional coupling between the cortex flow and the nucleus is negligible compared to the resistance to cytoplasmic flow offered by the nuclear segment, the pressure gradient arising from the difference in cortical active tension between the segments pushes the nucleus towards the side of lower active tension. For $\zeta^{(b)} > \zeta^{(a)}$, this effect may result in the apical migration of the nucleus (see Figure 5.4 C - E, left panels). Since the cytoplasm cannot flow opposite to the direction of the pressure gradient, the volume of the apical segment inflates over time in this case. In the second case, the frictional effect dominates over the bulk flow effect; assuming $\zeta^{(a)} > \zeta^{(b)}$, the material in the cortical layer moves from the basal towards the apical side, and entrains the nucleus at the contact area between cortex and nuclear envelope, pulling it towards the apical side (Figure 5.4 C - E, right panels). Depending on the magnitude of the flow resistance ξ of the nuclear segment, some fluid may pass through the nucleus from the apical to the basal side during movement.

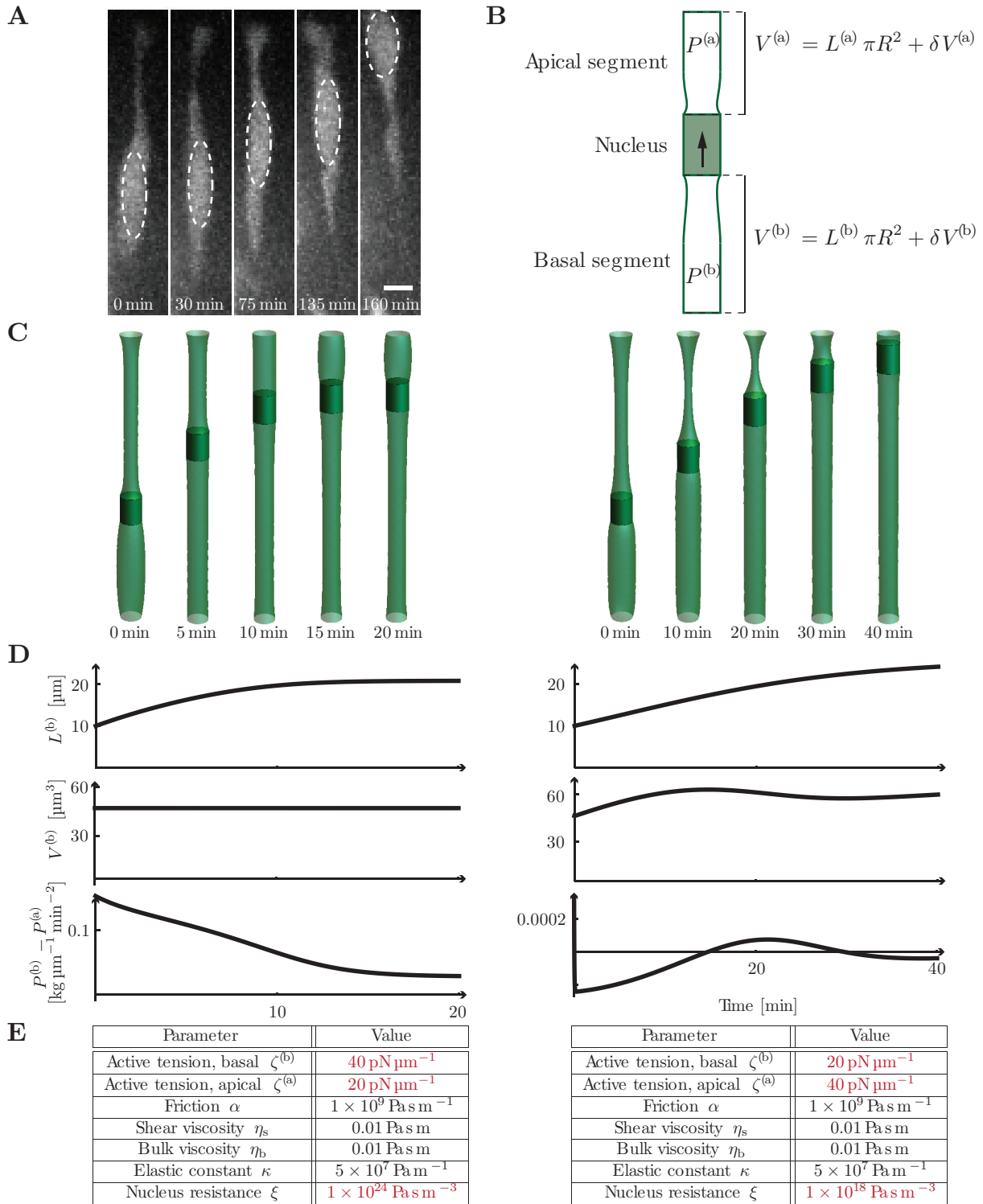


Figure 5.4: Apical migration of cell nuclei.

A. Time-lapse fluorescence microscopy images of an embryonic retinal cell of the zebrafish, expressing fluorescent cytoplasmic GFP. The nucleus (indicated by dotted outline) migrates to the apical side of the epithelium. Scale bar: 5 μm . Images obtained by I. Yanakieva (2015). **B.** Schematic of the pressures and volumes of the apical and basal segments in the theoretical description. **C.** Time-lapse representation of simulations of the three-segment model with the parameters given below. Left panels: for $\zeta^{(b)} > \zeta^{(a)}$ and a large flow resistance in the nuclear segment, apical migration is driven by the intracellular pressure difference. Right panels: for $\zeta^{(a)} > \zeta^{(b)}$ and a small flow resistance in the nuclear segment, apical migration results from friction with the cell cortex, which flows towards the apical side. **D.** Corresponding time evolutions of the nuclear position (top panels), the basal volume (middle panels) and the pressure difference across the nucleus (bottom panels). **E.** Parameter tables for the simulations in the left and right panels. Cell geometric parameters: $R = 1 \mu\text{m}$, $L^{(n)} = 2.5 \mu\text{m}$, $L_{\text{tot}} = 25 \mu\text{m}$.

5.3 Discussion

Interkinetic nuclear migration is a highly conserved feature of developing pseudostratified tissues including neuroepithelia [87, 125]. In vertebrates, INM is a prerequisite for orchestrated neurogenesis [125, 121]. Here, we explored different possible mechanisms underlying INM in single cells.

5.3.1 Investigating force generation during nuclear movements in pseudostratified cells

We developed a simplified description of a single cell embedded within an epithelial tissue, taking into account the presence of the cell nucleus, which divides the cell into basal and apical compartments (see Figure 5.3). To develop hypotheses regarding the mechanisms of force generation, we explored the behavior of this system given different assumption on nuclear and cell mechanical parameters. Specifically, dividing the cell into a basal, an apical and a nuclear segment, we studied the effect of different distributions of active tension within the walls of the segments. We found two regimes of the governing parameters, where apical migration of nuclei occurs as observed in the cells of pseudostratified tissues (Figure 5.4). Increased active tension in the basal segment compared to the apical segment can induce an intracellular pressure difference, which pushes the nucleus towards the apical side (see Figure 5.4 left panels). Alternatively, assuming an inverted active tension distribution, which is larger in the apical than in the basal segment, nuclear migration can result from cortical flows dragging the nucleus to the apical side (Figure 5.4 right panels). During pressure-driven nuclear migration, the volume of the basal segment is required to decrease or remain constant, because the cytoplasmic flow follows the pressure gradient in the cell. Preliminary data for cells in the developing zebrafish retina indicate that the dynamics of cytoplasmic volume during nuclear migration are not in agreement with the pressure-dependent model: the volume of the basal segment of these cells appears to increase during nuclear migration (data from independent experiments by H.O. Lee and I. Yanakieva, unpublished), suggesting that cytoplasmic fluid passes through the nuclear segment towards the basal side during apical movement. The second, friction-dependent mechanism may in principle allow for the observed volume dynamics (see Figure 5.4 D). This effect relies on the mechanical coupling between the cell cortex and the nucleus. In our theoretical description, we have made the assumption that a fixed contact area is created between the nucleus and the cortex, as may arise from connections between the nucleoskeletal structures underneath the nuclear envelope and the actin cytoskeleton. Such nucleo-cortical couplings, mediated by protein complexes spanning the nuclear membrane layer, have been shown to reposition the nucleus in fibroblasts polarizing for migration [84, 85]. Strikingly however, in the pseudostratified epithelium of the embryonic retina, it has been shown that apical migration can take place in the absence of a nuclear envelope. In these experiments, nuclear envelope breakdown and formation of the mitotic spindle had been initiated at a basal location by appropriate manipulations of centrosomes [121]. The structure formed by the spindle and the chromosomal material was subsequently seen to migrate to the apical surface of the cell. While this observation casts

doubt on the nuclear envelope playing any key role in mediating apical movement, the involved experimental disruptions may have introduced unphysiological conditions, potentially triggering cellular rescue mechanisms, which are distinct from the natural processes.

Aside from the mechanisms explored here, several other effects may drive actomyosin-dependent nuclear migration in the cells of pseudostratified epithelia, including processes involving cytoplasmic rather than cortical actin structures, which have been shown to mediate subcellular motility in other systems [136, 92]. The theoretical exploration presented here thus forms a basis from which implications and requirements for different mechanisms can be derived, and more detailed hypotheses can be formulated. An estimation of the active stress fields present during nuclear migration will be a necessary step to understand the mechanical processes resulting in the nuclear migration of pseudostratified cells. This may be achieved for example by obtaining the spatiotemporal distribution of active molecular motors in the actin cytoskeleton during nuclear migration. Combining theoretical findings with experimental observations may then allow to quantitatively understand the principle of force generation during interkinetic nuclear migration.

List of symbols

i, j, \dots	Indices of the coordinates on the surface
α, β, \dots	Indices of cartesian coordinates x, y, z
(b), (n), (a)	Superscripts denoting the basal, nuclear and apical segments of the cell
t	Time
s	Arclength surface coordinate
ϕ	Angle surface coordinate
∇_i	Covariant derivative operator
L	Segment length
V	Segment volume
R	Radius at the apical and basal boundaries, and radius of the nucleus
r	Shape of the axisymmetric surface
ψ	Surface angle
t_{ij}	Tension tensor
$P_{\text{int}}, P_{\text{ext}}$	Intracellular and extracellular pressures acting on the cortex
v^s	Velocity of flow within the surface
v^n	Velocity normal to the surface
v_{ij}	Symmetric velocity gradient tensor
η_b	Bulk viscosity
η_s	Shear viscosity
ζ	Active tension
κ	Elastic constant
$\delta r, \delta v^s, \delta P$	In Eq.'s 5.2 - 5.7: dynamic perturbations. In Eq.'s 5.9 and following, deviations from the cylindrical reference solution
$\tilde{\eta}$	Viscosity parameter, $\tilde{\eta} = 4\eta_b\eta_s/(2\eta_b + \eta_s)$
ω	Perturbation growth rate

λ	Perturbation wavelength
A, B, C	Constants
l	Hydrodynamic length, $l = R^2\zeta\sqrt{R^2\zeta(R^2\kappa - \zeta)}$
C_1, C_2, C_3, C_4	Integration constants
α	Friction coefficient
L_{tot}	Total basal and apical segment length, $L_{\text{tot}} = L^{(\text{b})} + L^{(\text{a})}$
V_{tot}	Total basal and apical segment volume, $V_{\text{tot}} = V^{(\text{b})} + V^{(\text{a})}$
ξ	Hydraulic resistance of the nuclear segment

Chapter 6

Concluding remarks

We have presented here a theory of the actomyosin cytoskeleton as a continuous material with intrinsic active properties, applied it to a number of different biological problems, and successfully integrated this framework with experimental measurements. We summarize here the main findings from our studies of different aspects of cell mechanics.

In Chapter 3, we investigated the mechanics of non-adhesive cell migration. Adhesive structures, which couple a cell's cytoskeleton to its substrate, constitute an indispensable part of the migratory machinery in most cells capable of self-propelled motion. We investigated the mechanisms underlying the motile behavior of cancer cells in confining environments, which migrate without such adhesive structures. We identified the physical principles underlying this type of non-adhesive cell motility by analyzing the dynamics of the actomyosin cortex in these cells during movement. Actomyosin-intrinsic forces generate rearward flows in the actomyosin cortex of these migrating cells, and result in the contraction of the cell rear and the simultaneous expansion at the front. These surface flows and cell deformations enable self-propelled motion through environments, in which sufficient substrate friction is provided to generate the thrust required to overcome any arising fluid drag forces. We identified the different parameter regimes of cell motility for cells migrating in microfluidic channels, deriving, and validating with experimental measurements, the relationship between cell velocity, cortical flow profiles and substrate friction. Our analysis furthermore allowed us to quantify the forces exerted by these non-adhesive cells on their surroundings during migration, uncovering fundamental differences to adhesive cell migration modes, which rely on significantly larger traction stresses and an inverted force distribution. We discussed the implications of these findings for cellular interactions during collective cell migration.

In Chapter 4, we investigated the initiation of cell furrowing during cytokinesis. The division of cells relies on highly coordinated processes within the actomyosin cell cortex. These result in the formation of a contractile ring structure, which drives the ingression of a cleavage furrow to divide the cytoplasm in half. Both biochemical regulation, involving local modifications of the cortical actin architecture, and mechanical feedback effects in the cortical layer contribute to

the assembly of the cytokinetic contractile ring. We studied the mechanical aspects of furrow initiation in the one-cell embryo of the nematode *C. elegans*. The actomyosin cortex of dividing *C. elegans* embryos features distinct and reproducible patterns of actin filament alignment. To describe these, we introduced a nematic term in our description, which accounts for the particular geometry of actin filaments, and generates an anisotropy in the cortical tension. We investigated the role of this anisotropy during the formation of the cell division furrow, and showed that mechanical effects alone, resulting from the couplings between cortical flows, filament ordering and cell shape, can generate a furrow ingression. This mechanism explains the phenomenon of pseudocleavage formation in the *C. elegans* embryo and may play a role in other cellular systems where the actin architecture allows for the nematic ordering of filaments.

Finally, we studied aspects of the mutual influence between single-cell level processes and the emergent properties of the constituted tissues in the context of nuclear movements in cells of pseudostratified epithelia. Before undergoing cytokinesis, the cells within these highly proliferative, tightly packed tissues translocate the nucleus to the apical side of the epithelium. In several tissues, this process is known to be mediated by the actin cytoskeleton and dependent on myosin II activity, but the physical principles of these movements are not understood. We first reported some general theoretical findings on the behavior of pseudostratified epithelia, and then explored different potential mechanisms leading to apical nuclear movements in a simplified description of a pseudostratified epithelial cell. In our model, apical translocation may occur as a consequence of either an intracellular pressure difference between the basal and apical parts of the cell, or resulting from frictional coupling between the nucleus and the flowing cell cortex. We discuss the implications and requirements for these mechanisms, and suggest how we may combine our theoretical findings with experimental observations, to gain an understanding of actomyosin dependent nuclear migration in pseudostratified epithelia.

While most parts of this work focused on the cytoskeletal processes of single cells in isolation, future efforts are to address the mutual influence between the mechanics of single cells and their surroundings within their natural tissue context. With the rapidly improving technical and computational capabilities available for data acquisition, there is an increasing potential and relevance for applying more and more detailed theoretical concepts to complex *in vivo* systems [115, 57]. The detailed quantitative characterization of cellular processes may provide the next steps towards understanding how the properties of tissues and organs emerge from single cell level phenomena in the development and functioning of living organisms.

Appendix A

Hydraulics of microfluidic channels with migrating cells

In this appendix, we discuss fluid mechanical aspects of the microfluidic systems, which were used to study migrating Walker cells, as described in Chapter 3. Specifically, we derive here i) the relationship used to calculate the friction coefficient between the walls of a microfluidic channel and an inserted cell's surface (see Section 3.2.3), ii) the equation for the average fluid flow induced by migrating cells in a channel, used to verify the fitted estimate for the flow resistance of a single cell ξ (see Section 3.2.3), and iii) the expression for the fluid drag coefficient α_D (see Section 3.2.2). We begin by considering the simple case of a single cell inserted into a microfluidic channel, as shown in Figure A.1 (top). The difference of pressure applied to the channel inlet and outlet $P_{\text{applied}} = P_{\text{in}} - P_{\text{out}}$ is related to the pressure difference on the cell $P_{\text{cell}} = P_{\text{ext}}^{(\text{r})} - P_{\text{ext}}^{(\text{f})}$ by

$$P_{\text{applied}} = \xi_{\text{ext}} \pi R^2 \bar{v}_{\text{ext}} + P_{\text{cell}}, \quad (\text{A.1})$$

where ξ_{ext} is the hydraulic resistance of the microfluidic channel, given by $8\eta_{\text{ext}}L_{\text{ext}}/(R^4\pi)$, and \bar{v}_{ext} denotes the average flow velocity of the external medium in the channel. The pressure on the cell is given by

$$P_{\text{cell}} = \xi \pi R^2 (\bar{v}_{\text{ext}} - U). \quad (\text{A.2})$$

Rewritten in terms of the effective friction χ resulting from the relative movements of the cell surface with respect to the channel walls at the contact surface (see Section 3.2.2, Equation 3.30), this pressure difference can be re-expressed as a function of the intrinsic cell velocity U_0

$$P_{\text{cell}} = \chi(U - U_0). \quad (\text{A.3})$$

We use these relations to estimate the friction coefficient arising in channels treated with different coating compounds, as described in Section 3.2.3 (see also Figure 3.9 A). These experiments were performed on unpolarized cells, for which $U_0 = 0$. Then, the cell velocity and the fluid velocity are related by

$$\bar{v}_{\text{ext}} = \left(1 + \frac{\chi}{\xi \pi R^2}\right) U, \quad (\text{A.4})$$

and the pressure difference applied to the microfluidic channel is given by

$$P_{\text{applied}} = \left(\chi \left(\frac{\xi_{\text{ext}}}{\xi} + 1 \right) + \xi_{\text{ext}} \pi R^2 \right) U. \quad (\text{A.5})$$

For unpolarized cells without surface flow, we compute the resistance of the cell to displacement χ by integrating the friction force density αU over the contact surface, assuming that the cell behaves as a solid object. We find $\chi = 2L\alpha/R$, and recover the relation given by Equation 3.39.

In the experiments monitoring the actomyosin cortex dynamics exhibited by Walker cells during migration, the microfluidic channels were submerged in a fluid bath such that no externally applied pressure was present, $P_{\text{applied}} = 0$. Then, for a single cell in the channel, Equation A.1 simplifies to

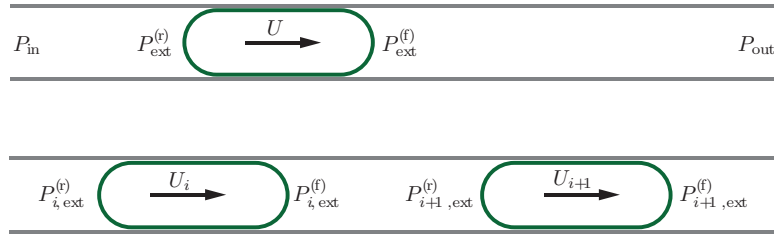


Figure A.1: Schematic representation of the pressures acting on single cells (top panel) and multiple cells (bottom panel) in the microfluidic channels of the experimental setups.

$$P_{\text{cell}} = -\xi_{\text{ext}} \pi R^2 \bar{v}_{\text{ext}}, \quad (\text{A.6})$$

and using A.2, the fluid flow induced by the migrating cell is given by

$$\bar{v}_{\text{ext}} = \frac{\xi}{\xi + \xi_{\text{ext}}} U, \quad (\text{A.7})$$

such that the fluid drag coefficient $\alpha_{\text{D}} = -P_{\text{cell}}/U$ (see Section 3.2.2) is defined as

$$\alpha_{\text{D}} = \xi_{\text{ext}} \pi R^2 \frac{\xi}{\xi + \xi_{\text{ext}}} \quad (\text{A.8})$$

for this case. For several cells migrating simultaneously in a microfluidic channel, see Figure A.1 (bottom), the pressure difference on cell i is given by

$$P_{i,\text{cell}} = \xi \pi R^2 (\bar{v}_{\text{ext}} - U_i), \quad (\text{A.9})$$

assuming that the cell flow resistance ξ takes the same value for all cells, and Equation A.7 modifies to

$$\bar{v}_{\text{ext}} = \frac{\xi}{N\xi + \xi_{\text{ext}}} \sum_{i=1}^N U_i, \quad (\text{A.10})$$

with N the number of cells. In Section 3.2.3, we use this relation to verify our estimate for the cell flow resistance ξ . Using that $U_i = U_{0,i} + P_{i,\text{cell}}/\chi$ (see Equation 3.30 in Section 3.2.2) and

Equation A.9, we obtain the following equation relating the velocities U_i , $U_{0,i}$ and \bar{v}_{ext}

$$\left(1 + \frac{\xi\pi R^2}{\chi}\right) \frac{U_i}{U_{0,i}} = 1 + \frac{\xi\pi R^2}{\chi} \frac{\bar{v}_{\text{ext}}}{U_{0,i}}. \quad (\text{A.11})$$

Analysis of the distribution of cell velocities indicates that the cells can be grouped into polarized self-propelled cells moving rapidly, and unpolarized slow cells (see Figure 3.11). For the rapidly moving cells, which were analyzed in the migration experiments, the intrinsic velocity U_0 is large compared to the velocity of the surrounding medium \bar{v}_{ext} . Furthermore, our results indicate that for large and intermediate friction conditions, the cell flow resistance is small compared to the effective friction $\xi\pi R^2/\chi < 1$. We therefore neglect the second term on the right hand side of Equation A.11, obtaining that

$$U_i = \frac{\chi}{\chi + \xi\pi R^2} U_{i,0} \quad (\text{A.12})$$

for polarized cells. Then the expression for the pressure on these cells simplifies to

$$P_{i,\text{cell}} = -\xi\pi R^2 U_i, \quad (\text{A.13})$$

and the fluid drag coefficient is approximated by

$$\alpha_{\text{D}} = \xi\pi R^2. \quad (\text{A.14})$$

Thus, for rapid, self-propelled cells the fluid drag coefficient is set mainly by the effective fluid flow resistance ξ .

Appendix B

Internal friction during Walker cell migration

The nucleus has been found to play an important role in cell migration mechanics in confined environments in different cellular systems [54, 67]. In this appendix, we investigate a possible dissipating effect due to the presence of the nucleus during cell migration in blebbing Walker cells. As stated in Equation 3.4, for the calculations presented in Chapter 3, we assume that the internal shear stresses acting on the cortex from the cytoplasmic side are negligible compared to the effect of friction with the walls of the confining microfluidic channel. However, such shear stresses may arise from molecular coupling between nucleoskeletal and cortical elements along the contact surface of the cortex with the nuclear envelope (see Figure B.1 A). Here, we discuss the effect of introducing an internal frictional force term resisting cortical flows into our theoretical description. For this case, Equation 3.5 modifies to

$$\partial_s t^s_s = (\alpha_{\text{ext}} + \alpha_{\text{int}})v^s + \alpha_{\text{ext}}U, \quad (\text{B.1})$$

with α_{int} and α_{ext} denoting the intracellular and extracellular friction coefficients respectively. For simplicity, we assume here that the internal friction acts only in the cylindrical cell region, where the cell is confined, and the cortex is pressed against the nucleus, and we do not treat the frontal cell part differently, where the cylindrical cell region extends beyond the nucleus (see Figure B.1 A and D). The solutions for the shape and flow in the cell pole regions thus remain unchanged from the expressions given in Section 3.2.2, and the flow in the cylindrical cell region modifies to

$$v^s = C_1 \exp\left(\frac{x^{(\text{m})}}{l}\right) + C_2 \exp\left(-\frac{x^{(\text{m})}}{l}\right) - \left(\frac{l}{l_{\text{ext}}}\right)^2 U - \frac{\zeta^{(\text{r})} - \zeta^{(\text{f})}}{(\alpha_{\text{int}} + \alpha_{\text{ext}})L}, \quad (\text{B.2})$$

for the piecewise linear profile of active tension 3.14, where the hydrodynamic lengths have been modified to $l = \sqrt{\eta/(\alpha_{\text{int}} + \alpha_{\text{ext}})}$ and $l_{\text{ext}} = \sqrt{\eta/\alpha_{\text{ext}}}$. As a result of the frictional coupling, the cortex exerts a flow-dependent force acting on the nucleus, which is balanced by the difference of the intracellular fluid pressure between the rear and front cell regions. Accordingly, the force

Parameter	Value
Viscosity η_{2D}	$27 \pm 1 \times 10^{-4} \text{ Pa s m}$
Cell flow resistance ξ	$3.5 \pm 0.3 \times 10^{15} \text{ Pa s m}^{-3}$
Myosin scaling factor $\zeta^{(0)}$	$53 \pm 1 \text{ pN } \mu\text{m}^{-1}$
Internal friction α_{int}	$5.2 \times 10^{-8} \pm 22 \text{ Pa s m}^{-1}$

Table B.1: Fitted parameter estimates for the description with internal friction.

balance on the nucleus reads

$$\left(P_{\text{int}}^{(r)} - P_{\text{int}}^{(f)}\right) \pi R^2 = -\alpha_{\text{int}} 2\pi R \int_0^L dx \quad v^s, \quad (\text{B.3})$$

replacing Equation 3.29 in Section 3.2.2. Deriving the equations for the cell velocity and the cortical flow profiles using the myosin intensity data as before, we repeated the fitting procedure detailed in Section 3.2.3 with the modified expressions. The parameter estimates obtained are summarized in Table B.1. Importantly, we recover that the internal friction is small compared to the external friction ($\alpha_{\text{int}}/\alpha_{\text{ext}} \ll 1$ for small, intermediate and large friction conditions), consistent with our initial assumption stated in Chapter 3.

Some experimental observations further suggest that nuclear properties do not have a large influence on migration mechanics of Walker cells in microfluidic channels. For example, nuclear size does not correlate with cell migration velocity in both large and intermediate friction conditions (Figure B.1 A - B). Furthermore, blebbing Walker cells were found to have very low expression levels of the nucleoskeletal components Lamin A and Lamin C (see [13]), which have been associated with nuclear stiffness. We also occasionally noted the presence of nuclear blebs [44] during migration, indicating structural weaknesses in the nuclear lamina (see Figure B.1 D). These findings suggest that blebbing Walker cells may have particularly soft nuclei, which do not exert a limiting effect on confined cell migration.

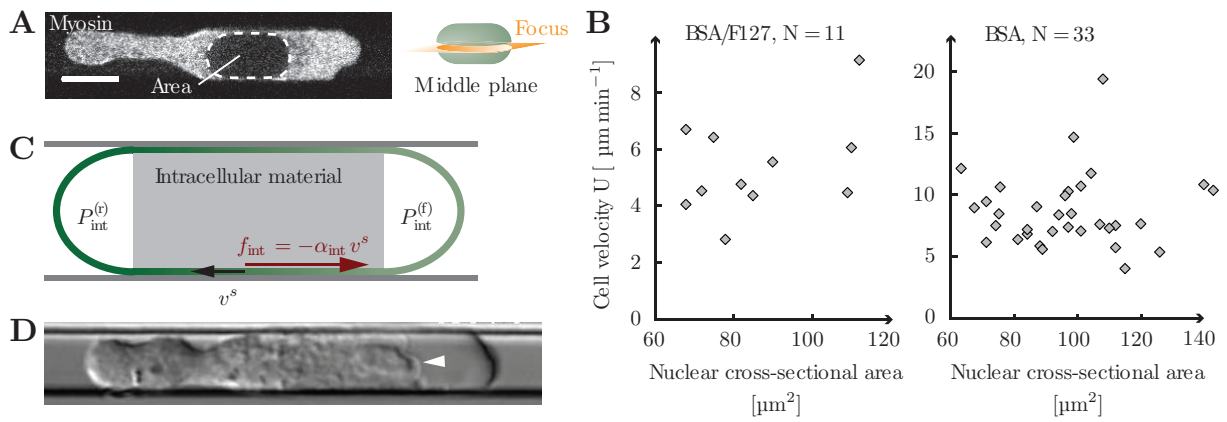


Figure B.1: Role of the nucleus and internal friction during Walker cell migration.

A. - B. The size of the nucleus does not correlate with cell velocity in large (BSA) or intermediate (F127/BSA) friction conditions. Confocal middle plane images of migrating Walker cells with fluorescently labeled myosin II (MRLC-GFP) were used to determine the cross-sectional area of the nucleus (panel A). Scale bar: $10\ \mu\text{m}$. **C.** Schematic representation of the description with internal friction. An internal frictional force density f_{int} acts on the cortex from the intracellular side in the cylindrically confined cell region. **D.** Bright-field image of a migrating Walker cell with a blebbing nucleus (highlighted by white arrow). Nuclear blebs suggest that the nucleoskeletal lamin network has a large mesh-size and/or structural weaknesses. Panels A - C were published in similar form in [13].

Appendix C

Image analysis and quantification

In this appendix we outline the procedures for analyzing microscopy images to extract the observables of actomyosin mechanics, as applied in Chapter 3. The image analysis for Chapter 4 was done by A.-C. Reymann, see [109] for details. From our experimental collaborators, we received time lapse fluorescence microscopy images of Walker cells migrating in microfluidic channels, with a time resolution of 2 s, with labeled components of the actomyosin cytoskeleton (see Figure 3.9 C for an example). We extracted the average profiles of myosin fluorescence intensity along the migration axis for different experimental conditions, to obtain an estimate for the distribution of active tensions within the cortical layer. Furthermore, we estimated the profiles of cortical flow. The obtained datasets consist of average values taken over different cells, different points in time, and different points in the y -direction along the cells, by which we assume the measured profiles to be stationary and axisymmetric, consistent with the assumptions of the theoretical description. To average over cells of different lengths, we divided the data into 50 bins along the axis of migration for the intensity quantification, and 33 bins for the PIV analysis. We registered the movies using the MultiStackReg plugin in Fiji, and applied a Gaussian blur filter with height 3 and width 0.9 to all images prior to analysis, in order to reduce noise. For details on the experimental setup, cell cultures and reagents, see [13]. Note that the microfluidic channels had a rectangular cross-section ($6 \times 10 \mu\text{m}^2$) to enable confocal microscopy, but were assumed to be cylindrical with radius $R = \sqrt{60 \mu\text{m}^2/\pi} \approx 4.4 \mu\text{m}$ for the theoretical description.

C.1 Estimation of cortical myosin intensities

For each friction condition, we estimated the average relative fluorescence intensity of cortical myosin in migrating Walker cells. We subtracted the background cytoplasmic signal from cortex plane images, using images from the middle section of the cells. All intensities were normalized to the average intensity in a region devoid of myosin spots in the front of the cell (see Figure C.1).

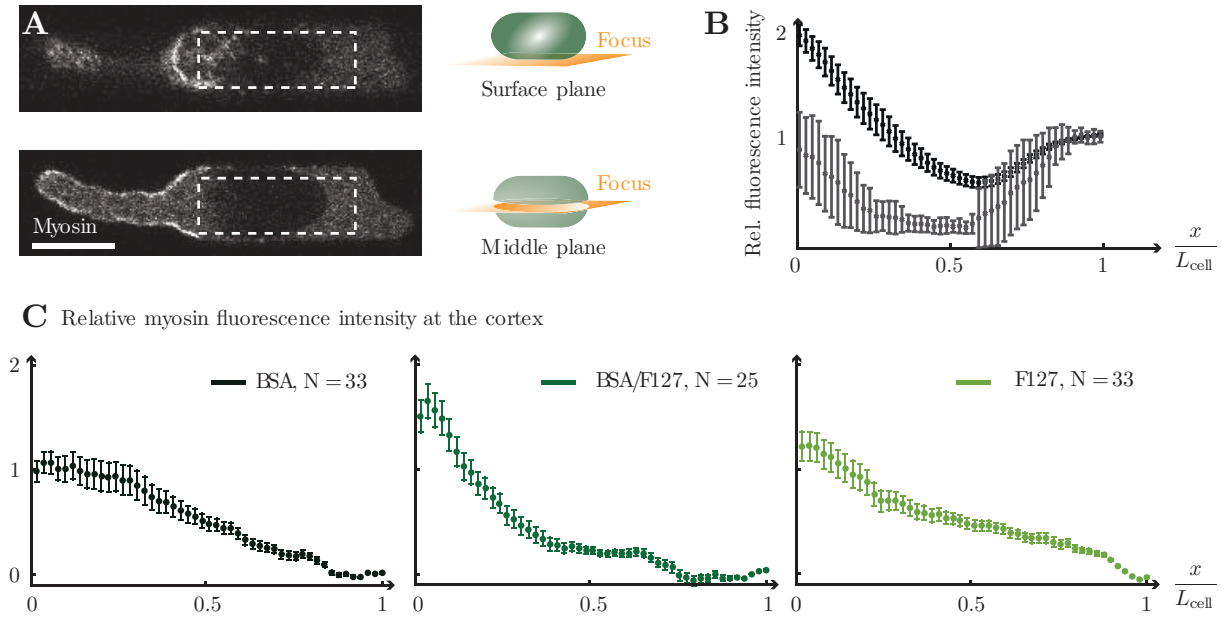


Figure C.1: Quantification of cortical myosin fluorescence intensity in migrating Walker cells. **A.** Confocal images of Walker cells with fluorescently labeled myosin II (MRLC-GFP) from the cortex and middle focal planes. Scale bar: 10 μm . White rectangles highlight the region of interest chosen for the quantification of myosin fluorescence intensity profiles. ROI chosen for the analysis of myosin II intensity. **B.** The cortical profile was obtained by subtracting the intensity signal of the middle plane image (gray) from the cortex plane image (black) to remove the cytoplasmic background. Both profiles are normalized to the average fluorescence intensity within a region at the cell front containing no myosin foci. The data here correspond to the dataset from the BSA condition. **C.** Relative cortical myosin fluorescence intensity profiles used for estimating the active tension fields in the three different friction conditions (see Section 3.2.3). All error bars refer to standard errors of the mean. Panels were published in similar form in [13].

C.2 Estimation of cortical flows

Particle image velocimetry is a method to quantify flow velocities based on cross-correlation analysis of images taken at subsequent time points, relying on visually distinct structures such as tracer particles, to move with the flow of material monitored [2]. To estimate the magnitude of cortical flows during Walker cell migration, we relied on the presence of stationary myosin foci forming in these cells to function as effective tracer particles. We manually selected a region of interest for analysis from time-averaged images such as Figure 3.5 A, spanning the cell from the rear to the front, but excluding the contracted tail structure. The algorithm we used was introduced and described in more detail in [86]. The cytoplasmic signal in the confocal images of the cortical plane of migrating Walker cells results in static noisy background (i. e. due to the shadow of the nucleus, see Figure 3.9 C), which leads to a systematic underestimation of cortical flow velocities by the PIV algorithm. To correct for this, we generated series of artificial test images, with random patterns of blurred spots, which were shifted in front of middle- plane images of the analyzed cells. We adjusted the intensity and size of the spots to match real myosin foci, and advanced the pattern at a rate of 3 px per frame, in the range of the observed cortical flow. Performing PIV on these artificial cortical flows with known velocity allowed us to estimate the factor correcting for the bias; we found $v_{\text{corr}} = 1.17v_{\text{PIV}}$.

In performing the averaging over time, height and cells to obtain the final profiles, we filtered the data based on the following criteria on the sample size, to account for differences in the quality of images from different cells and cell regions, as well as for variations in the size of cells, and the length of movies. For each cell, a data point for the profile along the cell migration axis was included, if the PIV algorithm generated $n > 300$ points over time and over the height of the cell for this location. Furthermore, in averaging over cells, we computed the sample size median for each bin along the profile for each friction condition, and discarded data points coming from smaller samples. This procedure allowed the precise estimation of flow velocities in the rear part of the cell, where stationary cortical patterns were sufficiently distinct to be traced by the PIV algorithm. The analysis was performed on a total of $N = 33$, $N = 25$ and $N = 33$ cells for the BSA, F127/BSA and F127 conditions respectively.

C.3 Software and tools

For the preprocessing of microscopy images and the selection of regions of interest, we used ImageJ (Fiji). Schematics and figures were assembled in Adobe Illustrator. Data analysis, fitting and visualization was performed with Matlab (MathWorks, 2013 - 2014) and Mathematica (Wolfram Research, 2013 - 2015), which was also used for algebraic computations.

Bibliography

- [1] M. Abercrombie. The crawling movement of metazoan cells. *Proceedings of the royal society of London B*, 207(1167):129–147, 1980.
- [2] R. J. Adrian. Particle-image techniques for experimental fluid mechanics. *Annual Review of Fluid Mechanics*, 23:261–304, 1991.
- [3] B. Alberts, A. Johnson, J. Lewis, D. Morgan, M. Raff, K. Roberts, and P. Walter. *Molecular Biology of the Cell*. Garland Science, 6 edition, 2014.
- [4] D. G. Albertson. Formation of the first cleavage spindle in nematode embryos. *Developmental biology*, 101(1):61–72, 1984.
- [5] J. L. Barbosa and M. do Carmo. Stability of hypersurfaces with constant mean curvature. In *Manfredo P. do Carmo–Selected Papers*, pages 221–235. Springer, 2012.
- [6] E. L. Barnhart, K.-C. Lee, K. Keren, A. Mogilner, and J. A. Theriot. An adhesion-dependent switch between mechanisms that determine motile cell shape. *PLoS biology*, 9(5):e1001059, 2011.
- [7] M. Behrndt, G. Salbreux, P. Campinho, R. Hauschild, F. Oswald, J. Roensch, S. W. Grill, and C.-P. Heisenberg. Forces driving epithelial spreading in zebrafish gastrulation. *Science (New York, N.Y.)*, 338(6104):257–60, 2012.
- [8] W. M. Bement. Actomyosin rings: The riddle of the sphincter. *Current Biology*, 12(1):14–16, 2002.
- [9] P. M. Bendix, G. H. Koenderink, D. Cuvelier, Z. Dogic, B. N. Koeleman, W. M. Briehner, C. M. Field, L. Mahadevan, and D. A. Weitz. A quantitative analysis of contractility in active cytoskeletal protein networks. *Biophysical journal*, 94(8):3126–3136, 2008.
- [10] K. A. Beningo, M. Dembo, I. Kaverina, J. V. Small, and Y. L. Wang. Nascent focal adhesions are responsible for the generation of strong propulsive forces in migrating fibroblasts. *Journal of Cell Biology*, 153(4):881–887, 2001.
- [11] M. Bergert. *Mechanics of protrusion formation and bleb-based migration in animal cells*. PhD thesis, Technical University Dresden, 11 2012.

- [12] M. Bergert, S. D. Chandradoss, R. A. Desai, and E. Paluch. Cell mechanics control rapid transitions between blebs and lamellipodia during migration. *Proceedings of the National Academy of Sciences*, 109(36):14434–14439, 2012.
- [13] M. Bergert, A. Erzberger, R. A. Desai, I. M. Aspalter, A. C. Oates, G. Charras, G. Salbreux, and E. K. Paluch. Force transmission during adhesion-independent migration. *Nature Cell Biology*, 17(4):524–529, 2015.
- [14] H. Berthoumieux, J. L. Maître, C. P. Heisenberg, E. K. Paluch, F. Jülicher, and G. Salbreux. Active elastic thin shell theory for cellular deformations. *New Journal of Physics*, 16:065005, 2014.
- [15] H. Blaser, M. Reichman-Fried, I. Castanon, K. Dumstrei, F. L. Marlow, K. Kawakami, L. Solnica-Krezel, C.-P. Heisenberg, and E. Raz. Migration of zebrafish primordial germ cells: a role for myosin contraction and cytoplasmic flow. *Developmental cell*, 11(5):613–27, 2006.
- [16] R. Boehme. Actin filament alignment by compressive cortical flow. Master’s thesis, Technical University Dresden, 2013.
- [17] M. Bovellan, Y. Romeo, M. Biro, A. Boden, P. Chugh, A. Yonis, M. Vaghela, M. Fritzsche, D. Moulding, R. Thorogate, A. Jégou, A. J. Thrasher, G. Romet-Lemonne, P. P. Roux, E. K. Paluch, and G. Charras. Cellular control of cortical actin nucleation. *Current Biology*, 24(14):1628–1635, 2014.
- [18] D. Bray and J. G. White. Cortical flow in animal cells. *Science (New York, N.Y.)*, 239(4842):883–888, 1988.
- [19] N. A. Bulgakova and E. Knust. The Crumbs complex: from epithelial-cell polarity to retinal degeneration. *Journal of cell science*, 122(Pt 15):2587–2596, 2009.
- [20] S. Byun, S. Son, D. Amodei, N. Cermak, J. Shaw, J. H. Kang, V. C. Hecht, M. M. Winslow, T. Jacks, P. Mallick, and S. R. Manalis. Characterizing deformability and surface friction of cancer cells. *Proceedings of the National Academy of Sciences of the United States of America*, 110(19):7580–7585, 2013.
- [21] A. C. Callan-Jones and R. Voituriez. Active gel model of amoeboid cell motility. *New Journal of Physics*, 15(2):025022, 2013.
- [22] R. Capovilla and J. Guven. Stresses in lipid membranes. *Journal of Physics A: Mathematical and General*, 35:6233–6247, 2002.
- [23] P. M. Chaikin and T. C. Lubensky. *Principles of condensed matter physics*, volume 1. Cambridge Univ Press, 2000.
- [24] G. Charras and E. Paluch. Blebs lead the way: how to migrate without lamellipodia. *Nature reviews. Molecular cell biology*, 9(9):730–736, 2008.

- [25] C. K. Choi, M. Vicente-Manzanares, J. Zareno, L. A. Whitmore, A. Mogilner, and A. R. Horwitz. Actin and alpha-actinin orchestrate the assembly and maturation of nascent adhesions in a myosin II motor-independent manner. *Nature cell biology*, 10(9):1039–1050, 2008.
- [26] A. G. Clark, K. Dierkes, and E. K. Paluch. Monitoring actin cortex thickness in live cells. *Biophysical journal*, 105(3):570–580, 2013.
- [27] A. G. Clark, A. L. Miller, E. Vaughan, H. Y. E. Yu, R. Penkert, and W. M. Bement. Integration of Single and Multicellular Wound Responses. *Current Biology*, 19(16):1389–1395, 2009.
- [28] C. R. Cowan and A. A. Hyman. Asymmetric cell division in *C. elegans*: cortical polarity and spindle positioning. *Annual review of cell and developmental biology*, 20:427–453, 2004.
- [29] G. Danuser, J. Allard, and A. Mogilner. Mathematical modeling of eukaryotic cell migration: insights beyond experiments. *Annual review of cell and developmental biology*, 29:501–28, 2013.
- [30] N. Dasanayake, P. Michalski, and A. Carlsson. General Mechanism of Actomyosin Contractility. *Physical Review Letters*, 107(11):118101, 2011.
- [31] P.-G. de Gennes, F. Brochard-Wyart, and D. Quéré. *Capillarity and wetting phenomena: drops, bubbles, pearls, waves*. Springer Science & Business Media, 2013.
- [32] P.-G. de Gennes and J. Prost. *The physics of liquid crystals*. 83. Oxford university press, 2 edition, 1995.
- [33] F. Del Bene, A. M. Wehman, B. A. Link, and H. Baier. Regulation of neurogenesis by interkinetic nuclear migration through an apical-basal notch gradient. *Cell*, 134(6):1055–1065, 2008.
- [34] M. Dembo and Y. L. Wang. Stresses at the cell-to-substrate interface during locomotion of fibroblasts. *Biophysical journal*, 76(4):2307–2316, 1999.
- [35] R. d’Inverno. *Introducing Einstein’s Relativity*. Oxford University Press, USA, 1992.
- [36] M. T. Downton and H. Stark. Simulation of a model microswimmer. *Journal of physics. Condensed matter : an Institute of Physics journal*, 21(20):204101, 2009.
- [37] D. J. Durian. Foam mechanics at the bubble scale. *Physical review letters*, 75(26):4780–4783, 1995.
- [38] J. Eggers and E. Villermaux. Physics of liquid jets. *Reports on Progress in Physics*, 71(3):036601, 2008.
- [39] F. Eghiaian, A. Rigato, and S. Scheuring. Structural, Mechanical, and Dynamical Variability of the Actin Cortex in Living Cells. *Biophysical Journal*, 108(6):1330–1340, 2015.

- [40] A. Fedier, P. Eggli, and H. U. Keller. Redistribution of surface-bound Con A is quantitatively related to the movement of cells developing polarity. *Cell Motility and the Cytoskeleton*, 44(1):44–57, 1999.
- [41] D. A. Fletcher and R. D. Mullins. Cell mechanics and the cytoskeleton. *Nature*, 463(7280):485–492, 2010.
- [42] P. Friedl, J. Locker, E. Sahai, and J. E. Segall. Classifying collective cancer cell invasion. *Nature Cell Biology*, 14(8):777–783, 2012.
- [43] E. Frixione. Recurring views on the structure and function of the cytoskeleton: A 300-year epic. *Cell Motility and the Cytoskeleton*, 46(2):73–94, 2000.
- [44] C. M. Funkhouser, R. Sknepnek, T. Shimi, A. E. Goldman, R. D. Goldman, and M. Olvera de la Cruz. Mechanical model of blebbing in nuclear lamin meshworks. *Proceedings of the National Academy of Sciences of the United States of America*, 110(9):3248–3253, 2013.
- [45] S. Fürthauer. *Active chiral processes in soft biological matter*. PhD thesis, Technical University Dresden, 5 2012.
- [46] M. L. Gardel, I. C. Schneider, Y. Aratyn-Schaus, and C. M. Waterman. Mechanical integration of actin and adhesion dynamics in cell migration. *Annual review of cell and developmental biology*, 26:315, 2010.
- [47] M. W. Goldberg, J. Fiserova, I. Huttenlauch, and R. Stick. A new model for nuclear lamina organization. *Biochemical Society transactions*, 36(Pt 6):1339–1343, 2008.
- [48] M. Götz and W. B. Huttner. The cell biology of neurogenesis. *Nature reviews. Molecular cell biology*, 6(10):777–788, 2005.
- [49] R. A. Green, E. Paluch, and K. Oegema. Cytokinesis in Animal Cells. *Annual review of cell and developmental biology*, 28:29–58, 2012.
- [50] S. W. Grill, P. Gönczy, E. H. Stelzer, and A. A. Hyman. Polarity controls forces governing asymmetric spindle positioning in the *Caenorhabditis elegans* embryo. *Nature*, 409(6820):630–633, 2001.
- [51] J. Guck, F. Lautenschläger, S. Paschke, and M. Beil. Critical review: cellular mechanobiology and amoeboid migration. *Integrative biology : quantitative biosciences from nano to macro*, 2(11-12):575–583, 2010.
- [52] S. L. Gupton and C. M. Waterman-Storer. Spatiotemporal Feedback between Actomyosin and Focal-Adhesion Systems Optimizes Rapid Cell Migration. *Cell*, 125(7):1361–1374, 2006.
- [53] J. Guven. Laplace pressure as a surface stress in fluid vesicles. *Journal of Physics A: Mathematical and General*, 39(14):3771–3785, 2006.

- [54] T. Harada, J. Swift, J. Irianto, J.-W. Shin, K. R. Spinler, A. Athirasala, R. Diegmiller, P. C. D. P. Dingal, I. L. Ivanovska, and D. E. Discher. Nuclear lamin stiffness is a barrier to 3D migration, but softness can limit survival. *The Journal of cell biology*, 204(5):669–682, 2014.
- [55] T. Hiraiwa and G. Salbreux. Role of turn-over in active stress generation in a filament network. *arXiv preprint arXiv:1507.06182*, 2015.
- [56] S. N. Hird and J. G. White. Cortical and cytoplasmic flow polarity in early embryonic cells of *Caenorhabditis elegans*. *Journal of Cell Biology*, 121(6):1343–1355, 1993.
- [57] J. Howard. Quantitative cell biology: the essential role of theory. *Molecular biology of the cell*, 25:3438–3440, 2014.
- [58] R. Ishikawa, T. Sakamoto, T. Ando, S. Higashi-Fujime, and K. Kohama. Polarized actin bundles formed by human fascin-1: Their sliding and disassembly on myosin II and myosin V in vitro. *Journal of Neurochemistry*, 87(3):676–685, 2003.
- [59] J.-F. Joanny, F. Jülicher, K. Kruse, and J. Prost. Hydrodynamic theory for multi-component active polar gels. *New Journal of Physics*, 9:422, 2007.
- [60] M. H. Jorrich, W. Shih, and S. Yamada. Myosin IIA deficient cells migrate efficiently despite reduced traction forces at cell periphery. *Biology open*, 2(4):368–372, 2013.
- [61] F. Jülicher. Active fluids and gels. In *New trends in the physics and mechanics of biological systems: Lecture notes of the Lew Houches summer school*, volume 92, chapter 4, pages 97–122. Oxford Scholarship Online, 2011.
- [62] F. Jülicher, K. Kruse, J. Prost, and J.-F. Joanny. Active behavior of the Cytoskeleton. *Physics Reports*, 449(1-3):3–28, 2007.
- [63] P. Kanchanawong, G. Shtengel, A. M. Pasapera, E. B. Ramko, M. W. Davidson, H. F. Hess, and C. M. Waterman. Nanoscale architecture of integrin-based cell adhesions. *Nature*, 468(7323):580–584, 2010.
- [64] T. Katayama, M. Watanabe, H. Tanaka, M. Hino, T. Miyakawa, T. Ohki, L.-H. Ye, C. Xie, S. Yoshiyama, A. Nakamura, R. Ishikawa, M. Tanokura, K. Oiwa, and K. Kohama. Stimulatory effects of arachidonic acid on myosin ATPase activity and contraction of smooth muscle via myosin motor domain. *American journal of physiology. Heart and circulatory physiology*, 298(2):505–514, 2010.
- [65] F. C. Keber, E. Loiseau, T. Sanchez, S. J. DeCamp, L. Giomi, M. J. Bowick, M. C. Marchetti, Z. Dogic, and A. R. Bausch. Topology and dynamics of active nematic vesicles. *Science (New York, N.Y.)*, 345(6201):1135–1139, 2014.
- [66] K. Keren, Z. Pincus, G. M. Allen, E. L. Barnhart, G. Marriott, A. Mogilner, and J. A. Theriot. Mechanism of shape determination in motile cells. *Nature*, 453(7194):475–480, 2008.

- [67] S. B. Khatau, R. J. Bloom, S. Bajpai, D. Razafsky, S. Zang, A. Giri, P.-H. Wu, J. Marchand, A. Celedon, C. M. Hale, S. X. Sun, D. Hodzic, and D. Wirtz. The distinct roles of the nucleus and nucleus-cytoskeleton connections in three-dimensional cell migration. *Scientific reports*, 2:488, 2012.
- [68] C. B. Kimmel, W. W. Ballard, S. R. Kimmel, B. Ullmann, and T. F. Schilling. Stages of embryonic development of the zebrafish. *Developmental dynamics : an official publication of the American Association of Anatomists*, 203(3):253–310, 1995.
- [69] K. Kruse, J.-F. Joanny, F. Jülicher, and J. Prost. Contractility and retrograde flow in lamellipodium motion. *Physical biology*, 3(2):130–137, 2006.
- [70] K. Kruse, J.-F. Joanny, F. Jülicher, J. Prost, and K. Sekimoto. Generic theory of active polar gels: a paradigm for cytoskeletal dynamics. *The European physical journal. E, Soft matter*, 16(1):5–16, 2005.
- [71] A. Kumar, A. Maitra, M. Sumit, S. Ramaswamy, and G. V. Shivashankar. Actomyosin contractility rotates the cell nucleus. *Scientific reports*, 4:3781, 2014.
- [72] S. Kuriyama and R. Mayor. Molecular analysis of neural crest migration. *Philosophical transactions of the Royal Society of London. Series B, Biological sciences*, 363(1495):1349–1362, 2008.
- [73] T. Lämmermann, B. L. Bader, S. J. Monkley, T. Worbs, R. Wedlich-Söldner, K. Hirsch, M. Keller, R. Förster, D. R. Critchley, R. Fässler, and M. Sixt. Rapid leukocyte migration by integrin-independent flowing and squeezing. *Nature*, 453(7191):51–55, 2008.
- [74] T. Lämmermann and M. Sixt. Mechanical modes of 'amoeboid' cell migration. *Current Opinion in Cell Biology*, 21(5):636–644, 2009.
- [75] L. D. Landau and E. M. Lifshitz. *Course of Theoretical Physics: Fluid mechanics*, volume 6. Butterworth-Heinemann, 2 edition, 1987. translated from Russian by JB Sykes and WH Reid.
- [76] E. Lauga and T. R. Powers. The hydrodynamics of swimming microorganisms. *Reports on Progress in Physics*, 72(9):096601, 2009.
- [77] F. Lautenschläger, S. Paschke, S. Schinkinger, A. Bruel, M. Beil, and J. Guck. The regulatory role of cell mechanics for migration of differentiating myeloid cells. *Proceedings of the National Academy of Sciences of the United States of America*, 106(37):15696–701, Sept. 2009.
- [78] H. O. Lee and C. Norden. Mechanisms controlling arrangements and movements of nuclei in pseudostratified epithelia. *Trends in cell biology*, pages 1–10, 2012.
- [79] W. R. Legant, J. S. Miller, B. L. Blakely, D. M. Cohen, G. M. Genin, and C. S. Chen. Measurement of mechanical tractions exerted by cells in three-dimensional matrices. *Nature methods*, 7(12):969–971, 2010.

- [80] L. Leung, A. V. Klopfer, S. W. Grill, W. A. Harris, and C. Norden. Apical migration of nuclei during G2 is a prerequisite for all nuclear motion in zebrafish neuroepithelia. *Development*, 138(22):5003–5013, 2011.
- [81] X. Liu, M.-S. Hong, S. Shu, S. Yu, and E. D. Korn. Regulation of the filament structure and assembly of *Acanthamoeba* myosin II by phosphorylation of serines in the heavy-chain nonhelical tailpiece. *Proceedings of the National Academy of Sciences of the United States of America*, 110:E33–40, 2012.
- [82] Y.-J. Liu, M. Le Berre, F. Lautenschläger, P. Maiuri, A. Callan-Jones, M. Heuzé, T. Takaki, R. Voituriez, and M. Piel. Confinement and Low Adhesion Induce Fast Amoeboid Migration of Slow Mesenchymal. *Cell*, 160:659–672, 2015.
- [83] T. B. Liverpool, M. C. Marchetti, J.-F. Joanny, and J. Prost. Mechanical response of active gels. *EPL (Europhysics Letters)*, 85(1):18007, 2009.
- [84] G. W. G. Luxton, E. R. Gomes, E. S. Folker, E. Vintinner, and G. G. Gundersen. Linear arrays of nuclear envelope proteins harness retrograde actin flow for nuclear movement. *Science (New York, N.Y.)*, 329(5994):956–959, 2010.
- [85] G. W. G. Luxton, E. R. Gomes, E. S. Folker, H. J. Worman, and G. G. Gundersen. TAN lines: a novel nuclear envelope structure involved in nuclear positioning. *Nucleus (Austin, Tex.)*, 2(3):173–181, 2011.
- [86] M. Mayer, M. Depken, J. S. Bois, F. Jülicher, and S. W. Grill. Anisotropies in cortical tension reveal the physical basis of polarizing cortical flows. *Nature*, 467(7315):617–621, 2010.
- [87] E. J. Meyer, A. Ikmi, and M. C. Gibson. Interkinetic nuclear migration is a broadly conserved feature of cell division in pseudostratified epithelia. *Current biology : CB*, 21(6):485–491, 2011.
- [88] E. Moeendarbary, L. Valon, M. Fritzsche, A. R. Harris, D. A. Moulding, A. J. Thrasher, E. Stride, L. Mahadevan, and G. T. Charras. The cytoplasm of living cells behaves as a poroelastic material. *Nature materials*, 12(1):1–9, 2013.
- [89] A. Mogilner. Mathematics of cell motility: have we got its number? *Journal of mathematical biology*, 58(1-2):105–134, 2009.
- [90] A. Mogilner and G. Oster. Cell motility driven by actin polymerization. *Biophysical journal*, 71(6):3030–3045, 1996.
- [91] K. Mohan, P. A. Iglesias, and D. N. Robinson. Separation anxiety: stress, tension and cytokinesis. *Experimental cell research*, 318(12):1428–1434, 2012.
- [92] M. Mori, N. Monnier, N. Daigle, M. Bathe, J. Ellenberg, and P. Lénárt. Intracellular transport by an anchored homogeneously contracting F-actin meshwork. *Current Biology*, 21(7):606–611, 2011.

- [93] S. Mukhina, Y.-l. Wang, and M. Murata-Hori. Alpha-Actinin Is Required for Tightly Regulated Remodeling of the Actin Cortical Network during Cytokinesis. *Developmental Cell*, 13(4):554–565, 2007.
- [94] S. Munevar, Y.-l. Wang, and M. Dembo. Traction Force Microscopy of Migrating Normal and H-ras Transformed 3T3 Fibroblasts. *Biophysical Journal*, 80(4):1744–1757, 2001.
- [95] M. Murrell, P. W. Oakes, M. Lenz, and M. L. Gardel. Forcing cells into shape: the mechanics of actomyosin contractility. *Nature Reviews Molecular Cell Biology*, (July), 2015.
- [96] A. Nagy, Y. Takagi, N. Billington, S. A. Sun, D. K. T. Hong, E. Homsher, A. Wang, and J. R. Sellers. Kinetic characterization of nonmuscle myosin IIB at the single molecule level. *Journal of Biological Chemistry*, 288(1):709–722, 2013.
- [97] C. Norden, S. Young, B. A. Link, and W. A. Harris. Actomyosin is the main driver of interkinetic nuclear migration in the retina. *Cell*, 138(6):1195–1208, 2009.
- [98] M. Norstrom and M. L. Gardel. Shear thickening of F-actin networks crosslinked with non-muscle myosin IIB. *Soft Matter*, 7(7):3228, 2011.
- [99] L. Onsager. Reciprocal relations in irreversible processes. i. *Physical Review*, 37(4):405, 1931.
- [100] J. T. Parsons, A. R. Horwitz, and M. A. Schwartz. Cell adhesion: integrating cytoskeletal dynamics and cellular tension. *Nature reviews. Molecular cell biology*, 11(9):633–643, 2010.
- [101] R. J. Pelham and F. Chang. Actin dynamics in the contractile ring during cytokinesis in fission yeast. *Nature*, 419(6902):82–86, 2002.
- [102] R. Poincloux, O. Collin, F. Lizárraga, M. Romao, M. Debray, M. Piel, and P. Chavrier. Contractility of the cell rear drives invasion of breast tumor cells in 3D Matrigel. *Proceedings of the National Academy of Sciences of the United States of America*, 108(5):1943–1948, 2011.
- [103] P. Pereira, M.-P. Valignat, J. Bico, and O. Théodoly. Single cell rheometry with a microfluidic constriction: Quantitative control of friction and fluid leaks between cell and channel walls. *Biomicrofluidics*, 7(2):024111, 2013.
- [104] G. Pretzler. A new method for numerical Abel-inversion. *Zeitschrift für Naturforschung. A, A Journal of physical sciences*, 46(7):639–641, 1991.
- [105] J. Prost, F. Jülicher, and J.-F. Joanny. Active gel physics. *Nature physics*, 11(February):111–117, 2015.
- [106] E. M. Purcell. Life at low Reynolds number. *American Journal of Physics*, 45(1):3–11, 1977.

- [107] R. Rappaport and B. N. Rappaport. Establishment of cleavage furrows by the mitotic spindle. *The Journal of experimental zoology*, 189(2):189–196, 1974.
- [108] J. Renkawitz and M. Sixt. Mechanisms of force generation and force transmission during interstitial leukocyte migration. *EMBO reports*, 11(10):744–750, 2010.
- [109] A.-C. Reymann, F. Staniscia, A. Erzberger, R. Boehme, G. Salbreux, and S. W. Grill. Cortical flow aligns actin filaments to initiate furrowing, in preparation.
- [110] M. W. Rochlin, M. E. Dailey, and P. C. Bridgman. Polymerizing microtubules activate site-directed F-actin assembly in nerve growth cones. *Molecular biology of the cell*, 10(7):2309–2327, 1999.
- [111] V. Ruprecht, S. Wieser, A. Callan-Jones, M. Smutny, H. Morita, K. Sako, V. Barone, M. Ritsch-Marte, M. Sixt, R. Voituriez, and C.-P. Heisenberg. Cortical Contractility Triggers a Stochastic Switch to Fast Amoeboid Cell Motility. *Cell*, 160(4):673–685, 2015.
- [112] G. Salbreux, G. Charras, and E. Paluch. Actin cortex mechanics and cellular morphogenesis. *Trends in cell biology*, pages 1–10, 2012.
- [113] G. Salbreux, J. Prost, and J.-F. Joanny. Hydrodynamics of Cellular Cortical Flows and the Formation of Contractile Rings. *Physical Review Letters*, 103(5):058102, 2009.
- [114] F. C. Sauer. Mitosis in the Neural Tube. *Journal of Comparative Neurology*, 62(2):377–405, 1935.
- [115] I. F. Sbalzarini. Modeling and simulation of biological systems from image data. *BioEssays : news and reviews in molecular, cellular and developmental biology*, 35(5):482–90, May 2013.
- [116] U. S. Schwarz, N. Q. Balaban, D. Riveline, A. Bershadsky, B. Geiger, and S. A. Safran. Calculation of forces at focal adhesions from elastic substrate data: the effect of localized force and the need for regularization. *Biophysical journal*, 83(3):1380–1394, 2002.
- [117] U. S. Schwarz and S. A. Safran. Elastic Interactions of Cells. *Physical Review Letters*, 88(4):048102, 2002.
- [118] U. S. Schwarz and S. A. Safran. Physics of adherent cells. *Reviews of Modern Physics*, 85(3):1327–1381, 2013.
- [119] J. Sedzinski, M. Biro, A. Oswald, J.-Y. Tinevez, G. Salbreux, and E. Paluch. Polar actomyosin contractility destabilizes the position of the cytokinetic furrow. *Nature*, 476(7361):462–466, 2011.
- [120] S. Strome and W. B. Wood. Generation of asymmetry and segregation of germ-line granules in early *C. elegans* embryos. *Cell*, 35(1):15–25, 1983.
- [121] P. J. Strzyz, H. O. Lee, J. Sidhaye, I. P. Weber, L. C. Leung, and C. Norden. Interkinetic Nuclear Migration Is Centrosome Independent and Ensures Apical Cell Division to Maintain Tissue Integrity. *Developmental Cell*, 32(2):203–219, 2015.

- [122] T. M. Svitkina, A. B. Verkhovskiy, K. M. McQuade, and G. G. Borisy. Analysis of the actin-myosin II system in fish epidermal keratocytes: Mechanism of cell body translocation. *Journal of Cell Biology*, 139(2):397–415, 1997.
- [123] J. Swaminathan. Ribbon diagram of human vimentin. <http://www.ebi.ac.uk/pdbe-srv/view/images/entry/1gk4600.png>, 2009. Accessed: 2015-07-10.
- [124] H. Tanimoto and M. Sano. A simple force-motion relation for migrating cells revealed by multipole analysis of traction stress. *Biophysical journal*, 106(1):16–25, 2014.
- [125] E. Taverna, M. Götz, and W. B. Huttner. The Cell Biology of Neurogenesis: Toward an Understanding of the Development and Evolution of the Neocortex. *Annual review of cell and developmental biology*, 30:1–38, 2014.
- [126] E. Taverna and W. B. Huttner. Neural progenitor nuclei IN motion. *Neuron*, 67(6):906–914, 2010.
- [127] J. A. Theriot and T. J. Mitchison. Actin microfilament dynamics in locomoting cells. *Nature*, 352(6331):126–131, 1991.
- [128] J.-Y. Tinevez, U. Schulze, G. Salbreux, J. Roensch, J.-F. Joanny, and E. Paluch. Role of cortical tension in bleb growth. *Proceedings of the National Academy of Sciences of the United States of America*, 106(44):18581–18586, 2009.
- [129] J.-W. Tsai, W.-N. Lian, S. Kemal, A. R. Kriegstein, and R. B. Vallee. Kinesin 3 and cytoplasmic dynein mediate interkinetic nuclear migration in neural stem cells. *Nature neuroscience*, 13(12):1463–1471, 2010.
- [130] Y. C. Tse, M. Werner, K. M. Longhini, J.-C. Labbe, B. Goldstein, and M. Glotzer. RhoA activation during polarization and cytokinesis of the early *Caenorhabditis elegans* embryo is differentially dependent on NOP-1 and CYK-4. *Molecular Biology of the Cell*, 23(20):4020–4031, 2012.
- [131] S. Usami, S. L. Wung, B. A. Skierczynski, R. Skalak, and S. Chien. Locomotion forces generated by a polymorphonuclear leukocyte. *Biophysical journal*, 63(6):1663–1666, 1992.
- [132] A. van Leeuwenhoek. Observations, Communicated to the Publisher by Mr. Antony van Leeuwenhoek, in a Dutch Letter of the 9th of Octob. 1676. Here English'd: concerning Little Animals by Him Observed in Rain-Well-Sea. and Snow Water; as Also in Water Wherein Pepper Had Lain In. *Philosophical Transactions of the Royal Society of London*, 12(133-142):821–831, 1677.
- [133] M. Vicente-Manzanares, X. Ma, R. S. Adelstein, and A. R. Horwitz. Non-muscle myosin II takes centre stage in cell adhesion and migration. *Nature reviews. Molecular cell biology*, 10(11):778–790, 2009.
- [134] Y. L. Wang, J. D. Silverman, and L. G. Cao. Single particle tracking of surface receptor movement during cell division. *The Journal of cell biology*, 127(4):963–971, 1994.

- [135] E. W. Weisststein. Christoffel symbol of the second kind. <http://mathworld.wolfram.com/ChristoffelSymboloftheSecondKind.html>. Accessed: 2015-07-15.
- [136] M. D. Welch, A. Iwamatsu, and T. J. Mitchison. Actin polymerization is induced by Arp2/3 protein complex at the surface of *Listeria monocytogenes*. *Nature*, 385(6613):265–269, 1997.
- [137] L. Wolpert, C. Tickle, and A. M. Arias. *Principles of development*. Oxford university press, 2011.

Acknowledgements

First and foremost, I would like to thank Guillaume Salbreux for the excellent supervision of this thesis; for the opportunity to work with him on the physics of the cytoskeleton, for sharing his knowledge and skills with me, and the extensive input and support I received over the last three years.

I am grateful to my thesis advisory committee members Frank Jülicher, Caren Norden and Jochen Guck for their continuous feedback and helpful advice, and I'm indebted to Frank and Jochen for agreeing to review this thesis.

I'm deeply thankful to Martin Bergert and Ewa Paluch for the truly fantastic collaboration on Walker cell migration, Iskra Yanakieva, Hyun-Ok Lee, Marija Matejic and Caren Norden for many inspiring hours dwelling on the mechanisms of interkinetic nuclear migration, and Anne-Cecile Reymann and Stephan W. Grill for allowing me to work on cell furrowing with them.

The members of the biological physics department have provided me with a wonderful working environment, many fruitful discussions and a generally great time. In particular, I'd like to thank (in alphabetical order) Silvanus Alt, Johannes Baumgart, David Jörg, Gary Klindt, Matthias Merkel, Alexander Mietke, Amitabha Nandi, José Negrete Jr., Wolfram Pönisch, Marko Popovic, Pawel Romanczuk, Jochen Schneider, André Scholich, Fabio Staniscia, and Steffen Werner.

Special thanks go to Alexander Mietke, Marko Popovic, Caren Norden, Iskra Yanakieva, Anne-Cecile Reymann, Jochen Schneider, Christine Earl, Peter Erzberger and Sacha Sokoloski for reading and commenting on sections of this thesis. I'm also thankful to the administrators of the Dresden Internation PhD Program and the MPI-PKS, in particular Melina Bohla, Marleen Franke and Ulrike Burkert for helping me with the buerocratic aspects of the last three years.

And last but not least, I would like to thank my amazing family and friends.

BIBLIOGRAPHY

Versicherung

Hiermit versichere ich, dass ich die vorliegende Arbeit ohne unzulässige Hilfe Dritter und ohne Benutzung anderer als der angegebenen Hilfsmittel angefertigt habe; die aus fremden Quellen direkt oder indirekt übernommenen Gedanken sind als solche kenntlich gemacht. Die Arbeit wurde bisher weder im Inland noch im Ausland in gleicher oder ähnlicher Form einer anderen Prüfungsbehörde vorgelegt.

Die Arbeit wurde am Max-Planck-Institut für Physik komplexer Systeme angefertigt und von Dr. Guillaume Salbreux betreut.

Ich erkenne die Promotionsordnung der Fakultät Mathematik und Naturwissenschaften der Technischen Universität Dresden an.

Anna Erzberger